

**COMPUTATIONAL MODELING, STOCHASTIC AND
EXPERIMENTAL ANALYSIS WITH THERMOELASTIC
STRESS ANALYSIS FOR FIBER REINFORCED
POLYMERIC COMPOSITE MATERIAL SYSTEMS**

A Thesis
Presented to
The Academic Faculty

by

Shane M. Johnson

In Partial Fulfillment
of the Requirements for the Degree
Doctor of Philosophy in the
School of Civil and Environmental Engineering

Georgia Institute of Technology
August 2010

**COMPUTATIONAL MODELING, STOCHASTIC AND
EXPERIMENTAL ANALYSIS WITH THERMOELASTIC
STRESS ANALYSIS FOR FIBER REINFORCED
POLYMERIC COMPOSITE MATERIAL SYSTEMS**

Approved by:

Professor Rami Haj-Ali, Advisor
Department of Civil Engineering
Georgia Institute of Technology

Professor Kenneth Will
Department of Civil Engineering
Georgia Institute of Technology

Professor Donald White
Department of Civil Engineering
Georgia Institute of Technology

Professor Abdul-Hamid Zureick
Department of Civil Engineering
Georgia Institute of Technology

Professor Andrew Makeev
Department of Aerospace Engineering
Georgia Institute of Technology

Date Approved: April 2010

ACKNOWLEDGEMENTS

My thanks and appreciation go to Dr. Rami Haj-Ali, my advisor, for his guidance, encouragement, persistence, patience and expert advice. Interaction with him has inspired my love of research and has encouraged me to seek new and exciting challenges. My gratitude also goes to my colleagues Rani El-Hajjar, Bo-Siou Wei, and Hee-Sun Kim. Thanks are also in order to Bradley Boyce of Stress Photonics Inc. for his expert advice and valuable technical assistance in the field of Infrared Thermography. Thanks to Erian Armanios for opening his composites manufacturing lab to my research group, and thanks to Xinyuan Tan for guiding me to manufacturing quality composites.

TABLE OF CONTENTS

ACKNOWLEDGEMENTS	iii
LIST OF TABLES	vii
LIST OF FIGURES	viii
LIST OF SYMBOLS OR ABBREVIATIONS	xiv
SUMMARY	xiv
I INTRODUCTION	1
1.1 General	1
1.1.1 Fiber Reinforced Polymeric Materials	1
1.1.2 Thermography	2
1.2 Experimental Studies	3
1.2.1 Quantitative Thermography and Thermoelastic Stress Analysis in Composites	3
1.2.2 TSA for Damage in FRP Composites	7
1.2.3 Experimental Studies on Jute Hybrid Bio-Composites	9
1.2.4 Damage in FRP Lap Joints	10
1.3 Analytical and Numerical Studies	12
1.3.1 Nonlinear Anisotropic Micro-macromechanical Modeling	12
1.3.2 Analytical and Computational Modeling of FRP Lap Joints	16
1.3.3 Fatigue Damage Models for FRP Composites	19
1.4 Objective	22
1.5 Present Study	23
II THERMOELASTIC STRESS ANALYSIS FOR QUANTITATIVE ANALYSIS	26
2.1 Methodology	26
2.2 Derivation	27
2.3 IR Test Setup	33

2.4	Validation of TSA Technique on Prepreg and Pultruded Composites	36
2.5	Thermomechanical Calibrations for Various FRP Composites . . .	37
2.6	Validation under a Multi-axial state of stress	42
III	MECHANICAL BEHAVIOR OF JUTE HYBRID BIO-COMPOSITES	54
3.1	Introduction	54
3.2	Jute Hybrid Bio-composite Systems	55
3.3	Nonlinear Constitutive Models for Bio-Composites	57
3.3.1	Anisotropic Deformation Theory (ADT) Based Model . . .	59
3.3.2	Anisotropic Potential Theory Model (APT)	61
3.3.3	New Formulation for the Nine-Cell Micromechanical Model (Nine-Cell)	64
3.3.4	The HFGMC micromechanical modeling framework	72
3.4	Calibration and Verification	88
IV	THERMOELASTIC STRESS ANALYSIS FOR FAILURE INITIATION AND PROGRESSION IN COMPOSITE LAP SHEAR JOINTS	110
4.1	Introduction	110
4.2	Proposed IR-TSA Testing Set-up	111
4.3	Proposed IR Testing Approach	114
4.4	Results	119
V	A STOCHASTIC FATIGUE DAMAGE MODEL FOR COMPOSITE SIN- GLE LAP SHEAR JOINTS BASED ON MARKOV CHAINS AND THER- MOELASTIC STRESS ANALYSIS	126
5.1	Introduction	126
5.2	Testing Setup	129
5.3	Fatigue damage metrics using IR-TSA	133
5.4	A cumulative damage model using Markov chain theory	138
5.5	TSA results and Stochastic S-N curves	140
5.6	TSA results and Stochastic S-N curves	149
VI	CONCLUSION	152

6.1	Quantitative Thermoelastic Stress Analysis	152
6.2	Analytical and Experimental Analyses for Jute Hybrid Bio-Composites	152
6.3	Damage Initiation of FRP Lap Joints	153
6.4	Stochastic Fatigue of FRP Lap Joints	155
6.5	Future Work	156
6.5.1	Fatigue of Lap Joints	156
6.5.2	Fatigue of 3D Woven Fiber Reinforced Polymeric Material Systems	157
REFERENCES		159

LIST OF TABLES

1	Effective Elastic Properties	36
2	Description of Jute hybrid bio-composite material system	55
3	Nominal V-notch Specimen Dimensions	91
4	Unidirectional elastic material properties of Jute with chopstrand mat	92
5	Calibrated Ramberg-Osgood Relations and Parameters for Jute / Glass Chopstrand Mat	93
6	Ultimate material properties of Jute with chopstrand mat	93
7	Fiber linear elasetic properties used in the Nine-Cell RUC	94
8	Nine-Cell RUC Isotropic Nonlinear Matrix Material Properties (Ramberg- Osgood Relations)	94
9	Nine-Cell RUC geometry for equivalent constituent volume fractions .	94
10	Nine-Cell RUC in-plane cell properties for equivalent volume fractions	96
11	Unidirectional material properties of IM7/epoxy composite laminate .	115
12	Unidirectional material properties of S2-glass/epoxy composite laminate	132
13	Number of test specimens and applied stresses	133
14	Number of test specimens and applied stresses	140

LIST OF FIGURES

1	Schematic cross-sectional view of a layered orthotropic composite with surface coatings	28
2	Schematic of TSA Setup for thermomechanical calibration	34
3	Setup for Thermo-mechanical calibration	35
4	Thermo-mechanical calibration for E-glass/epoxy	37
5	Thermo-mechanical calibration for Uncoated Carbon/Epoxy	38
6	Schematic showing the lay-up for $[0_5/90/0_5]$	38
7	Thermo-mechanical calibration for uncoated S2glass/Epoxy for the $[0_5/90/0_5]$ Lay-up	39
8	Thermo-mechanical calibration for coated S2-glass/epoxy	40
9	Thermo-mechanical calibration for quasi isotropic S2-glass/Epoxy . .	41
10	Geometry of notched specimen used to verify the TSA technique and a very refined quarter-model FE mesh used to model the notched specimen	43
11	TSA images of open hole specimens of Carbon/epoxy	44
12	Horizontal line interrogation of open-hole geometry for verification of thermomechanical calibration of un-coated unidirectional carbon/epoxy	45
13	Horizontal line interrogation of open-hole geometry for verification of thermomechanical calibration of coated unidirectional carbon/epoxy .	46
14	Vertical line interrogation of open-hole geometry for verification of thermomechanical calibration of coated unidirectional carbon/epoxy .	46
15	Vertical line interrogation of open-hole geometry for verification of thermomechanical calibration of un-coated unidirectional carbon/epoxy	47
16	TSA images of open hole specimens of S2-glass/epoxy	48
17	Horizontal line interrogation of open-hole geometry for verification of thermomechanical calibration of un-coated S2-glass/epoxy for the $[0_5/90/0_5]$ lay-up	49
18	Horizontal line interrogation of open-hole geometry for verification of thermomechanical calibration with epoxy coating of S2-glass/epoxy for the $[0_5/90/0_5]$ lay-up	49

19	Horizontal line interrogation of open-hole geometry for verification of thermomechanical calibration of un-coated quasi-isotropic S2-glass/epoxy lay-up	50
20	Horizontal line interrogation of open-hole geometry for verification of thermomechanical calibration with epoxy coating of quasi-isotropic S2-glass/epoxy lay-up	51
21	Vertical line interrogation of open-hole geometry for verification of thermomechanical calibration of un-coated S2-glass/epoxy for the $[0_5/90/0_5]$ lay-up	52
22	Vertical line interrogation of open-hole geometry for verification of thermomechanical calibration with epoxy coating of the S2-glass/epoxy for the $[0_5/90/0_5]$ lay-up	52
23	Vertical line interrogation of open-hole geometry for verification of thermomechanical calibration for un-coated S2-glass/epoxy with a quasi-isotropic lay-up	53
24	Vertical line interrogation of open-hole geometry for verification of thermomechanical calibration with epoxy coating for S2-glass/epoxy with a quasi-isotropic lay-up	53
25	Hybrid Jute/Glass composite with chopstrand mat surface layer . . .	56
26	Color similarity algorithms used to identify and segment Jute yarns from background	56
27	(a) Idealized medium with periodic arrays of long fibers (rectangular cross-sections) showing a quarter UC (bold line), (b) Nine-cell micro-model of rectangular UC	65
28	Schematic illustration of a unidirectional periodic array in the global $x_2 - x_3$ plane of multiphase composite media with its repeating unit-cell (RUC), defined with respect to its $y_2 - y_3$ local coordinate system. .	74
29	General arrangement of cells and their geometry and coordinate systems for the HFGMC-RUC model. Mirrored cells-interfaces are illustrated to enforce the periodic boundary conditions.	75
30	One-cell configuration with its neighboring cells showing its two primary "feed-forward" interfaces along with the location for the stress integration points.	82
31	Overall tangential system of equations for the HFGMC-RUC model indicating the contribution of cell $(\beta\gamma)$ to the system and showing a row of complete equations for this cell.	85

32	Jute/glass chopstrand mat system as tested in tension in the fiber direction	89
33	Jute/glass chopstrand mat system as tested in compression in the transverse fiber direction	90
34	Jute/glass chopstrand mat v-notch specimen as tested with the Iosipescu fixture	91
35	Jute/glass chopstrand mat system as tested in shear with the Iosipescu fixture	92
36	Nine-Cell RUC geometry for System 1	95
37	Contour map of TSA image scaled to predicted remote axial stress and contour map of calculated axial stress from an optical strain analysis method of an open-hole specimen (Specimen 1) of Jute with chopstrand mat surface layer	97
38	Contour map of TSA image scaled to predicted remote axial stress and contour map of calculated axial stress from an Digital Image Correlation method of an open-hole specimen (Specimen 2) of Jute with chopstrand mat surface layer	98
39	Contour map of predicted remote axial stress of open-hole specimen Jute with chopstrand mat surface layer showing ADT and APT Models	99
40	Contour map of predicted remote axial stress of open-hole specimen Jute with chop strand mat surface layer showing Linear and Nine-Cell Models	100
41	Axial Stress line interrogation on open-hole specimen for 400lb loading on Jute with chop strand mat material system showing the prediction capabilities of the Nine-Cell Model and Linear orthotropic models . .	101
42	Axial Stress line interrogation on open-hole specimen for 400lb loading on Jute with chop strand mat material system showing the prediction capabilities of the ADT, APT and Linear orthotropic models	102
43	Translaminar Fracture Toughness Test Specimen Schematic	103
44	Results of the Translaminar Fracture Toughness Test on Jute/Glass Chopstrand using the Eccentrically Loaded Single Edge Notched Tension Specimen	104
45	Remote Stress vs. Remote Axial Strain, Image Correlation at Location 1 used for validation of the ADT, APT, Nine-Cell models, Linear, and XFEM orthotropic models	106

46	Remote Stress vs. Axial Strain at Open Hole Edge, Image Correlation at Location 2 used for validation of the ADT, APT, Nine-Cell models, Linear, and XFEM orthotropic models	107
47	Remote Stress vs. Axial Strain, Digital Image Correlation at Location 3 used for validation of the ADT, APT, Nine-Cell models, Linear, and XFEM orthotropic models	108
48	Remote Stress vs. Axial Strain, Digital Strain Analysis using 3/4 inch gauge length extensometer over the open hole used for validation of the ADT, APT, Nine-Cell models, Linear, and XFEM orthotropic models	109
49	Infrared camera and the IR-TSA experimental setup	112
50	Areas of interest and IR Window	113
51	Schematic for Expected IR Front View of Lap Joint	114
52	Single Lap Joint specimen geometry made from IM7 Quasi-isotropic laminates	115
53	Deformed single lap joint	116
54	Peel and shear stresses in a typical IM7/Epoxy quasi-isotropic single lap shear joint	116
55	Localized stress intensity at bond edge, FE results showing peel stresses at bond edge on a deformed IM7/Epoxy quasi-isotropic single lap joint	117
56	Two proposed IR-TSA Test Methods. Method-A: a static load step is applied, followed by a cyclic loading about this loading level. Method-B: a static load is applied and unloaded followed by cyclic loading at a pre-specified load and cyclic load amplitude. The next applied static load level is increased.	118
57	Front and side view of the crack front formation in long-bond single-lap shear joint made with woven plates and tested with Method A, ultimate failure occurs immediately following the 4,450 lb load level. Signature of crack tip is visible from the side view at the 4,400 lb load level.	119
58	Front and side view of the crack front formation at the bond edge in long-bond single-lap shear joint made from uni-tape plates tested with Method A, ultimate failure occurs immediately following the 3,300 lb load level. Signature of crack tip is visible from the side view at the 3,200 lb load level.	120

59	Early stages of crack formation and damage initiation in short-bond single-lap shear joint made from woven plates tested with procedure B preserved after a maximum load level of 1700lb. Noticeable changes in the bond line IR measurement from (c) to (d).	121
60	Early stages of crack formation and damage initiation in short-bond single lap-shear joint made with uni-tape plates tested with Method B and preserved after a maximum load level of 2000lb. Increasing changes in bondline IR emission indicating damage progression from (b) to (c) and (c) to (d).	122
61	Early stages of crack formation and damage initiation in long-bond single-lap shear joint made from woven plates tested with Method B and preserved after a maximum load level of 3750lb. Increasing changes in bondline IR emission indicating damage progression from (b) to (c) and (c) to (d). Noticeable drop in stress concentration from (c) to (d).	122
62	Early stages of crack formation and damage initiation in long-bond single-lap shear joint made from uni-tape plates tested with Method B and preserved after a maximum load level of 1900lb. Increasing changes in bondline IR emission indicating damage progression from (c) to (d). Noticeable drop in stress concentration from (c) to (d).	123
63	Photograph showing micro-cracking in short bond line fabric specimen #1 (200X) corresponding to IR-TSA measurement in Figure 59.	124
64	Photograph showing disbonding at the adhesive interface in short bond-line fabric specimen #4 (200X)	124
65	Photograph showing micro-cracking in short bond line uni-tape specimen #5 (50X) corresponding to IR-TSA in Figure 60.	125
66	Fatigue Test Setup for S2-glass/E733FR Single Lap Joints	130
67	S2-glass/E733FR Single Lap Joint specimen geometry	132
68	Typical evolution of maximum IR-TSA spatial gradients for increasing fatigue cycles	135
69	Typical evolution of maximum IR-TSA spatial gradients for increasing fatigue cycles	135
70	Area measures to evaluate the typical damage evolution as defined by differential IR-TSA under increasing fatigue cycles	136
71	Normalized effective bond length measures to evaluate the typical damage evolution as detected by IR-TSA under increasing fatigue cycles	137
72	Fatigue damage indices of shear lap joints subjected to stress level of 0.65	141

73	Fatigue damage indices of shear lap joints subjected to stress level of 0.55	142
74	S-N curve progression for damage index of TSA area	144
75	Constructed stochastic SN data based on two limited data sets and previously calibrated MCM	145
76	Proposed algorithm for generating stochastic S-N curves using previously calibrated MCMs.	147
77	Schematic representation of the construction of stochastic SN curves.	148
78	Thermoelastic Stress Analysis for Fatigue of an IM7 Laminate	149
79	Thermoelastic Stress Analysis for Fatigue of an IM7 Single Lap Joint	149
80	Thermoelastic Stress Analysis for Fatigue of an IM7 single nested overlap joint	150
81	Thermoelastic Stress Analysis for Fatigue of a Unidirectional S2-Glass/Epoxy Laminate	150
82	Thermoelastic Stress Analysis for Fatigue of a Quasi-Isotropic S2-Glass/Epoxy Laminate	150
83	Thermoelastic Stress Analysis for Fatigue of a Quasi-Isotropic S2-Glass/Epoxy Single Nested Overlap Joint	151
84	Thermoelastic Stress Analysis for Fatigue of a Quasi-Isotropic S2-Glass/Epoxy Single Nested Overlap Joint	151

SUMMARY

Many studies with Thermoelastic Stress Analysis (TSA) and Infrared Thermography, in Fiber Reinforced Polymeric materials (FRPs), are concerned with surface detection of "hot spots" in order to locate and infer damage. Such experimental analyses usually yield qualitative relations where correlations between stress state and damage severity cannot be obtained. This study introduces quantitative experimental methodologies for TSA and Digital Image Correlation to expand the use of remote sensing technologies for static behavior, static damage initiation detection, and fatigue damage in FRPs. Three major experimental studies are conducted and coupled with nonlinear anisotropic material modeling: static and TSA of hybrid bio-composite material systems, a new stochastic model for fatigue damage of FRPs, and fracture analysis for FRP single-lap joints. Experimental calibration techniques are developed to validate the proposed macromechanical and micromechanical nonlinear anisotropic modeling frameworks under multi-axial states of stress. The High Fidelity Generalized Method of Cells (HFGMC) is a sophisticated micromechanical model developed for analysis of multi-phase composites with nonlinear elastic and elastoplastic constituents is employed in this study to analyze hybrid bio-composites. Macro-mechanical nonlinear anisotropic models and a linear orthotropic model for fracture behavior using the Extended Finite Element method (XFEM) are also considered and compared with the HFGMC method. While micromechanical and FE results provide helpful results for correlating with quasi-static behavior, analyzing damage progression after damage initiation is not straightforward and involves severe energy dissipation, especially with increasing damage progression. This is especially true for fatigue damage evolution, such as that of composite joints as it is associated

with uncertainty and randomness. Towards that goal, stochastic Markov Chain fatigue damage models are used to predict cumulative damage with the new damage indices proposed using full-field TSA image analysis algorithms developed for continuously acquired measurements during fatigue loading of S2-Glass/E733FR unidirectional single-lap joints. Static damage initiation is also investigated experimentally with TSA in single-lap joints with thick adherends providing for new design limitations. Fracture behavior of a single-lap joint is also analyzed with different fracture methods including the Virtual Crack Closure Technique (VCCT) and critical stress techniques. The computational modeling, stochastic and experimental methods developed in this study have a wide range of applications for static, fracture and fatigue damage of different FRP material and structural systems.

CHAPTER I

INTRODUCTION

1.1 General

This chapter presents a literature review of significant studies on experimental, analytical and numerical studies characterizing the behavior of fiber reinforced polymeric (FRP) material systems. In addition, quantitative experimental studies on the use of Infrared Thermography and Thermoelastic stress analysis, micromechanical and macromechanical modeling approaches, static and fatigue damage detection in FRPs, and stochastic modeling approaches for fatigue damage in FRPs. The final section of this chapter will outline the objectives and research approach of the present study.

1.1.1 Fiber Reinforced Polymeric Materials

Fiber reinforced polymeric materials (FRP) consist of glass, graphite or carbon, aramid, boron, silicon carbide, natural fibers, etc. held together in a structural unit with a binder or matrix material and combined with fillers for mechanical performance or cost benefits. The binder or matrix material for FRPs is either a thermoset or thermoplastic. Thermosets use polymer chains that cross-link and therefore do not melt at high temperatures. Thermoplastics, on the other hand, use polymer chains that do not cross-link allowing them to melt and harden again when cooled. Typical thermosets are epoxies, polyester, or phenolic. Typical thermoplastics are polyimide, polysulfone, polyetheretherketone (PEEK), or Polyphenylene sulfide.

Types of fiber reinforced composites include continuous, woven, chopped, and hybrid composites. Hybrid composites consist of mixed fiber types or fiber geometries. Continuous composites consist of continuous fibers oriented in individual layers or laminae and bonded together to form a laminate. Fabrication Processes for FRP

typically include open molds, autoclave, compression moulding, filament winding, pultrusion, reinforced reaction injection molding, thermoplastic molding, resin transfer molding, and structural reaction injection molding. An autoclave is a heated pressure vessel which takes a laminate through a temperature and pressure curing program. Prepreg is typically used for autoclaved laminates. Prepreg is a tape of precoated fibers with polymer resin. Achieving void contents of 0.1% is typical for autoclaved laminates using prepreg. Pultrusion is a manufacturing process in which unidirectional filaments are impregnated in resin and pulled through a heated die to produce long prismatic structural components. Pultrusion and autoclaving were used for fabricating the glass, carbon, and hybrid jute-glass fiber reinforced polymeric materials used in this study.

1.1.2 Thermography

Thermography is the science of measuring temperature changes on the surface of materials due to stress generated thermal fields (SGTF) or externally applied thermal fields (EATF). Thermography is a non-destructive investigation (NDI) tool that allows remote sensing capabilities to detect imperfections or characterize materials. This NDI tool typically requires a sensitive infrared camera capable of detecting temperatures changes less than 50 mK. Sensitivities commonly reported during the 1980's were 0.1K, and in many cases trouble with data measurements was reported due to ambient conditions. Since that time, methods to process and measure thermal data such as Stress Pattern Analysis by Thermal Emission (SPATE) where points are scanned in a point-by-point manner under adjustable computer control have developed into fast and accurate full-field Thermoelastic Stress Analysis (TSA) methods. SPATE methods required 1-2 hours to obtain a single image scanning 50 points per second. Thermoelasticity measurement systems today have a thermal resolution of at least 1 mK for a full-field image with exposure times of 1 minute or less. This

temperature sensitivity allows for more sophisticated remote sensing capabilities to exploit damage and damage progression in materials and structural components.

Materials must be excited to expose imperfections. Thermography can be used to detect anomalies spatially because imperfections disrupt heat transfer. An excitation source is the heat source that introduces energy to cause heat energy transfer to occur. Excitation sources can be applied by externally applied thermal fields or by mechanical means for stress generated thermal fields. In either case the thermal field produced is dependent on the emissivity of the material investigated. Emissivity is the ability and efficiency of a material to emit, reflect, or absorb energy. The choice of EATF or SGTF depends on the application, service conditions, material properties, and experience. In the field, the service conditions such as vibrations may be used to excite the material. In many cases discrimination of damage effects is difficult, and the particular method of IR-thermography used is based on the desire to illuminate and excite the particular imperfections of interest.

1.2 Experimental Studies

1.2.1 Quantitative Thermography and Thermoelastic Stress Analysis in Composites

Quantitative infrared thermography NDE methods are non-contact full-field techniques whereby an IR camera with digital sensors is used to detect small changes of temperature due to different sources. The later can be in the form of an irreversible applied mechanical load, direct heat source, ultrasonic stress waves, among others. The overall goal is to subject the structure or the material to thermomechanical deformation that produce spatial variations in the surface temperatures and allow correlation between measured IR field and the stress or strain on the surface. Under adiabatic and reversible conditions in isotropic materials, the application of a small cyclic load will induce small and repeated variations in temperature that are proportional to the sum of principle stresses. Kelvin [125] (Thomson, 1878) was the first to propose this

thermoelastic principal. He used thermodynamics-based derivations to obtain a linear relation between the temperature change and the first stress-invariant. The recent advances and affordability of charged-coupled-device (CCD) cameras, with fast acquisition systems, have lead to a powerful and quantitative thermoelastic stress analysis (TSA) measurement techniques. The first invariant of the stress can be measured on the surface of loaded coupons made of homogeneous materials. TSA has been also applied in composite materials to measure stresses in thin laminated composites with and without damage. Limited attention has been directed to quantitative TSA in multi-layered fiber reinforced plastic (FRP) composite materials. In laminated composites, several difficulties may arise in the use of TSA, such as the effects of mean stress and frequency dependent testing. Temperature diffusion and non-adiabatic approaches have been proposed to model the thermoelastic effect in laminated composites. Potter et al. [104, 105] developed techniques to investigate the thermoelstic effect in laminated composites. Bakis and Reifsneider [13] used laminate analysis and micromechanical formulations to develop predictions of the thermoelastic signal, and good agreement was found between their analytical analysis and experiments, with differences due possibly to material heterogeneity and laminate surface conditions. They also investigated the effect of the cyclic loading frequency on the thermoelastic singal to find spurious non-adiabatic effects above 30 Hz. Dunn [44] used a mathematical model to account for the thermal conduction in the top epoxy layer of a graphite/epoxy composite. Kyriakopoulos et al. [87] used heat conduction finite element analysis to quantify the TSA signal in the absence of adiabatic conditions. In the case of thin laminates, the IR camera was found to detect temperature changes on the surface ply alone. Van Hemelrijck et al. [68] utilized a non-adiabatic theory approach that took into account the interlaminar heat transfer and obtained good correlation between theoretical and experimental results of the surface temperature for a cross-ply carbon/epoxy laminate. The technique was also used for qualitative

and limited quantitative studies. For example, Zhang et al. [140–142] studied the dependence of the thermal coefficients of thermal expansion, thickness of surface matrix resin, loading frequency, and changes in absolute temperature on the TSA signal. They noticed an effect of the surface resin thickness. By altering the resin thickness, they found that the TSA signal is highest without a surface layer and above a certain thickness the TSA signal is constant-independent of specimen thickness. They related this effect to a lack of heat transfer from the load carrying fibers to the surface at greater thicknesses. They also researched stress concentrations in the knit-yarn fiber intersections in a woven carbon/epoxy laminate. A mean stress effect was observed in the glass/epoxy composite that was studied. Dulieu-Smith et al. [43] reported test results of a full-field stress characterization on a woven tee-joint with FRP laminated fillets. Cunningham et al. [36] used a DeltaTherm IR detection system to characterize damage around a circular hole in a laminated plate with unidirectional E-glass/epoxy. Mackenzie [92] and Welch and Zickel [133] investigated the characteristics of the thermal radiation signal emitted from different surface coatings. The solution of Mackenzie for the thermal wave problem characterized the IR flux amplitude from the surface as a function of IR reflection and thermal material properties of the considered substrate-coat-air system. Using material properties of a typical paint coating, a range of thicknesses and applied thermal frequencies was identified to allow the coat to act as a strain witness layer. Barone and Patterson [17] proposed using a polymeric coating to extract the strain field from TSA measurements. Their method was applied for isotropic substrates. Good correlation between analytical solutions and measured TSA responses was obtained for aluminum plates with circular holes. El-Hajjar and Haj-Ali [48] proposed a technique to measure the sum of the direct strains on the surface of thick section and orthotropic composites to the TSA signal obtained from the surface of the specimen. Their method was verified experimentally and compared favorably with finite-element (FE) simulations of notched and cracked

coupons. This method was used to verify damage studies in thick-section composite materials, considered by Kilic and Haj-Ali [82] and Haj-Ali and El-Hajjar [49]. Ju and Rowlands [78] applied the stress field solution expansion from Khalil et al. [71] together with a thermoelastic stress analysis approach to determine the stress intensity factors (SIFs) of off-axis crack orthotropic composites. The thermoelastic stress signal was assumed to relate to the in-plane direct stresses through two separate coefficients. They used finite element analysis to calibrate the two thermo-mechanical coefficients to correlate the thermoelastic signals to the direct stresses. The SIFs from Lekhnitskii's solution [88] via thermoelastic stress signals were calculated and compared with those obtained from FE models. Tomlinson and Marsavina [127] and Diaz et al. [39, 40] used Muskhelishvili's solution [98] to calculate the stress intensity factors (SIFs) in metallic materials using different IR-TSA techniques. They provided methods to determine the location of the crack tip and studied the crack closure and residual stress in their research. The SIFs were also determined from the fatigue crack. Thick section pultruded composites were investigated and their TSA technique showed accurate ability compared with analytical FE solutions. Haj-Ali et al. [62] developed two IR-TSA methods to measure of the sum of surface strains from the surface of FRP orthotropic composites. They showed that the mixed mode stress intensity factors can be calculated using their method and the Lekhnitskii's anisotropic elasticity solution for the stress field ahead of a crack tip in anisotropic medium. Emery et al. [50] similarly developed calibration techniques relating the in-plane strains and material properties to predict the thermoelastic signal in orthotropic laminates taking into account the surface characteristics. Dulieu-Barton et al. [42] developed a temperature correction methodology for fiber reinforced polymeric materials and metals to account for a mean ambient temperature effect during TSA measurements. Their methodology is better able to filter out effects outside of the cyclic loading such as the operator handling the specimen during acquisition or

heat flow from the grips to the specimen during cyclic loading.

1.2.2 TSA for Damage in FRP Composites

Several studies have shown that infrared thermography is a powerful tool for evaluating damage in many applications with fiber reinforced polymeric materials. Dulieu-Smith et al. [43] evaluated a GRP tee joint using a combination of Thermoelastic Stress Analysis (TSA) and FEA. The goal of the study was to correlate finite element to TSA without evaluating damage; however the method can be extended to provide a tool for investigating damage initiation and propagation in composite joints. Mackin and Roberts [93] tracked static damage progression in ceramic matrix composites using TSA on double edge notched specimens. Bakis et al. [14] related the residual strength, stiffness, and fatigue life to their corresponding damage states obtained from photoelastic coating and thermal emission experiments for circular notched graphite/epoxy laminates subjected to fully reversed fatigue loads. They observed the damage initiated around the hole for quasi-isotropic and orthotropic laminates. Matrix cracking and delamination patterns were different in both cases due to the interaction between adjacent plies. Compared with photoelastic data, the thermal emission was more sensitive to the minute deformations near fracture paths in surface plies. Bremond et al. [31] also illustrated the advantages of infrared thermography as a non-destructive method. Jones et al. [75] developed a damage variable based on Thermoelastic Stress Analysis data to analyze damage in metal and composite systems; this damage variable is showed excellent correlation to traditional measurements of crack length in their study. Kageyama et al. [79] suggested a damage threshold approach based on 3D FEA, and used TSA with linear elastic fracture mechanics to measure the crack propagation in notched carbon/epoxy laminates. Differential infrared thermography was proposed and used to track the damage in $[45^\circ]$ and $[0/90^\circ]$ type graphite/epoxy laminates by Lohr et al. [91]. In their experiment,

the measured temperature was seen to decrease as the number of cycles increased due to cracking in the epoxy surface layer. This effect was more pronounced under higher frequencies and made quantitative TSA difficult for these composite material systems. Adding a thick resin surface layer was found to stabilize the TSA signal and attenuate the heat transfer from the carbon/epoxy inner layers. Cavaliere et al. [33] applied TSA techniques to investigate the fatigue behavior of metal matrix composite sheets joined by friction stir welding process. They stated that the infrared signal relating the sum of principal stresses can be used to investigate stress concentration and the stress intensity factors for notched metal matrix composite specimens. El-Hajjar and Haj-Ali [48, 63] proposed a technique to measure the sum of the direct strains on the surface of thick section and orthotropic composites to the TSA signal obtained from the surface of the specimen. Their method was verified experimentally and compared favorably with FE simulations of notched and cracked coupons. This method was used to verify damage studies in thick-section composite materials, considered by Kilic and Haj-Ali [81, 82]. Johnson et al [73, 74] showed fatigue damage progression in thick-section composites with Thermoelastic Stress Analysis (TSA). TSA data was gathered to obtain a mean thermal effect that was related to fatigue damage and damage evolution. The elastic modulus in pultruded materials was measured by an extensometer, and showed lower sensitivity under the fatigue loading than TSA measurements. A limited number of specimens was examined; therefore, it could not be used to predict fatigue damage evolution. This study was expanded on by Wei et al. [132], and stochastic Markov Chain models were developed to characterize the fatigue damage in composite laminates from the cumulative IR-TSA data. They proposed a method to predict the S-N curve and showed that TSA metrics could be used to predict fatigue damage evolution.

1.2.3 Experimental Studies on Jute Hybrid Bio-Composites

Hybrid fiber reinforced plastic FRP systems are composite materials that can combine different forms of reinforcement layers, such as roving, continuous filament mats (CFM), woven fabrics, and braided preforms. The reinforcement combination is usually repeated through the thickness of the cross-section of a flat member. Fibers can be made of carbon or glass or natural fiber yarns. Matrix materials are commonly made of polyester or vinylester resin that includes additives such as glass microspheres and clay particles. Pultruded composites can include thin and thick-walled members (1/16 to 1 in.) having similar shapes to the standard steel beam shapes, such as wide-angle, channels, and angle sections. Recently, FRP pultruded composite materials have been widely applied for civil and infrastructural engineering applications, such as bridges, transmission towers, and structural components of buildings.

The demand for natural fiber composite systems is increasing, e.g., due to legislation for partially decomposable vehicles to reduce landfills. Many car manufacturers are using this green technology not only because it can be marketed as green, but also because natural fiber systems can provide improved stiffness, weight, and insulation at lower cost than glass fibers [24]. Frames, decking material, railings for parapet wall, furniture sections, wall panels, roofing sheets, temporary shelters, post office boxes are some examples of structural applications utilizing natural fibers [70]. Wool et al. [120] suggests that monolithic roofs of natural fibers in a soybean resin can resist hurricanes in addition to providing beneficial insulation properties. Different combinations of fiber systems (Flax mats, Paper/chicken feathers, paper/corrugated paper, paper/e-glass fiber) for composite beams were investigated by Dweib et al. [46] as manufactured by the Vacuum Resin Assistant Transfer Moulding (VARTM) process to show the potential for different structural applications with natural fiber systems. Van de Velde et al. [128] developed pultruded systems from flax fibers.

Durability of natural fiber composites is a concern for any exposed application.

Several studies [21, 97] have investigated the durability of composites in an alkaline environment, three years natural and 1000h accelerated UV, simulated sunlight, immersion at 70C in water for 30 days, and freeze and thaw cycles (-25 to 20C), etc. These studies show that the severity of aging is most detrimental in accelerated water tests. Also in some natural fiber systems fungal infestation can occur at cut edges of weathered composites. Failure of natural fiber composites due to delamination or fibre swelling in wet conditions has spurred further work into chemical treatments to increase moisture resistance (increased performance in different aqueous environments) in the natural fibre systems [9, 22, 35, 47, 129, 138]. Sabeel Ahmed et al. [8] investigated various combinations of jute-glass laminates evaluating tensile, flexural, and interlaminar shear properties as measures of performance. The effect of hybridizing was investigated to minimize overall cost of the laminates taking advantage of the lower cost of jute while greatly increasing resistance to moisture absorption. They found that various jute-glass hybrids out perform a homogenous glass or jute reinforced polymer systems when cost and moisture resistance is taken into account. Jute fibers are popular as reinforcement materials because of their increased elastic modulus and higher elongation at fracture as compared to other natural fiber systems. Many sources list the longitudinal Youngs Modulus of Jute Fibers from 20 - 40 GPa; discrepancies in the literature are possibly due to assumptions of a circular cross-section [8, 23, 107, 113, 118] in addition to the inherent mechanical variability of natural systems. The modulus is significantly lower than the modulus of E-Glass fibers which have a longitudinal modulus of approximately 73GPa.

1.2.4 Damage in FRP Lap Joints

Recent innovations in advanced aerospace structures can be attributed to the manufacturing of composite materials with superior strength-to-weight ratios. Engineering

aircraft structures with composite materials requires a detailed knowledge of durability and damage tolerance of individual structural components and especially fiber reinforced polymer (FRP) joints. Traditional mechanical testing methods using extensometers and strain gauges of composite joints may only measure linear load-deformation responses to failure giving no indication of overload or failure initiation. Non destructive evaluation tools offer a significant refinement over traditional mechanical tests, such that failure initiation of critical components can be detected and identified with some limitations. This is especially important since the bonding condition cannot be easily checked.

Single lap joint geometry has been traditionally used as a control to justify changes in design towards improving static and fatigue performance. In many cases FEA is used to investigate the stress distribution differences within the bond for alternative joint geometries to better understand the effect of joint geometry on joint performance. For example, Zeng et al. [139] developed a wavy composite lap joint as an alternative to traditional lap joints or adhesive joint geometries with tapered edges to avoid the load eccentricity and the associated singular peel stresses at the joint ends. The wavy lap joint resulted in compressive peel stresses at the joint ends altering the failure progression so that there was no indication of damage initiation before final failure. Comparing this to the traditional lap joint, crack initiation was noticed from the load/displacement relationship and visual inspection of cracks. Avila et al [12] used FEA to make correlations between stress distributions in wavy lap joints and single lap joints with the failure loads in E-glass/epoxy composites. They noticed a 41% higher load carrying capacity for wavy lap joints over conventional single-lap joints attributed to a more uniform stress field with compressive peel stresses in the wavy lap joint. Fessel et. al [51] showed significant improvements in overall joint strength for the reverse-bent joint over the traditional lap shear joint for several steel alloy substrates with different overlap lengths. They used FEA to evaluate stress

distributions within the bond and discussed possibilities for improved joint strength by modifying joint geometries to achieve more uniform stress distributions instead of high localized stresses at the joint ends with a relatively unstressed central region. Borsellino et al. [30] showed for a given resin longer cure times correspond to a significantly stiffer, stronger resin as shown by stress-strain relations. The authors also showed some evidence of capturing stabilization by investigating changes in failure (adhesive/cohesive) mechanisms with extended curing times as viewed by surface inspections of failed single lap joints. The FE was used to evaluate internal stress distributions, and experimental evaluation was based on mechanical testing (flexural modulus, ultimate failure stresses, or impact resistance). Da Silva et al. [37] compared basic double lap geometries with an inside tape and adhesive fillet design with various resins using experimentally determined failure loads and FEA to evaluate the internal stress distributions due to combined temperature and mechanical loads using titanium and carbon fiber composites. Many experimental methods were used to evaluate overall joint performance based on more traditional mechanical testing and ultimate failure states.

1.3 Analytical and Numerical Studies

1.3.1 Nonlinear Anisotropic Micro-macromechanical Modeling

Many experimental and analytical studies have been focused on the nonlinear response of laminated composite materials. Macro-level theories are formulated to characterize the nonlinear response by idealizing the composite as an anisotropic homogeneous medium. Petit [102] proposed an incremental approach for the analysis of symmetric laminates under uniform membrane loading. In their approach, the elastic constants of a lamina are determined as a function of the lamina strains. Lamina failure is identified when any of its strain components exceeds the experimentally obtained limiting strain value. Once a failure mode is detected in the lamina, the

corresponding tangent stiffness is set to a high negative value in order to achieve stress unloading in this direction. Their analyses predicted the overall shape of the nonlinear response quite well, while the laminate ultimate failure loads were predicted with acceptable accuracy. Hahn and Tsai [55] used the complementary energy density polynomial function, for a lamina under a plane-stress state, to derive a nonlinear stress-strain relation for laminated composites. An additional fourth-order term of the axial-shear stress is added to the polynomial function. This term represents the nonlinear shear strain. Interaction terms between the three stress components were neglected. Hahn [54] extended this work to model the nonlinear behavior of laminates, and considered the effect of material nonlinearity on the buckling load of a symmetric laminate. Hashin et al. [67] formulated a new nonlinear constitutive model where inelastic transverse and axial shear strains exist in a lamina under plane stress conditions. Each inelastic strain component is an independent quadratic function in terms of the stress invariants raised to a general power. Ramberg-Osgood representation of nonlinear stress-strain curves was used to express the nonlinear axial-shear and transverse stress-strain relations. Predicted nonlinear behavior compared well with experimental results for different laminated composite materials. Jones and Nelson [77] proposed a material model based on strain energy that accounts for nonlinear behavior under biaxial states of stress. This model can only be applied to multi-axial stress states where the strain energy is lower than the maximum strain energy generated in the uni-axial test results. Since this is often the case when the composite is subject to general multi-axial stress states, different approaches were proposed to overcome this difficulty, Jones and Morgan [76], Abu-Farsakh [7]. Amijima and Adachi [10] introduced a simple technique to represent the shear nonlinearity using piecewise linear segments. Sandhu [112] introduced a technique for solution of the nonlinear laminate equations using piecewise cubic spline functions to represent the lamina uni-axial test data. He also proposed a predictor-corrector iterative

method. Nahas [99] presented a similar predictor-corrector technique in which the basic uni-axial stress-strain relations are allowed to have a general nonlinear representation. Kuppuswamy et al. [86] used the Richard and Abbott [106] representation for the nonlinear uni-axial stress-strain relations in a three-dimensional finite element analysis. However, their study uses uncoupled one-dimensional stress-strain relations which do not reflect interaction effects. Pindera and Herakovich [103] and Mathison et al. [96] derived a nonlinear plane stress constitutive model using orthotropic endochronic theory. This theory is based on irreversible thermodynamics with internal variables. Dvorak and Rao [45] proposed a plasticity theory for fibrous composites under axisymmetric deformation. Plastic dilatation and deformation of the composite in the fiber direction were accounted for. A yield function was formed using the stress invariants of a transversely isotropic material and simple hardening and flow rules were derived. Griffin [53] extended Hill's anisotropic plasticity theory, and used the associated plasticity flow rule to determine the plastic increment of strain. A Ramberg-Osgood uni-axial stress-strain relation was used to model nonlinear hardening. Sun and Chen [119] developed a one parameter orthotropic plasticity model for thermoplastic and metal-matrix composite laminates in plane stress. In this model, one-parameter plastic-potential scalar function is proposed. Only transverse and axial shear stresses are involved in the plastic potential; therefore, plastic deformation in the axial direction of the lamina is neglected. In addition, a power law relation between effective plastic strain and the effective stress is proposed; as a result, a total of three material parameters are needed to fully describe the lamina plastic behavior.

A nine-cell cohesive micromodel is developed similar to the doubly periodic multi-phase composite media fully described and reviewed by Aboudi [3,4,6], and is a simplified version of the more general case of the High Fidelity Generalized Method of Cells given by Haj-Ali [56]. The High Fidelity Generalized Method of Cells (HFGMC) is a computational nonlinear micromechanical model for multi-phase composites. A

more thorough review of the HFGMC model can be found in Aboudi [3] and in Haj-Ali and Aboudi [58] where the modified form now includes nonlinear algorithms with tailored stress correction schemes, iterative micromechanical solution methods for rapid error reduction, and multi-scale features extending the capabilities of the model for greater efficiency in capturing the local and global load re-distribution that is associated with nonlinear and damage effects in large-scale structural computational finite element models consisting of doubly periodic multiphase composite media. Classical nonlinear micromechanical models of multi-phase materials are capable of capturing the nonlinear effective response of the material but neglect the local spatial variation of the deformation fields within the representative microstructure. The HFGMC has the capability of predicting local nonlinear mechanical behavior of periodic multi-phase materials subject to remote loading through a modeling framework that allows for a detailed description of the constituents and spatial deformations between the phases. Multiphase composites are analyzed within the HFGMC framework with nonlinear elastic, elastoplastic and viscoplastic constituents Aboudi2004.

The HFGMC has been used to analyze fully coupled electro-magneto-thermo-elastic multi-phase composites [5], fiber-matrix debonding in metal matrix composites [19], thermomechanical analysis of internally cooled structures at elevated temperatures for aerospace engine applications [11], adhesively bonded composite joints [20], and internal pore pressure for the analysis of foam insulation of the external tank of the space shuttle [18].

Experimental and analytical studies have been performed to characterize the effective material properties and behavior of pultruded FRP composites. Herakovich and Mirzadeh [69] studied the effects of the spatial distribution of fibers and fiber volume content on the effective properties of pultruded graphite/epoxy composites. They observed that the fiber and resin rich area were distributed non-uniformly. In

addition they found fiber waviness, which reduces the stiffness and strength of the pultruded composites. Bank [15,16] used the Iosipescu shear test to characterize in-plane shear modulus and strength of glass fiber pultruded specimens having vinylester and polyester matrix. The specimens were cut from the webs and angles of wide-angle pultruded beams. Pronounced nonlinear stress-strain relations were shown. Wang and Zureick [130] characterized the tensile behavior of coupon specimens cut from different locations of a pultruded I-shaped beam. Flaws such as high void content and uneven distribution of reinforcement was significant in this material system. The specimen size effects on the effective properties were also examined. Tomblin and Barbero [126] performed analytical model to predict unidirectional compression strength of pultruded composites. Nonlinear responses were shown mainly due to fiber microbuckling. Nonlinear stress-strain behavior under multi-axial static loading can occur in pultruded FRP materials and structures. Haj-Ali and Kilic [59] conducted extensive off-axis tests finding a pronounced nonlinear material response evident in all off-axis angles of thick-section pultruded composites including the uniaxial specimen (0°). This material nonlinearity was attributed to the low fiber volume fraction (FVF) and behavior of the soft polymeric matrix.

1.3.2 Analytical and Computational Modeling of FRP Lap Joints

Hart-Smith [65] examined the effect of plasticity in the adhesive in FRP lap joints, an imbalance of the stiffness of the adherends, bond length, fiber stacking sequences, adherend thermal mismatches, and other effects in his analytical parametric study. Hart-Smith notes three distinct and characteristic failure modes in single lap joints: adherend failure due to in-plane stresses from the eccentricity in the load path, failure of the adhesive in shear, and failure of the adhesive due to peel stresses. Elastic studies have indicated that joint failure emanates from shear failure of the adhesive; however, the inclusion of adhesive plasticity in the analysis indicates that failure is associated

with adhesive peel stresses. If the interlaminar tension strength is lower than the peel strength; however adherend failure is expected. Hart-Smith [66] expanded this study to double-lap, single-lap, scarf and stepped-lap configurations under tensile, compressive, and in-plane shear load conditions covering joint parameters such as: adhesive plasticity (elastic-plastic shear stress model), adherend stiffness imbalance and adherend thermal mismatch. Again, he focused on failure modes such as the case when the adherend fails outside the joint (1), the ultimate shear strain of adhesive is exceeded resulting in bond failure (2), and peel stresses induced at ends of joint exceed the interlaminar tension strength of the laminate resulting in splitting failure of the adherend (3). The main modification suggested to alleviate these peel and shear stress intensity and failure mode is to taper the end of the outer adherend. Hart-Smith suggests that peel stresses are only a problem if joint efficiency is low; however, peel stresses are still important in more efficient joint types especially for fracture analysis. Dickson et. al [41] also developed a parametric study using closed form analyses, finite element analysis, and photoelasticity to verify their solutions. They included the effects of stress through the thickness of the adherends but neglected the effects of adhesive plasticity. Instead they chose to include a plastic zone approach in their analytical model which ignored the presence of peel stresses in the adhesive and assumed that shear stresses are constant in the zone as an approximation. Again, Dickson et. al focused on ultimate joint strength instead of failure initiation in this study. Lai et al developed a closed form solution to obtain fracture parameters for investigating debonding in the cracked lap shear joint problem. Their analytical method is compared to finite element results and fatigue experiments. The solution is similar to Goland and Reissner approach [52] for a classical single lap shear joint problem involving only linear behavior of the adhesive, but adds fracture parameters for investigating crack growth. Campilho et al. [32] investigated joint efficiency using a parametric finite element study on internal stress distributions for different overlap

lengths, plate thickness, and stacking sequences of single lap joints similar to Hart-Smith. The experimental part of their study focused mostly on ultimate failure stresses of the joints instead of failure initiation.

Although strength based approaches for failure in single lap joints [65, 66] has shown excellent correlation with experimental results, fracture mechanics approaches for fiber reinforced polymeric composites have gained more popularity in the past two decades [85]. Linear elastic fracture mechanics (LEFM) emerged from linear elasticity to solve for the stress and deformation fields around cracks in continuous media. These solutions and fracture-based material properties are used in design problems of materials and structures with defects. By using Westergaards elasticity solution [134], Irwin [72] shows that the stress field expansion near the crack tip is related to a constant multiplied by the coefficient of the square root of the distance from crack tip. This constant is called the stress intensity factor (SIF), K . The SIF is shown to be directly related to the strain energy release rate. Sih, Paris and Irwin [115] employ Lekhnitskii's [88] solution to relate strain energy release rate to the SIFs for anisotropic materials. The mixed-mode case in absence of the tearing mode is also presented. They show that for anisotropic materials where the crack is aligned in one of the material symmetries, the SIF in mode-I and II are not coupled. In the case where the crack is not aligned with material symmetry, the SIFs are both coupled and need to be solved simultaneously. Dally and Sanford [38] propose an experimental method to determine the mode-I SIF in isotropic materials using a strain gauge. The Westergaard stress function [134] is used to calculate the mode-I SIF based on strain gauge measurements. To obtain an accurate SIF, they determine the optimal location and orientation of the strain gauge needed to eliminate the effect of non-dominant terms and increase the contribution of the mode-I SIF. Shukla et al. [114] extend Dally and Sanfords method to orthotropic materials. They use Airys function for a two-dimensional orthotropic body and solve for the strain field equations. Rybicki

and Kanninen [111] develop a virtual crack closure technique (VCCT) to evaluate the SIFs. The technique is based on the crack closure integral, which can be used in a finite element analysis (FEA) with a coarse mesh. Damage onset and growth in composite components at material or geometric discontinuities is related to Mode I, II, and III delaminations. Different mixed mode fracture criterion has been developed for crack growth due to a combination of Mode I and Mode II delaminations. The Virtual Crack Closure Technique (VCCT) criterion uses the principles of linear elastic fracture mechanics (LEFM) and, therefore, is appropriate for problems in which brittle crack propagation occurs along predefined surfaces. VCCT is based on the assumption that the strain energy released when a crack is extended by a certain amount is the same as the energy required to close the crack by the same amount. Stroud et. al [84] used fracture mechanics and probabilistic analyses to investigate the strength of a single lap joint exploring the effects of configurational and material uncertainties on the strength of a single lap shear joint.

1.3.3 Fatigue Damage Models for FRP Composites

Spatial damage distributions during fatigue experiments of uniform samples are usually scattered in part due to the material heterogeneity. A probabilistic damage approach is therefore advantageous over a deterministic method in order to account for the relatively wide variability of test results. Bogdanoff et al. [26–29] were the first to introduce a new cumulative damage model using stochastic processes. A Markov chain model was used to take into account the variability (e.g., manufacturing and service loads). They further pointed out that the life testing in which time to failure was recorded does not provide enough information for the member function (mf) behavior. Thus, they divided the probability transition matrix into different segment numbers to improve accuracy. Results of different probabilities in the transition matrix of the Markov chain model were investigated analytically. They

compared previous experimental work done by other researchers with Markov chain models. Bogdanoff and Kozin [28] called the cumulative damage model the B-model and converted it to a nonstationary model using a time transformation condensation method. Polynomial equations were used for mapping the time in different domains. To maintain the definition of the transition matrix, a condensation method was used in their models. This allows the stationary Markov chain to become a nonstationary model. Kozin and Bogdanoff [83] employed the B-model together with the Paris law to describe the fatigue process. Rowatt and Spanos [110] applied a cumulative damage model to laminated composite materials. The time transformation condensation method was also employed in their work. They investigated the evolution of compliance in composite materials subjected to a constant amplitude fatigue loading. The change in compliance was related to the individual damage mechanisms of a critical element within the laminate to achieve a life prediction of the material system. Their experimental data was based on a single mid-specimen axial extensometer measured in a straight composite coupon. Xi et al. [108, 137] used a cumulative damage model together with the R-curve to predict the damage evolution of a three point bend concrete beam. They used a geometric series to generalize transition probabilities in Bogdanoff and Kozins approach. A recursive expression was proposed to obtain the probabilities in the transition matrix. The R-curve was obtained in order to provide the crack extension, which was required in the recursion, for a specific specimen geometry and given loading conditions. Wu and Ni [136] studied three different damage approaches: Markov chain model, Yangs power law model, and a polynomial model for fatigue crack growth. They performed constant and random amplitude loadings on aluminum alloy compact tension C(T) fracture specimens, and they used the three models to predict the fatigue behavior of the specimens. For the case of random loading, the polynomial model fitted the experiments better than the Yangs model. They pointed out that the nonstationary Markov chain model was sufficient to describe the

fatigue process and also suitable for random loading. Tanimoto [124] applied different stress levels to carbon/epoxy laminates and observed that the fatigue life had more scatter in the 10⁵-10⁶ cycle range. A Weibull probability model was used to construct the probability of failure at different stress amplitudes through the fatigue life. The dominate failure mode was delamination. Liu and Mahadevan [94] utilized Monte Carlo simulations combined with Miners rule that took into account the coefficients in Tsai-Hill failure criterion in order to estimate the fatigue life of composite laminates. They assumed the random variable such as ply thickness, elastic modulus, and ply angle as normal distribution for Monte Carlo simulations. Their numerical method had good agreement with the experiments conducted by Mandell and Samborsky [95]. Liu and Mahadevan [89] employed a nonlinear fatigue damage accumulation method with a stochastic S-N curve technique to predict the fatigue life of metallic materials under various stress levels. The fatigue data was obtained from the literature for different materials with variable or constant amplitude loadings. A required coefficient for formulating the nonlinear damage accumulation rule was calibrated with the experimental fatigue data. The coefficient accounted for material properties and applied stress levels, which were not usually considered in a typical linear damage accumulation rule. The Karhunen-Loeve expansion method [90] was conducted to generate their stochastic S-N curves. Numerical simulations using the proposed damage method yielded satisfactory agreement with the experimental fatigue life. The majority of proposed cumulative damage models used to evaluate material behavior under fatigue are mainly based on traditional contact based measurements, including strain gauges and extensometers. Rowatt and Spanos [110], for example, used extensometer data gathered from 17 coupons to investigate changes in compliance that was related to the stochastic evolution of fatigue damage in composite materials. Wu and Ni [136] used dial gages to measure fatigue crack growth in metallic C(T) specimens. Traditional contact based may not be practical for all specimen geometries, and

non-traditional tools may also be more sensitive to damage especially in composite joints. Tamuzs et al. [122,123] conducted fatigue tests on woven orthotropic composite laminates in off-axis loadings. They developed a quadratic master curve function to describe the strength, deformation, and degradation of the stiffness. This master curve was obtained by the best fit of the experimental data through the fatigue life of the laminates, and showed that the reduction of the stiffness before fatigue failure does not depend on the loading angles with respect to the material angles. An S-N master curve was also developed by replacing the applied stresses in the conventional S-N curve with a modified stress function. The S-N master curve was an innovative alternative way of representing damage accumulation using a stochastic approach. However, the variability in composite fatigue data was not fully accounted for.

1.4 Objective

The objective of this manuscript is to develop new experimental and computational methods for analyzing the behavior of FRP composites. For the experimental part of this study, quantitative methods using Thermoelastic Stress Analysis and other experimental methods are developed for validating new computational modeling approaches for a new class of materials. Jute hybrid bio-composites were chosen for the experimental and analytical part of this study. Nonlinear anisotropic micro and macromechanical models were developed to capture the multi-axial response of the material. The last part of this manuscript is focused on new quantitative methods for analyzing lap joints using TSA. First, lap joints are tested statically, and changes are correlated with real damage effects using photomicroscopy. Then, stochastic methods are developed with new methods for processing in-situ TSA cumulative fatigue data.

1.5 Present Study

Chapter 2 of the present study develops a quantitative thermoelastic strain analysis method for composite materials. El-Hajjar and Haj-Ali verified fracture mechanics computational models for thick-section pultruded E-glass/polyester and E-glass/vinylester composites with experiments using this quantitative strain analysis method. In chapter 2 this study provides this thermomechanical calibrations for prepreg S2glass/epoxy, Carbon/epoxy, and pultruded E-glass/polyester. This work is then extended to a new class of materials investigating the linear and nonlinear mechanical behavior of Jute hybrid bio-composites, and new nonlinear micromechanical and macromechanical modeling approaches are developed for the analysis of the materials. Two of these nonlinear anisotropic homogeneous models assume that the material is under a state of plane stress. The third is a nonlinear 3D micromechanical model using a Nine-Cell micromechanical model, a special case developed by Haj-Ali [56] of the more general High Fidelity Generalized Method of Cells (HFGMC). The HFGMC micromechanical modeling framework was proposed by Aboudi [101] and later modified by Haj-Ali and Aboudi [58] to include nonlinear algorithms with tailored stress correction schemes, iterative micromechanical solution methods for rapid error reduction, and multi-scale features extending the capabilities of the model for greater efficiency in capturing the local and global load re-distribution that is associated with nonlinear and damage effects in large-scale structural computational finite element models consisting of doubly periodic multiphase composite media. The models from are calibrated from uniaxial experiments and validated in the third part of this study with Thermoelastic Stress Analysis (TSA) and Digital Image Correlation (DIC) for a full-field stress-strain analysis of plates with a hole. Tests are conducted to generate the stress-strain nonlinear response up to ultimate failure and three nonlinear constitutive material models are used to predict the multi-axial stress-strain behavior of bio-composites. Chapters 4 and 5 cover damage in FRP single lap

joints using TSA. Future damage detection techniques in aging aircraft will require quantitative and noncontact nondestructive evaluation (NDE) methods especially for composite components. Infrared (IR) thermography techniques have been qualitatively used to assess and indirectly infer the durability of structural systems. IR-NDE tests to ascertain the health and integrity of the structure over time, especially around connection areas and other critical locations where potential damage can occur. Quantitative NDE-IR methods have received limited attention, especially in composite materials, because these require rapid data acquisitions and signal processing coupled with high resolution and full-field IR. These are past limitations of electronic hardware and the software. One objective of this research was to examine composite components under loading and extract deformation measures from the emitted IR field of the tested components. A research collaboration with Lockheed Martin for non-destructive evaluation of composite lap shear joints led to a development of thermoelastic stress analysis techniques for evaluation aerospace structures. Chapter 4 presents a study on infrared thermography for failure initiation and progression in composite lap shear joints. This study also presents some generic finite element results for analyzing bond characteristics in lap joints.

Chapter 5 expands on the previous chapter by implementing TSA on FRP single lap joints for fatigue damage. IR-TSA techniques are employed to capture cumulative fatigue data and a damage index is defined for the quasi-isotropic S2-glass/E733FR composite lap-joints subjected to constant amplitude fatigue loading. Markov chain models are employed with the TSA damage index to predict fatigue behavior for a maximum stress corresponding to 65% and 55% of the ultimate stress. Next, new stochastic S-N curves utilizing the calibrated Markov damage model are also introduced. The TSA and mechanical testing setup and test procedures are first discussed. The proposed IR-TSA damage index is defined based on the area reduction of stresses. The numerical results from the experiments are then utilized along with

Markov chain theories to predict the fatigue behavior in S2-glass/E733FR lap-joints. Chapter 5 presents infrared thermography for fatigue damage detection in FRP composites with stochastic methods for analyzing this fullfield data. Chapter 6 presents the major outcome of this study and future work.

CHAPTER II

THERMOELASTIC STRESS ANALYSIS FOR QUANTITATIVE ANALYSIS

2.1 Methodology

A experimental thermoelastic stress/strain analysis (TSA) technique is presented to measure normal stresses or the sum of the normal surface strains in FRP composites. The method proposed by El-Hajjar and Haj-Ali [48] can be used to verify computational models by providing a full-field measurement of the strain (or stress) invariant. This chapter will present the derivation for this quantitative TSA method, steps to acquire a thermomechanical calibration constant, and a verification of a computational models under a multi-axial state of stress for different material systems under different loading frequencies. This work is presented as a continuation of the work from the Master's Thesis by Shane Johnson [73], and this experimental work is presented here serving as a basis for utilizing TSA as a quantitative method for verifying computational models under multi-axial states of stress. All the experimental work in this section is was newly acquired to verify the accuracy of the method with different material systems and at different frequencies and stress or strain ranges. In addition to this method, the same experimental calibration is executed without the surface coating to show that two calibration constants would then be required for an orthotropic composite. Derivation is also introduced for the case of an uncoated multi-layered composite. This derivation was used with Lekhnitskiis elasticity solution to quantify the full strain field and determine mixed-mode stress intensity factors (SIFs) for crack tips in composite plates subjected to off-axis loading in the fracture study by Haj-Ali et al [62].

In general, to obtain the thermomechanical calibration constant the composite material tested is given an isotropic surface coat that experiences the same in-plane strain conditions as the individual lamina in a perfectly bonded laminate or pultruded composite. During the calibration, the infrared (IR) signal from the coat is measured, and strains in the axial and transverse loading directions are recorded while the specimen under a uniform state of stress is cyclically loaded. This quantitative thermoelastic strain analysis method allows a single material constant, comprised of the thermomechanical properties of the composite, to be calibrated such that the measured IR signal can be related to the sum of the in-plane strains. The theoretical derivation of this method developed by El-Hajjar and Haj-Ali [48] assumes steady state, adiabatic conditions and is applied to the case of multi-layered composite materials. The proposed method is validated by its application to Carbon/epoxy, S2-glass/epoxy, and thick-section E-glass/polyester composites under multi-axial states of stress.

2.2 Derivation

The proposed formulation directly relates the TSA signal to the sum of the direct strains in a coated, layered composite medium. A perfect bond is required for the validity of the method because at each material point the same in-plane strains must be experienced by the surface coating and individual laminae, and debonded sections of a composite would cause non-adiabatic effects like friction and rubbing. The thermomechanical material response of the isotropic surface coating is considered linear elastic and independent of the mean applied stress and loading frequency where the axial and transverse coefficients of thermal expansion are equivalent. Figure 1 schematically illustrates a typical layered composite with surface coatings and different orthotropic layers. If the elastic stiffness of the coat is small compared to the overall stiffness, the measured mechanical response is primarily due to the substrate. While assuming that the surface coating is responsible for the thermoelastic

response ($\alpha_1 = \alpha_2$), the TSA signal is interpreted to represent the change in the sum of the direct in-plane strains of each layer. The new material constant that is derived relates the TSA signal to the change of the in-plane strains and can be calibrated experimentally from TSA measurements on specimens under a uniform state of stress when the in-plane strains are known. In-plane strains are easily measured during the calibration with a bi-axial strain gauge mounted on the back surface of the same specimen under a uniform state of stress.

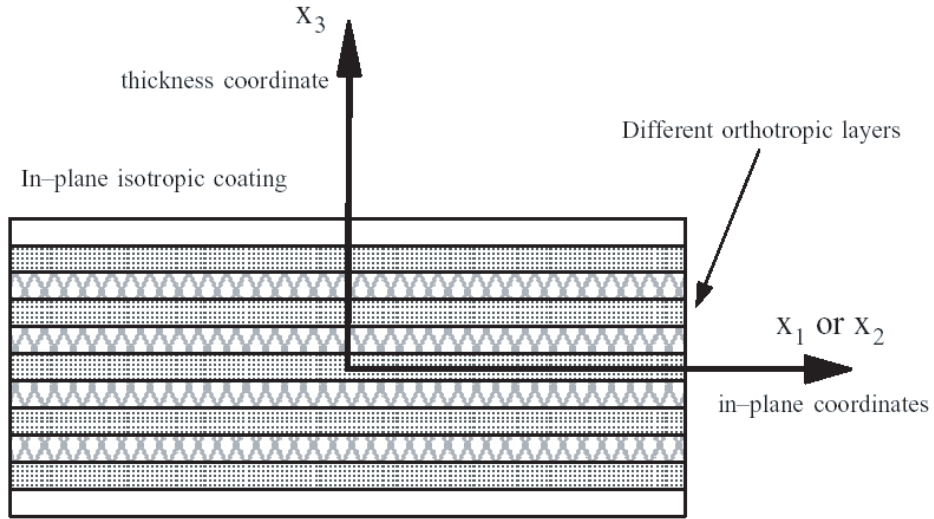


Figure 1: Schematic cross-sectional view of a layered orthotropic composite with surface coatings

Displacement continuity is assumed between the individual laminae to account for the same in-plane strains in all the layers when a uniform in-plane loading is applied during the thermomechanical calibration. Assuming traction continuity results in equivalent uniform out-of-plane stresses with the composite and surface coating layer. The 3D lamination theory developed by Pagano [100], is used in this formulation to enforce traction and displacement continuity between individual laminae while accounting for equivalent linear anisotropic stress-strain relations for the substrate. A basic equation governing the thermoelastic effect is given by Wong et al. [135]:

$$Q_{i,i} = T \frac{\delta \sigma_{ij}}{\delta T} \dot{\epsilon}_{ij} - \rho_o C_\epsilon \dot{T} + \rho_o \dot{R} \quad (1)$$

Where Q_i is the heat flux through the surface whose outward directed normal is n_i , T is temperature, σ_{ij} is the stress tensor, ϵ_{ij} is the strain tensor, ρ_o is the density, C_ϵ is the specific heat at constant deformation, and \dot{R} is the heat production rate per unit mass of the internal heat sources. The thermomechanical constitutive law for a linear anisotropic material is given by Hookes law:

$$d\sigma_{ij} = C_{ijkl} d\epsilon_{kl} - C_{ijmn} \alpha_{mn} dT \quad (2)$$

Where, C_{ijkl} is the fourth rank tensor of the material constants, α_{mn} are the coefficients of thermal expansion and dT is the change in temperature. If the material properties are assumed to remain constant with change in temperature, then the stress change in temperature is simply:

$$\frac{\delta \sigma_{ij}}{\delta T} = -C_{ijmn} \alpha_{mn} \quad (3)$$

Assuming adiabatic conditions and the absence of internal heat sources, the heat flux through the surface $Q_{i,i} = 0$, and the specific heat at constant deformation $\dot{R} = 0$, Equations 3 and 1 are combined to give:

$$\rho_o C_\epsilon \frac{\dot{T}}{T} = -C_{ijmn} \alpha_{mn} \dot{\epsilon}_{ij} \quad (4)$$

Next, assuming small strain theory, and using the incremental form of Equation 2 to express for $C_{ijmn} d\epsilon_{ij}$, Equation 4 is rewritten as:

$$\rho_o C_\epsilon \frac{dT}{T} = -\alpha_{mn} [d\sigma_{mn} + C_{mnpq} \alpha_{pq} dT] \quad (5)$$

For the special case of an in-plane transversely isotropic coat under a state of plane stress, the in-plane material properties are equal, $\alpha_{11} = \alpha_{22} = \alpha$, $C_{11pq} = C_{22pq}$, $d\sigma_{33} = 0$. Placing theses conditions on Equation 5, it is then seen that the thermoelastic effect is dependent only on the in-plane properties:

$$\left[\frac{\rho_o C_\epsilon}{T} + C_{mnpq}\alpha_{mn}\alpha_{pq}\right]dT = -(\alpha_{11}d\sigma_{11} + \alpha_{22}d\sigma_{22}) = -\alpha(d\sigma_{11} + d\sigma_{22}) \quad (6)$$

The general, the stress-strain relation for the in-plane isotropic surface coating is:

$$\begin{bmatrix} \sigma_{11} \\ \sigma_{22} \\ \sigma_{33} \\ \tau_{23} \\ \tau_{13} \\ \tau_{12} \end{bmatrix} = \begin{bmatrix} C_{11} & C_{12} & C_{13} & 0 & 0 & 0 \\ C_{12} & C_{11} & C_{13} & 0 & 0 & 0 \\ C_{13} & C_{13} & C_{33} & 0 & 0 & 0 \\ 0 & 0 & 0 & C_{44} & 0 & 0 \\ 0 & 0 & 0 & 0 & C_{44} & 0 \\ 0 & 0 & 0 & 0 & 0 & (C_{11} - C_{12})/2 \end{bmatrix} \begin{bmatrix} \epsilon_{11} \\ \epsilon_{22} \\ \epsilon_{33} \\ \gamma_{23} \\ \gamma_{13} \\ \gamma_{12} \end{bmatrix} \quad (7)$$

The plane stress assumption in this layer enables expressing the out-of-plane strain ϵ_{33} in terms of the in-plane strain components:

$$\epsilon_{33} = -\frac{C_{13}}{C_{33}}(\epsilon_{11} + \epsilon_{22}) = -\frac{C_{13}}{C_{33}}\epsilon_{\alpha\alpha}; \alpha = 1, 2 \quad (8)$$

Therefore, the first stress invariant can be expressed as:

$$\Delta\sigma = \sigma_{\alpha\alpha} = \sigma_{11} + \sigma_{22} = \frac{(C_{11}C_{33} + C_{12}C_{33} - 2C_{13}^2)}{C_{33}}(\epsilon_{11} + \epsilon_{22}) \quad (9)$$

From an experimental perspective, the infrared detector measures an un-calibrated TSA signal, S , that is linearly related to the radiant photon flux emitted due to a surface temperature change ($S \propto \frac{\Delta T}{T} \propto \Delta\sigma$). Equation 6 can be used to relate the

TSA signal to the incremental change of the first stress invariant through a parameter k_σ :

$$\Delta\sigma = k_\sigma S \quad (10)$$

Substituting Equation (9) into (10) results in:

$$\frac{(C_{11}C_{33} + C_{12}C_{33} - 2C_{13}^2)}{C_{33}}(\Delta\epsilon_{11} + \Delta\epsilon_{22}) = k_\sigma S \quad (11)$$

Next, the above elastic constants of the surface layer are used to relate the TSA signal to the direct in-plane strains instead of the stress invariant. This is important since all orthotropic layers have the same in-plane strains in a medium subjected to in-plane loading. A new constant k_ϵ can then be defined as:

$$k_\epsilon = \frac{C_{33}}{(C_{11}C_{33} + C_{12}C_{33} - 2C_{13}^2)}k_\sigma \quad (12)$$

This enables formulating a new thermoelastic equation, similar to Equation 10, in terms of the in-plane strains using the new relationship:

$$\Delta\epsilon_{\alpha\alpha} = k_\epsilon S; \quad \alpha = 1, 2 \quad (13)$$

For a composite material with an orthotropic top surface and no surface coating, Eq. (6) cannot be used (i.e., no scalar relation exists between the sum of stresses and the temperature gradients for the orthotropic case). Two separate material coefficients are now needed. Therefore, Eq. (6) can be rewritten for an orthotropic case in the form:

$$dT = A_1 \cdot \sigma_{11} + A_2 \cdot d\sigma_{22} \quad (14)$$

In order to calibrate the above two constants, the stresses can be replaced by strains.

$$dT = A_1 \cdot (C_{11}\epsilon_{11} + C_{12}\epsilon_{22} + C_{13}\epsilon_{33}) + A_2 \cdot d(C_{12}\epsilon_{11} + C_{22}\epsilon_{22} + C_{23}\epsilon_{33}) \quad (15)$$

where the C_{ij} is the material orthotropic stiffness. Imposing a state of plane stress, the stress-strain relations of an orthotropic material can be expressed as:

$$\begin{Bmatrix} \partial\sigma_{11} \\ \partial\sigma_{22} \\ \partial\tau_{12} \end{Bmatrix} = \begin{bmatrix} Q_{11} & Q_{12} & 0 \\ Q_{12} & Q_{11} & 0 \\ 0 & 0 & Q_{66} \end{bmatrix} \begin{Bmatrix} \epsilon_{11} \\ \epsilon_{22} \\ \gamma_{12} \end{Bmatrix} \quad (16)$$

The out-of-plane strain ϵ_{33} can be expressed as:

$$\epsilon_{33} = -\frac{\nu_{13}}{E_{11}}\sigma_{11} - \frac{\nu_{23}}{E_{22}}\sigma_{22} = -\left(\frac{\nu_{13}}{E_{11}}Q_{11} + \frac{\nu_{23}}{E_{22}}Q_{12}\right)\epsilon_{11} - \left(\frac{\nu_{13}}{E_{11}}Q_{12} + \frac{\nu_{23}}{E_{22}}Q_{22}\right)\epsilon_{22} \quad (17)$$

Therefore,

$$\epsilon_{33} = B_1\epsilon_{11} + B_2\epsilon_{22}; B_1 = -\left(\frac{\nu_{13} + \nu_{12}\nu_{23}}{1 - \nu_{12}\nu_{21}}\right); B_2 = -\left(\frac{\nu_{13}\nu_{21} + \nu_{23}}{1 - \nu_{12}\nu_{21}}\right) \quad (18)$$

Substituting Eq. 15 into Eq. 18 yields:

$$dT \equiv S = H_1 \cdot d\epsilon_{11} + H_2 \cdot d\epsilon_{22} \quad (19)$$

$$H_1 = (A_1 \cdot C_{11} + A_2 \cdot C_{12} + A_1 \cdot B_1 \cdot C_{13} + A_2 \cdot B_1 \cdot C_{23}) \quad (20)$$

$$H_2 = (A_1 \cdot C_{12} + A_2 \cdot C_{22} + A_1 \cdot B_2 \cdot C_{13} + A_2 \cdot B_2 \cdot C_{23}) \quad (21)$$

Equation (19) implies that one can calibrate the coefficients, H_1 and H_2 , separately and apply superposition, assuming that application of the model remains in the linear range of the material.

In the axial direction, Eq. (19) can be expressed in terms direct strains:

$$S = (H_1 - \nu_{21}H_2) \cdot d\epsilon_{11} = k_1 \cdot d\epsilon_{11} \quad (22)$$

Likewise, in the transverse direction,

$$S = (-\nu_{12}H_1 - H_2) \cdot d\epsilon_{22} = k_2 \cdot d\epsilon_{22} \quad (23)$$

Solving Eqs. (22,23) yields:

$$H1 = \frac{\nu_{21}k_2 + k_1}{1 - \nu_{12}\nu_{21}}H2 = \frac{k_2 + \nu_{12}k_1}{1 - \nu_{12}\nu_{21}} \quad (24)$$

where k_1 and k_2 are the slope of experimental calibration curves for TSA signal vs ϵ_{11} and TSA signal vs ϵ_{22} . For a general plane stress case, the TSA signal can be expressed as the general case in Eq. (19).

2.3 IR Test Setup

A DeltaTherm DT1500 thermoelasticity measurement system was used to acquire the thermal measurements. The DeltaTherm's infrared array detector synchronized with the applied cyclical loading enables the detection of the transient thermoelastic effect. The infrared detector acts as a transducer, which converts the incident radiant photon flux into electrical signals. A lock-in analyzer (a signal-processing unit) extracts the thermoelastic information from the detectors output signal by using the reference signal from the loading device. The TSA-IR system uses the reference signal to reject any non-stress related thermal emissions. The frequency should be high enough to prevent heat transfer due to stress gradients during the load cycle. The Delta-Therm has a thermal resolution of at least 1 mK for image exposure times of one minute or less. Figure 2 shows a schematic for the testing setup testing setup, and Figure 3

shows the experimental setup for the thermomechanical calibration. The IR camera captures images at rates of more than 400 frames per second. The applied load signal is used to integrate synchronized TSA images that correspond to peak values of loading. The integration of the captured images is a temporal smoothing process performed over a specified period. In this study, a period of 1-2 min was used. The cyclic load was applied using an MTS 810 servo-hydraulic test system with a 22.2 kN(50 kip) capacity. The accuracy of the recorded strains is within 50 microstrostrains and the load is within 0.22 kN (50lb).

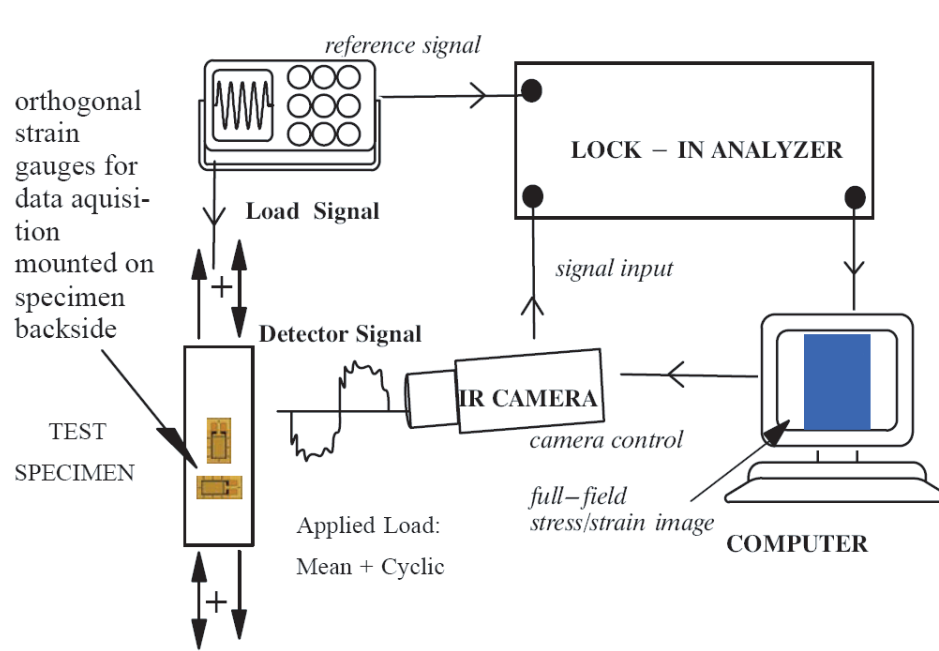


Figure 2: Schematic of TSA Setup for thermomechanical calibration

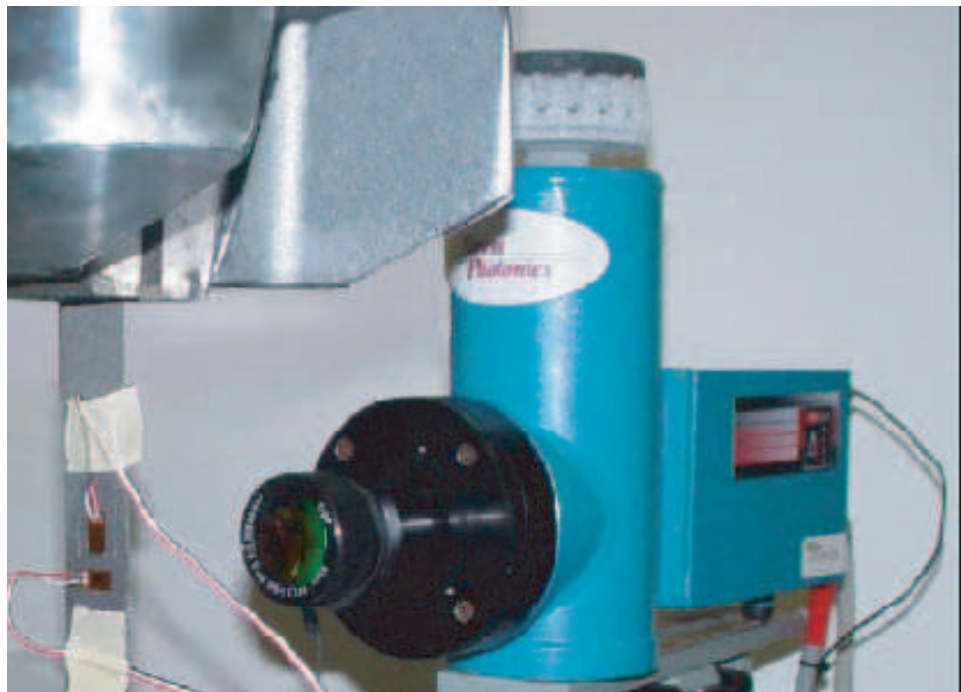


Figure 3: Setup for Thermo-mechanical calibration

2.4 Validation of TSA Technique on Prepreg and Pultruded Composites

The proposed TSA method was calibrated for Eglass/polyester pultruded, S2glass/epoxy prepreg, and Carbon/Epoxy FRP composite systems. The FRP coupons were tested with the load applied parallel and transverse to the major stiffness axis. The mechanical properties of the tested coupons are shown in Table 1. The Eglass tension coupons were 25.4 mm (1.00 in.) wide, had 152.4 mm (6 in.) ungripped length and a thickness of 12.2 mm (0.48 in.). The S2glass tension coupons were 25.4 mm (1.00 in.) wide, had 152.4 mm (6 in.) ungripped length. A uniform thickness of 2.26 mm (0.089 in) was achieved for the $[0_5/90/0_5]$ system using an autoclave, and a uniform thickness of 1.78 mm (0.070 in) was achieved for the quasi-isotropic system using an autoclave. The unidirectional Carbon/epoxy tension coupons were 25.4 mm (1.00 in.) wide, had 152.4 mm (6 in.) ungripped length and a thickness of 1.16 mm (0.046 in.). Biaxial strain gages were oriented in the material directions to measure the surface strains. The TSA effect was calibrated for the linear elastic region of the stress-strain response curve (< 0.25). Time effects on the stress-strain response during each cyclic load application were not considered significant and the material was assumed to be under steady-state conditions. The effective properties of the Pultruded E-Glass/Epoxy system in Table 1 were obtained by Haj-Ali and El-Hajjar [48]. For more details on the stress-strain response of these systems, see Johnson [73].

Table 1: Effective Elastic Properties

System	E_{11} , GPa (Msi)	E_{22} , GPa (Msi)	G_{12} , GPa (Msi)	ν_{12}
Pultruded E-Glass/Epoxy	17.1 (2.484)	9.96 (1.444)	3.5 (0.507)	0.283
Carbon/Epoxy	120. (17.46)	10.5 (1.235)	6.9 (1.010)	0.333
S2Glass/Epoxy $[0_5/90/0_5]$	49.4 (7.168)	17.3 (2.830)	13.6 (1.976)	0.229
S2Glass/Epoxy $[-45/0/45/90]_s$	26.7 (3.879)	26.7 (3.879)	17.5 (2.536)	0.307

2.5 Thermomechanical Calibrations for Various FRP Composites

A calibration shown in Figure 4 was repeated in this study for the pultruded system used by Haj-Ali and El-Hajjar in [48]. The thermomechanical constant obtained in this study is 9.8 % lower than the value obtained by their group, $k_\epsilon = 5.5973 \times 10^4$ camera units/(in/in). The difference may be due to differences in the numerical algorithms used to obtain TSA averages for the specimen, ways of processing the strain data to calculate, degradation of the camera sensors over time, or variability and differences in manufacturing of the pultruded E-glass/epoxy plates.

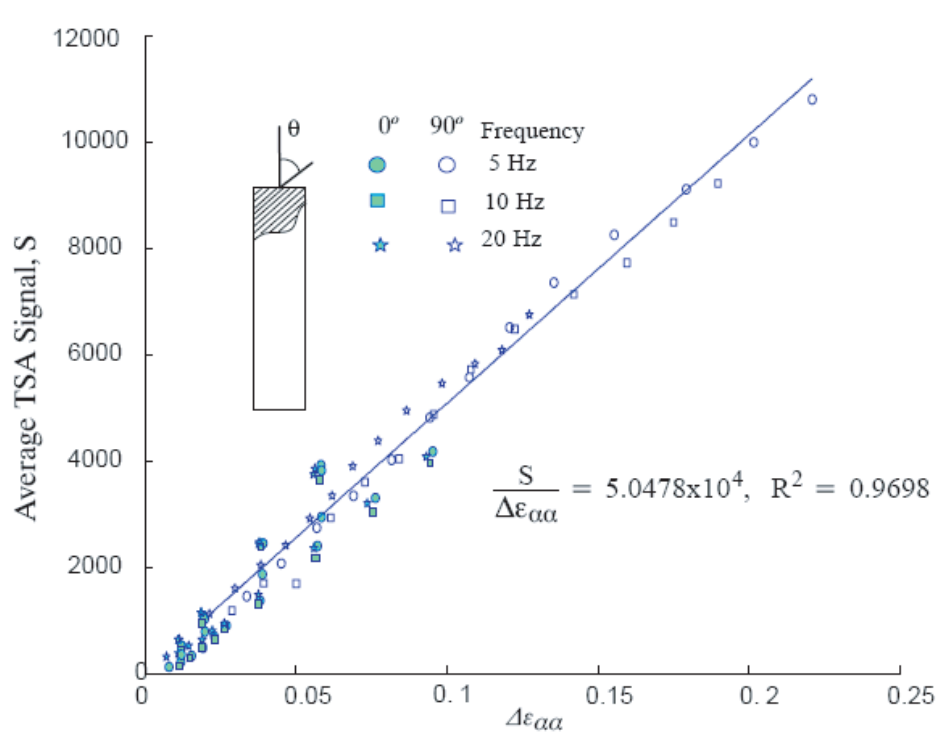


Figure 4: Thermo-mechanical calibration for E-glass/epoxy

Next, a unidirectional carbon/epoxy system is investigated. Notice in the calibration in Figure 5 that the 90° specimens show a slightly different slope than the 0° specimens. One should be aware of verifying computational models 2 distinct calibration constants. The thickness of the surface coat should be considered in this

case. It may be necessary to characterize certain layups with 2 calibration constants especially if a proper isotropic coat is not applied. Also notice in Figure 5 that a small number of data points were taken at high frequencies for the larger change in strain values. This is because the MTS machine was not tuned for each frequency. The error in the change in force applied to the specimen was neglected since the relation is in terms of the change in the sum of measured strains and TSA signal.

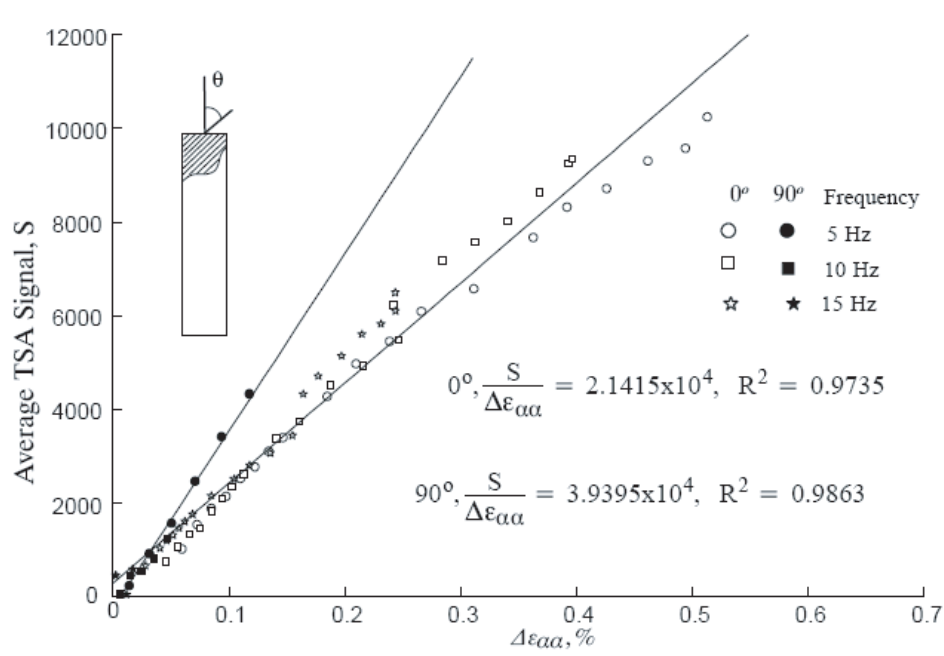


Figure 5: Thermo-mechanical calibration for Uncoated Carbon/Epoxy

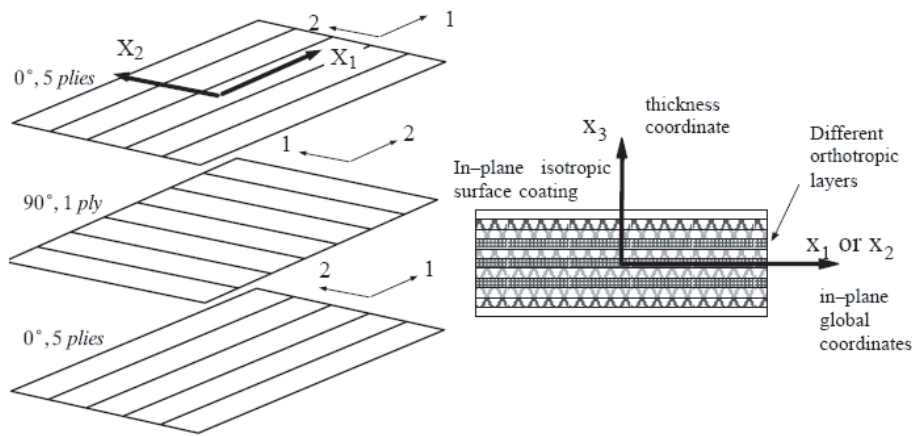


Figure 6: Schematic showing the lay-up for $[0_5/90/0_5]$

Notice in the calibration in Figure 7 that the 90° specimens show a different slope than the 0° specimens. The thickness of the surface coat should be considered in this case. It is necessary to characterize this layups with 2 calibration constants or apply an isotropic coat. An additional epoxy coating of approximately 0.3 mm (0.12 in) was cured at room temperature to the surface of the $[0_5/90/0_5]$ layup. This surface coat was then sprayed with flat black paint and the calibration from Figure 4 was repeated, and the result is shown in Figure 8. As you can see the isotropic surface coat allows the system to be characterized by a single constant that relates the Thermoelastic signal to the sum of the normal strains.

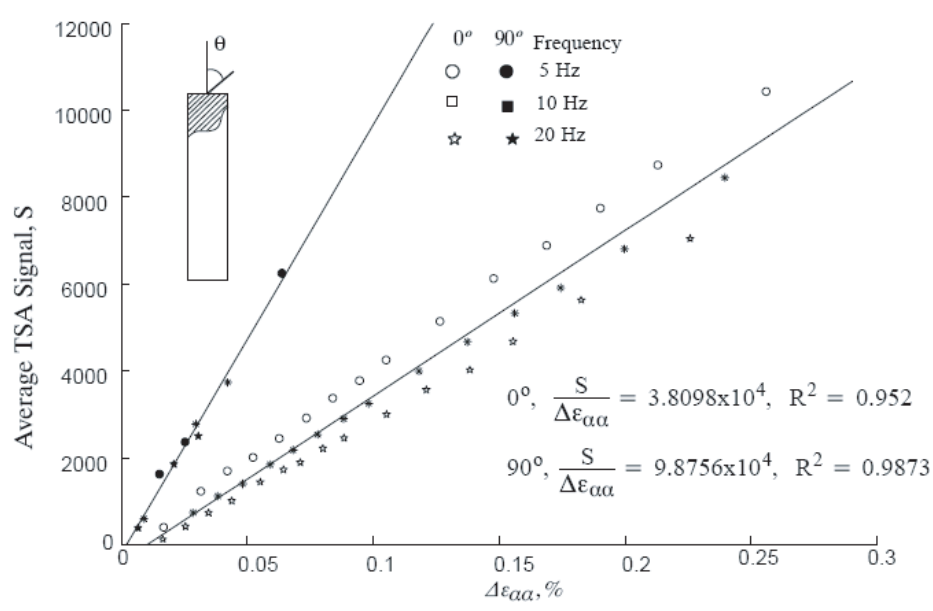


Figure 7: Thermo-mechanical calibration for uncoated S2glass/Epoxy for the $[0_5/90/0_5]$ Lay-up

The longitudinal stiffness of the $[0_5/90/0_5]$ system was measured to provide validity to the assumption of the negligible stiffness difference in adding the epoxy coating. Table 1 shows the values of the standard $[0_5/90/0_5]$, while the properties obtained from the epoxy coated samples are $E_{11} = 42.3$ GPa (6858 ksi) and $E_{22} = 20.4$ GPa (2957 ksi), respectively. These values are within five percent different than that obtained from uncoated specimens. This change of stiffness due to the epoxy

coat can be considered within the experimental error range and justifies using the proposed coat for TSA measurements. The calibration constant labeled All Fiber Directions, $K_\epsilon = 3.2477 \times 10^4$, will be used to validate different coated material systems to show that the epoxy coating is being calibrated in Figure 8. Figure 9 shows the thermomechanical calibration repeated for a quasi-isotropic S2-glass/Epoxy with a $[-45/0/45/90]_s$ layup scheme. This layup was chosen because the surface ply is orientated at -45 degrees from the loading axis. This surface ply tends to change the orientation of the thermoelastic signal with the angle of the surface ply. Two different quasi-isotropic lay-ups should theoretically have globally identical strain field. Bakis et al. [14] showed that two quasi-isotropic laminates resulted in different measured thermoelastic emission patterns for different stacking sequences. Adding an isotropic surface coat to the quasi-isotropic laminate acts as a strain witness. Two different quasi-isotropic lay-ups with the same added isotropic surface coating should theoretically have the same thermoelastic emission pattern for different stacking sequences. The thickness of the surface coat is the subject for future research.

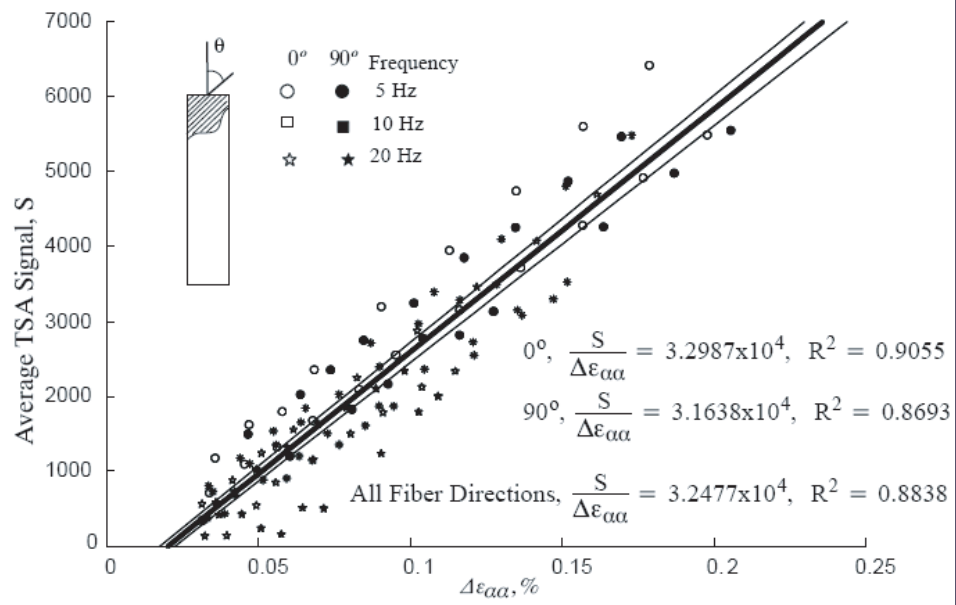


Figure 8: Thermo-mechanical calibration for coated S2-glass/epoxy

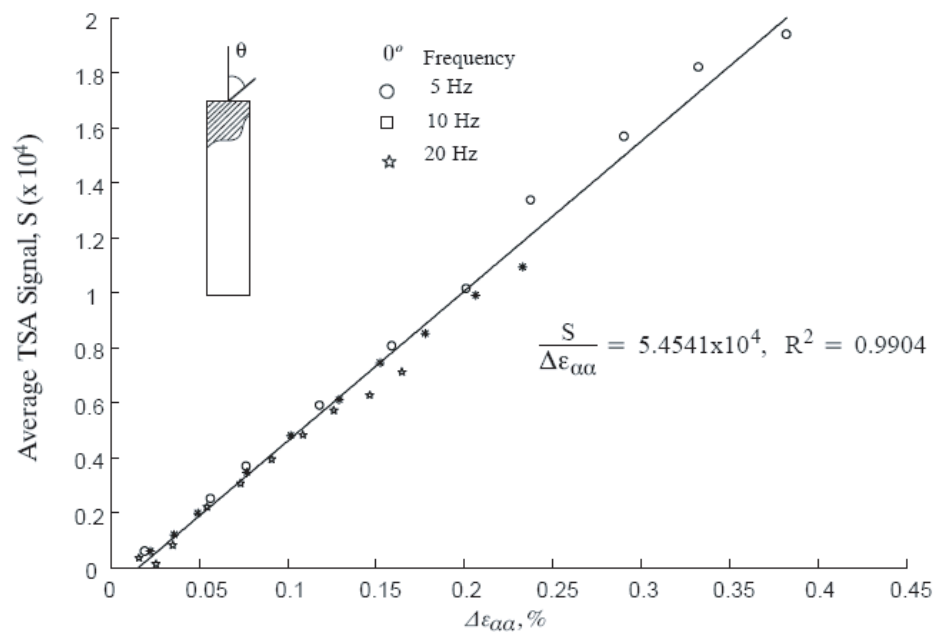


Figure 9: Thermo-mechanical calibration for quasi isotropic S2-glass/Epoxy

2.6 Validation under a Multi-axial state of stress

A standard open-hole specimen ASTM D 5766/ D 5766M was chosen for validation of the calibration under a multi-axial state of stress. The specimen dimensions were 1.5 in wide, with a centered 0.25 in hole, and an ungripped length of 6 in, and a thickness of 0.046 in. The specimen was cut so that the major stiffness axis is the axial direction of the loaded geometry. The specimen was sprayed with flat black paint and the force on the specimen was recorded as the system was cyclically loaded. This change in force was later used in computational models. A quarter symmetry finite element model of the open-hole unidirectional carbon/epoxy system with material properties provided in Table 1 was chosen for computational analysis. The specimen geometry and finite element mesh are shown in Figure 10. The model consisted of 30,000 of Abaqus's CPS8R elements with symmetric boundary conditions on the quarter geometry. A uniformly distributed load (half of that applied to the actual specimen) was applied to the model, and the sum of the in-plane strains along the horizontal and vertical axes through the center of the hole were plotted in Figure 12 through 15 and 17 through 24. The results were used to how the experimental results compared to finite element and to show the effect of adding a surface witness layer.

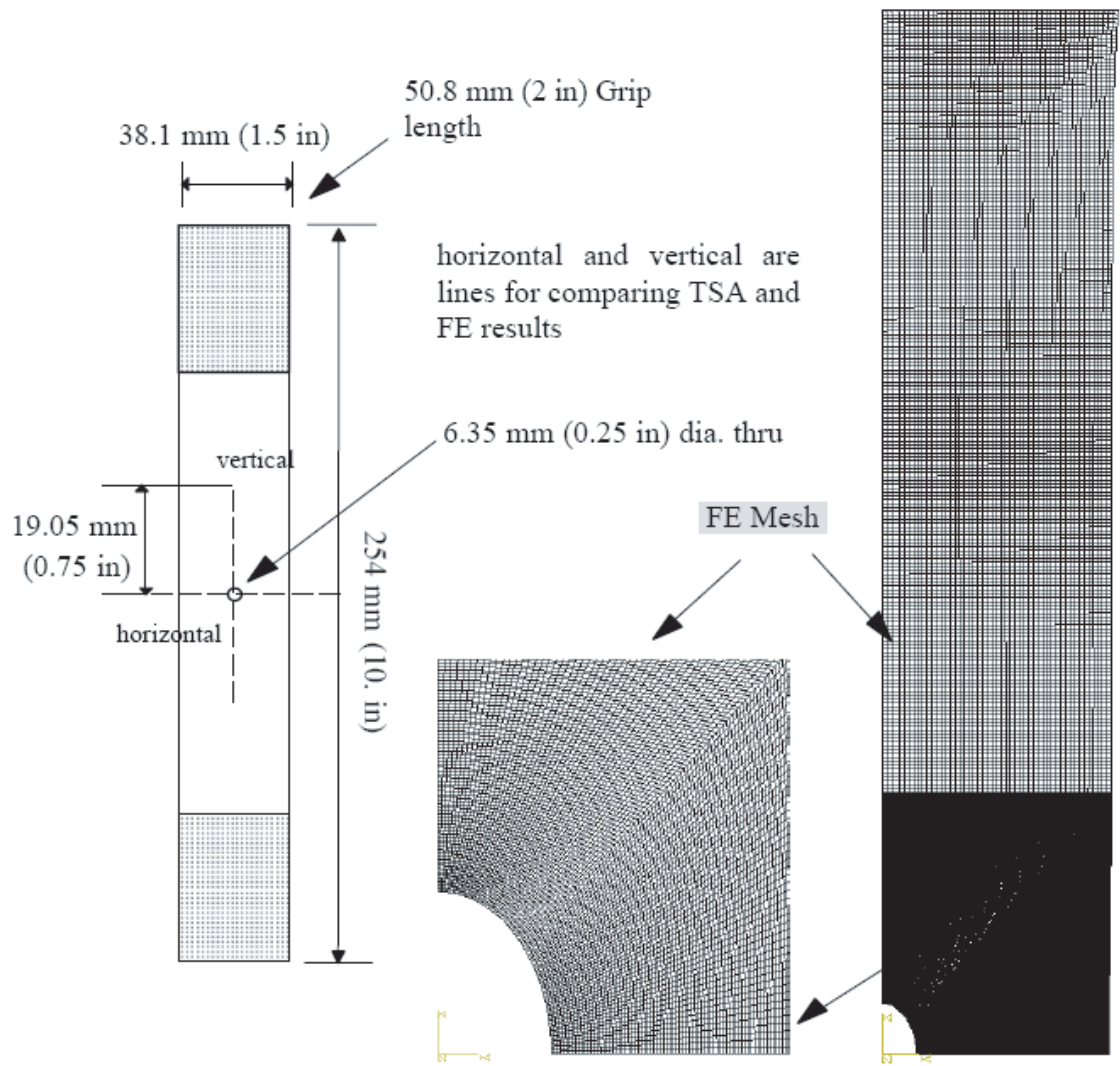


Figure 10: Geometry of notched specimen used to verify the TSA technique and a very refined quarter-model FE mesh used to model the notched specimen

A TSA image of an un-coated unidirectional carbon/epoxy open-hole specimen was taken, and the result is shown in Figure 11. Notice in this case a small amount of damage resulted upon drilling the unidirectional composite, and some loose fibers are seen at the hole edge on the left side of the image of the un-coated specimen in Figure 11. Future open-hole specimens were drilled with a brad point drill bit at a low drill speed (600 rpm) as suggested by Mackin et al. [93].

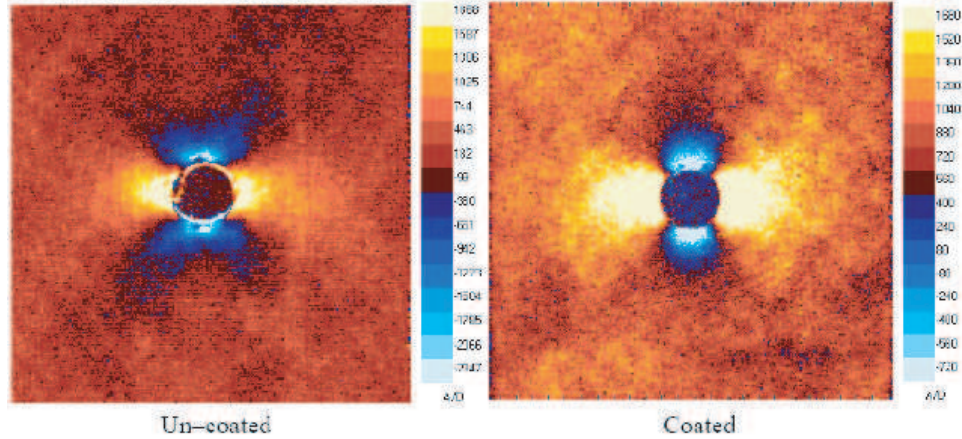


Figure 11: TSA images of open hole specimens of Carbon/epoxy

Figures 12 and 15 show vertical and horizontal line interrogations drawn on the TSA data for a 0 degree specimen through the center of the hole using the 0 degree calibration constant ($k_e = 2.1415 \times 10^4$ as shown in Figure 5) to scale the data. The vertical line interrogation shows thermoelastic data for a 38.1 mm (1.5 in) line through the center of the hole as shown in Figure 10. A reasonable accuracy was achieved for model verification using the 0 degree calibration constant with a 0 degree open hole coupon. To verify the proposed calibration, the surface of the specimen must be coated with epoxy or alternative isotropic coat, and the experimental calibration must be re-examined so that a single calibration constant is achieved. In this case however, the 0 degree calibration constant was used because a small error in $\epsilon_{\alpha\alpha}$ would result from an experimental test where the TSA values are less than 2000 camera units. So within this range of the calibration, a single constant was used to

verify a computational model.

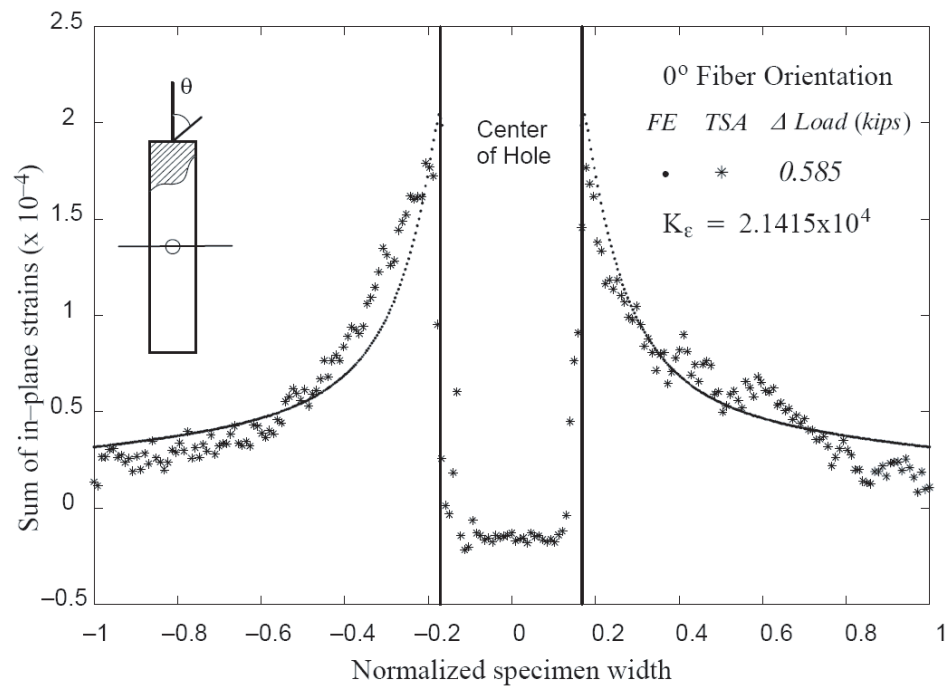


Figure 12: Horizontal line interrogation of open-hole geometry for verification of thermomechanical calibration of un-coated unidirectional carbon/epoxy

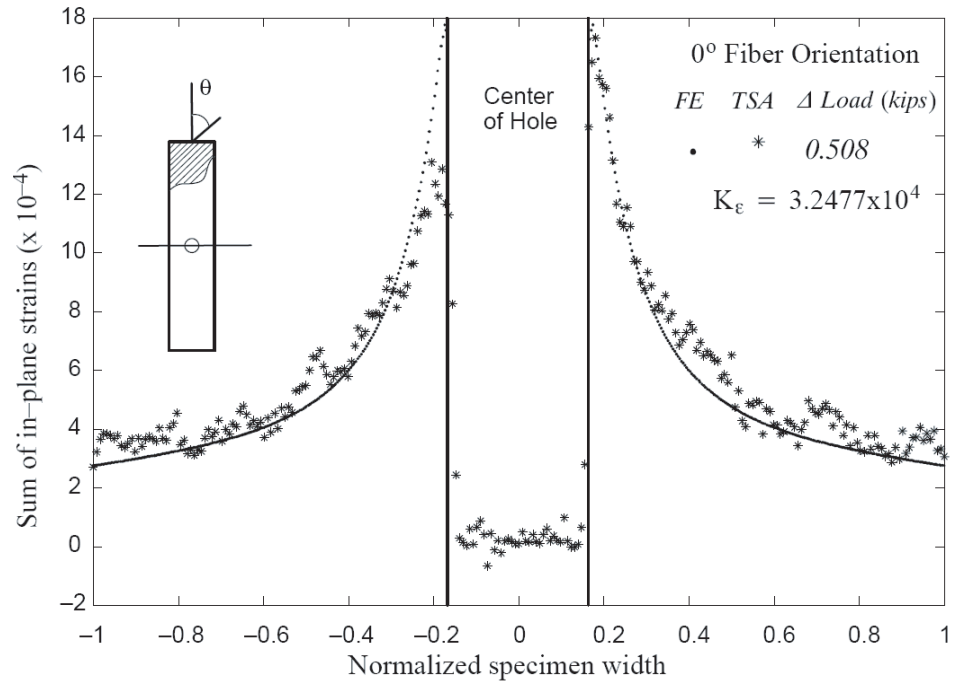


Figure 13: Horizontal line interrogation of open-hole geometry for verification of thermomechanical calibration of coated unidirectional carbon/epoxy

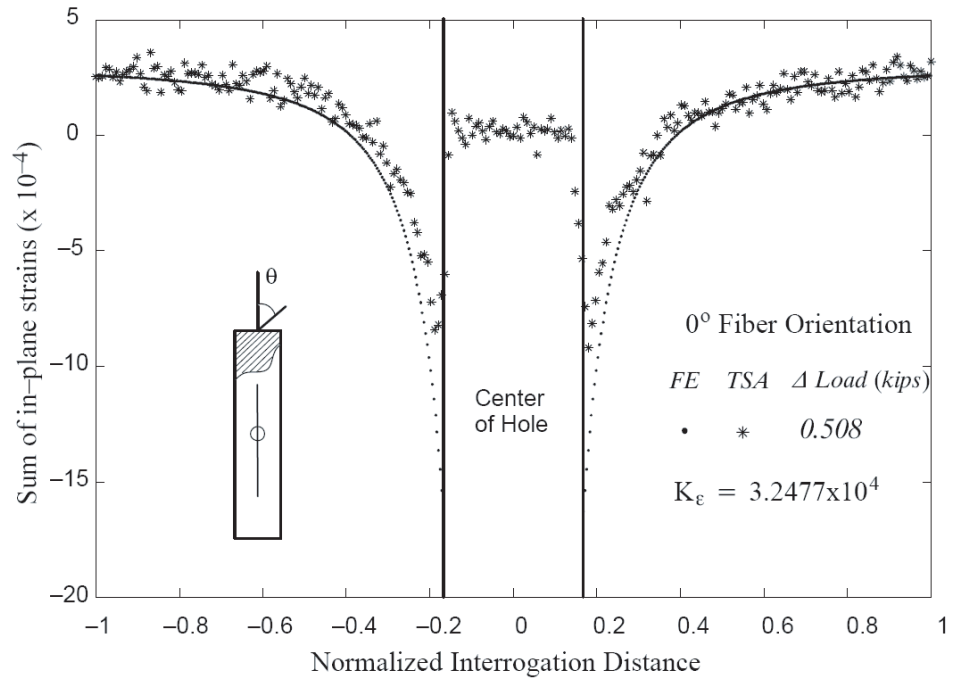


Figure 14: Vertical line interrogation of open-hole geometry for verification of thermomechanical calibration of coated unidirectional carbon/epoxy

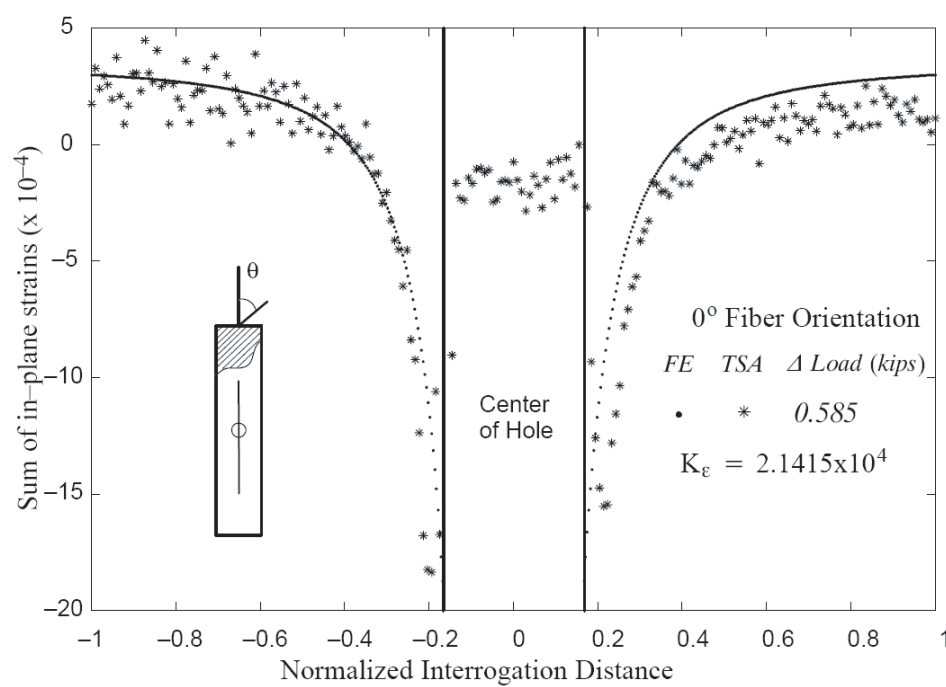


Figure 15: Vertical line interrogation of open-hole geometry for verification of thermomechanical calibration of un-coated unidirectional carbon/epoxy

For validation of the S2-glass/epoxy system the same geometry shown in Figure 10 was chosen for validation of the calibration under a multi-axial state of stress. The major stiffness axis is the axial direction of the loaded geometry. The lay-up of the two S2-glass/epoxy systems are quasi-isotropic and a $[0_5/90/0_5]$ lay-up as shown in Figure 6. In the case of the $[0_5/90/0_5]$ lay-up, one 90° ply is placed in the middle of the lay-up to provide additional stability to the system. A uniform thickness of 0.089 in was achieved for this system using an autoclave. A uniform thickness of 0.0662 in was achieved for the quasi-isotropic system using an autoclave. The specimen was sprayed with flat black paint and the force on the specimen was recorded as the system was cyclically loaded. This change in force was later used in computational models. The same quarter geometry finite element mesh was used for the computational analysis of this system with material properties provided in Table 1.

The computational results for two loading cases with the corresponding experimental loading cases are plotted in Figures 17 and 21 for the $[0_5/90/0_5]$ lay-up. These experiments take into account the thermomechanical constant provided in Figure fig:cals2, $k_\epsilon = 3.8195 \times 10^4$. The full-field infrared signal can be used to verify various specimen geometries and material systems with some accuracy. Notice the uniformity of the TSA signal in Figure 16. Overall, the results illustrate the accuracy of the proposed method in determining the full-field strain invariant in various FRP systems. In both cases only a coating of flat black paint was applied to the specimen surface. Improved results may be obtained by adding a layer of continuous fiber mat material or epoxy to the surface. The 45 layer of S2-glass/epoxy on the surface of the Quasi Isotropic layup shows that the surface ply plays a large role in the thermoelastic response.

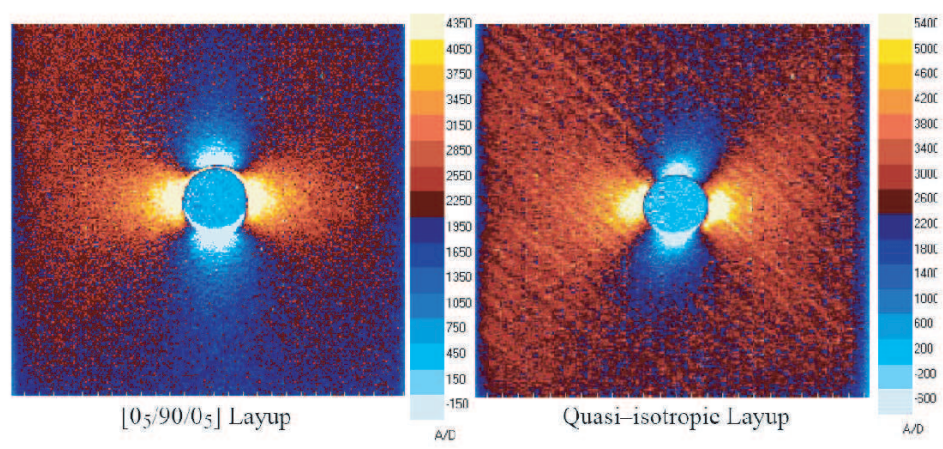


Figure 16: TSA images of open hole specimens of S2-glass/epoxy

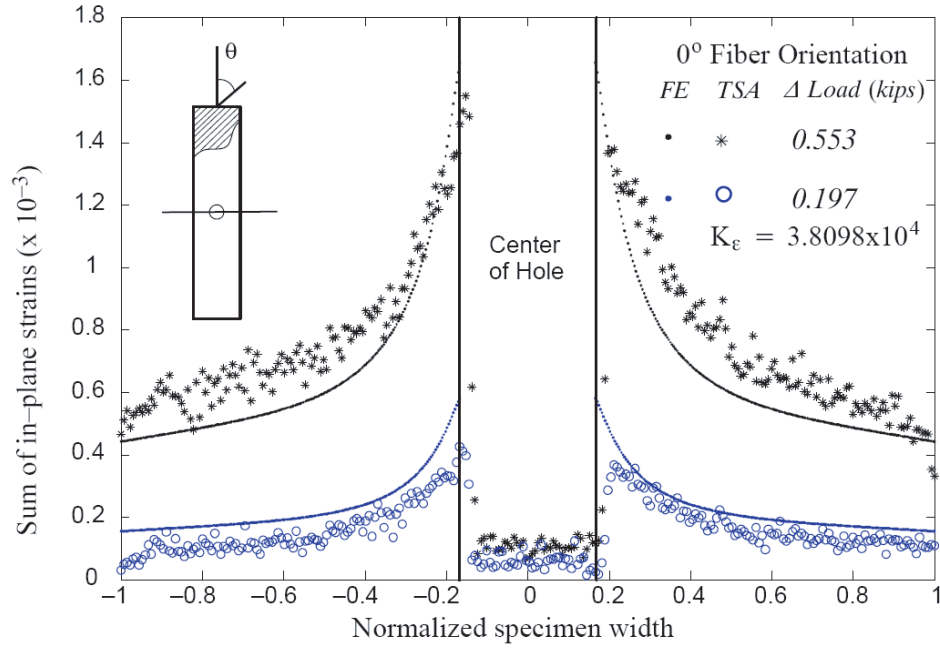


Figure 17: Horizontal line interrogation of open-hole geometry for verification of thermomechanical calibration of un-coated S2-glass/epoxy for the $[0_5/90/0_5]$ lay-up

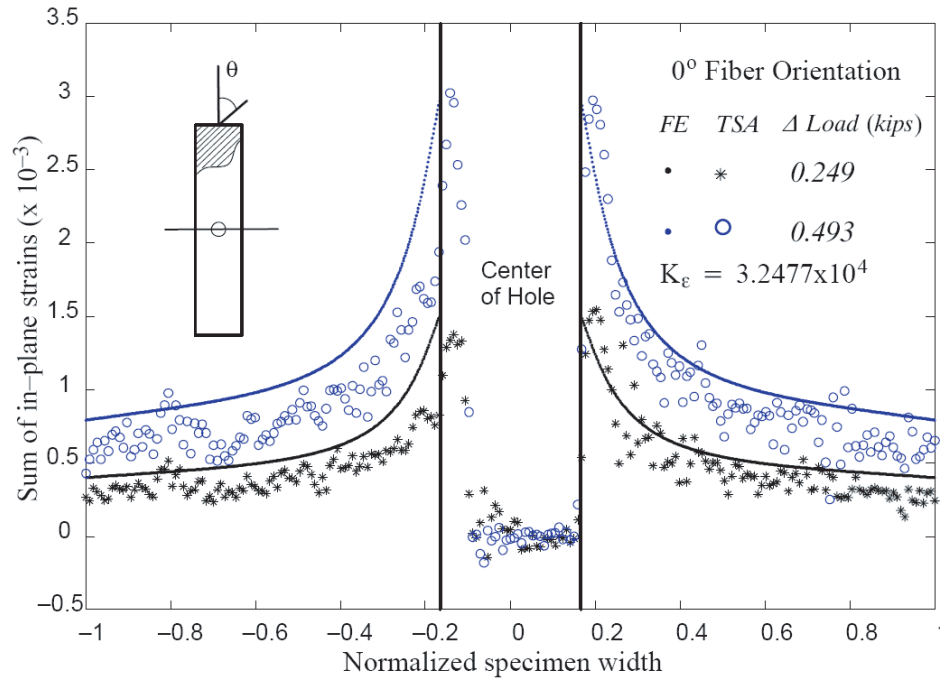


Figure 18: Horizontal line interrogation of open-hole geometry for verification of thermomechanical calibration with epoxy coating of S2-glass/epoxy for the $[0_5/90/0_5]$ lay-up

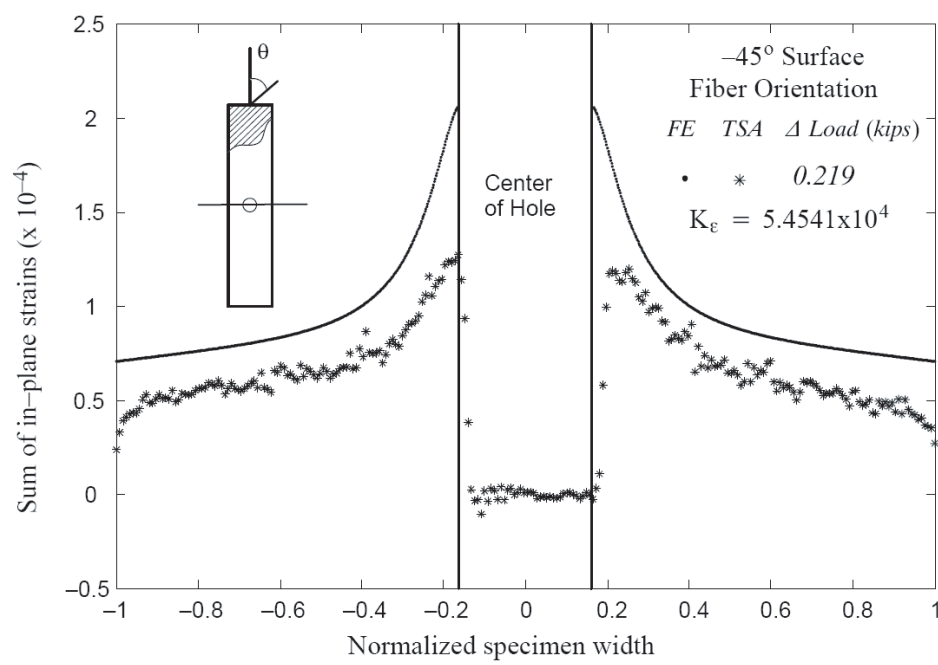


Figure 19: Horizontal line interrogation of open-hole geometry for verification of thermomechanical calibration of un-coated quasi-isotropic S2-glass/epoxy lay-up

The lack of fit for the prediction shown in Figure 19 can be explained due the multi-axial state of stress in the material system of the top layer, i.e. normal and transverse stresses. Previous predictions from this type of calibration were done for the 0° top layer with predominately axial stresses. This may also explain the good quality in those cases.

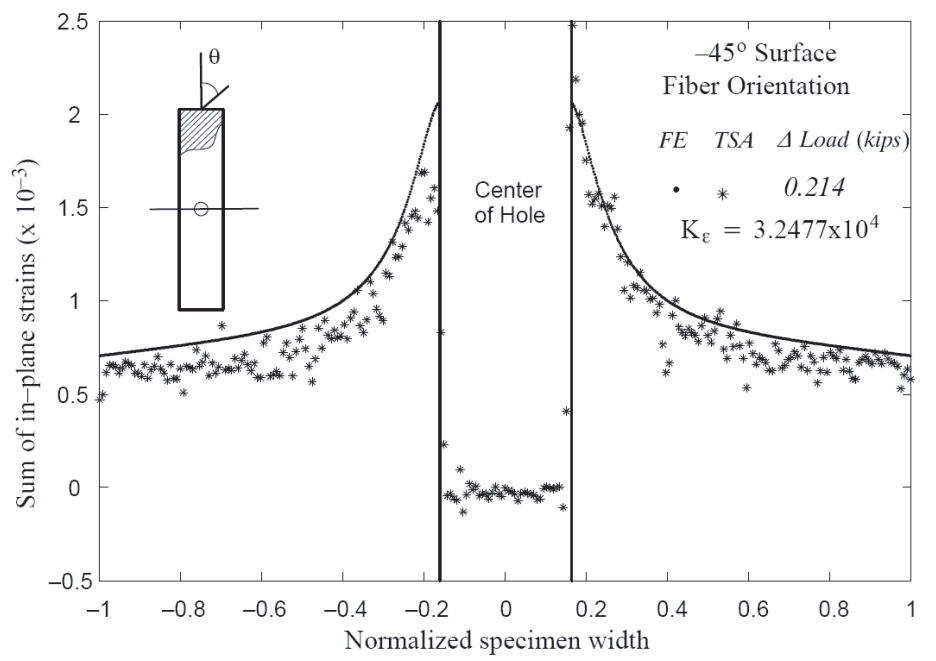


Figure 20: Horizontal line interrogation of open-hole geometry for verification of thermomechanical calibration with epoxy coating of quasi-isotropic S2-glass/epoxy lay-up

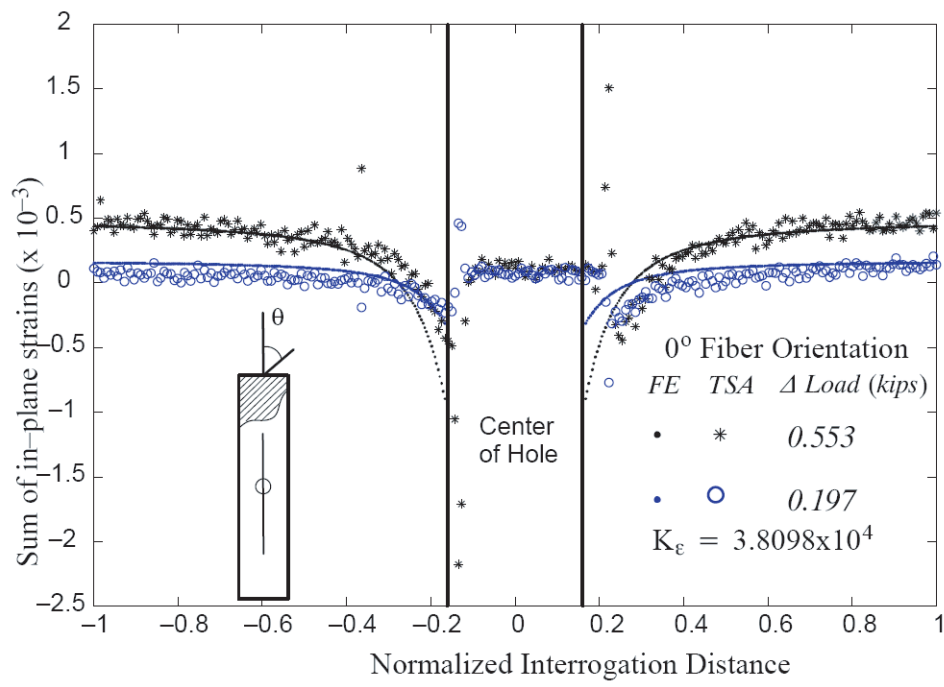


Figure 21: Vertical line interrogation of open-hole geometry for verification of thermomechanical calibration of un-coated S2-glass/epoxy for the $[0_5/90/0_5]$ lay-up

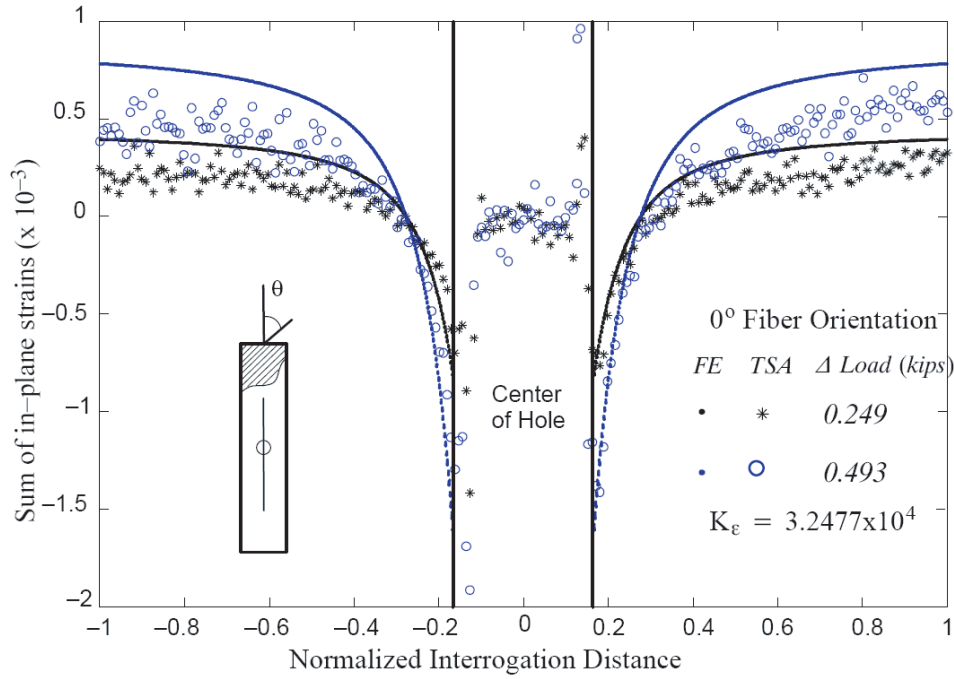


Figure 22: Vertical line interrogation of open-hole geometry for verification of thermomechanical calibration with epoxy coating of the S2-glass/epoxy for the $[0_5/90/0_5]$ lay-up

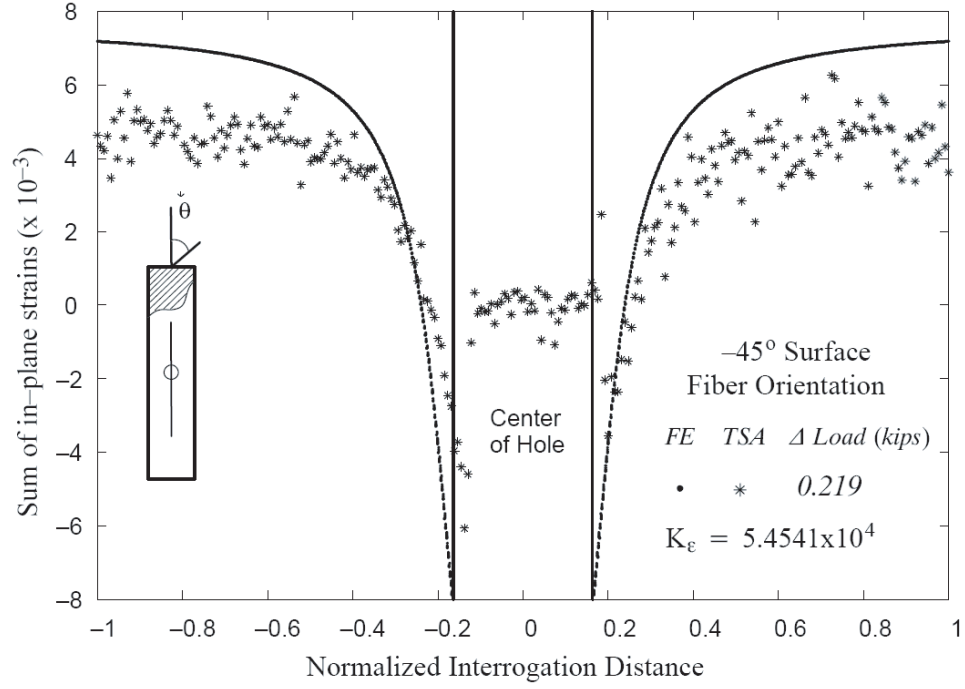


Figure 23: Vertical line interrogation of open-hole geometry for verification of thermomechanical calibration for un-coated S2-glass/epoxy with a quasi-isotropic lay-up

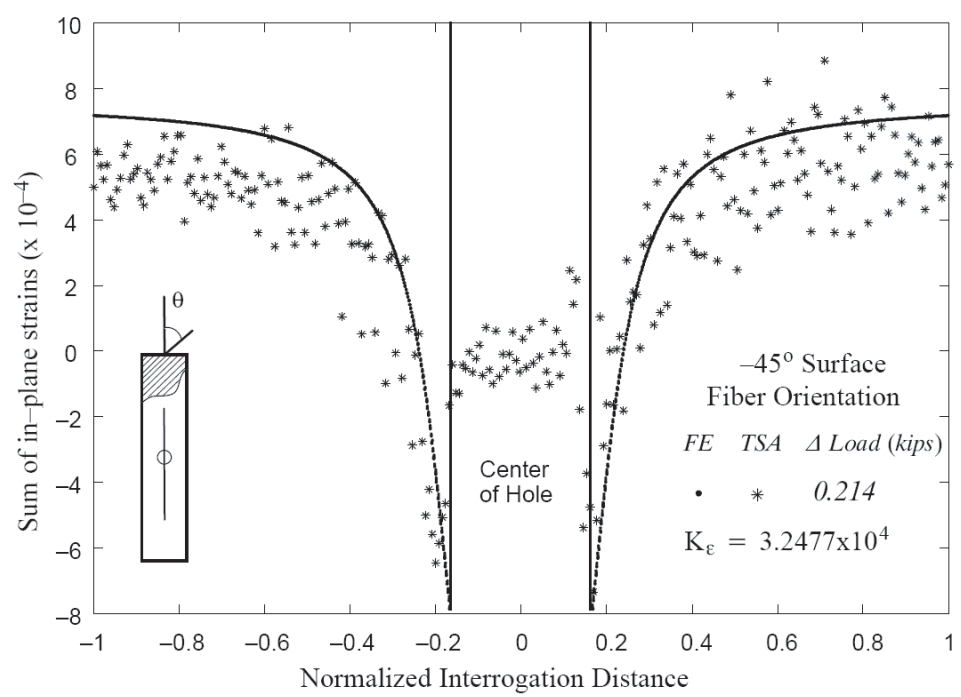


Figure 24: Vertical line interrogation of open-hole geometry for verification of thermomechanical calibration with epoxy coating for S2-glass/epoxy with a quasi-isotropic lay-up

CHAPTER III

MECHANICAL BEHAVIOR OF JUTE HYBRID BIO-COMPOSITES

3.1 Introduction

This chapter utilizes TSA as before, but this section discusses analytical work and towards investigating nonlinear behavior in Jute Hybrid Bio-Composites where TSA techniques are utilized for validation of the computational modeling approaches. An experimental and analytical study is carried out to investigate the mechanical behavior of biocomposites in the form of pultruded layers manufactured with Jute bio-fibers, combined with unidirectional roving E-glass, and embedded in a polymeric matrix. Stress strain curves are generated for these dually reinforced systems in transverse, axial and shear modes to calibrate the nonlinear parameters for computational models. Two macro and one micromechanical constitutive models are proposed to characterize the nonlinear orthotropic behavior of these material systems and implement them within a finite element (FE) code. The models are validated under a multi-axial state of stress by full-field stress/strain analysis via digital image correlation (DIC) and Thermoelastic Stress Analysis (TSA) of open-hole specimens. While these hybrid composites have relatively low modulus, their material consistency lend them to be used in many structural applications. Hybrid bio-composites are environmentally friendly and can provide a sustainable alternative to existing engineering materials in several applications. Section 2 of this manuscript introduces the bio-composites used in this study along with their composition and overall linear mechanical properties. Section 3 of this study formulates three nonlinear constitutive material models that can be used to predict the multi-axial stress-strain behavior of bio-composites. Two

of these nonlinear anisotropic homogeneous models assume that the material is under a state of plane stress. The third is a Nine-Cell nonlinear 3D micromechanical model using a special case of the more general High Fidelity Generalized Method of Cells (HFGMC) proposed by Aboudi [101] and modified by Haj-Ali and Aboudi [58]. The formulation for the HFGMC model is also given in this section. The models from Section 3 are calibrated and validated in the third part of this study with Thermoelastic Stress Analysis (TSA) and Digital Image Correlation (DIC) for a full-field stress-strain analysis of plates with a hole. A more detailed description of techniques used for validation of computational analysis using TSA is available in the literature on static, fatigue, and fracture behavior of FRP composite materials for quantitative comparisons in the Introduction.

3.2 Jute Hybrid Bio-composite Systems

The hybrid composite system for this study is composed of continuous Jute yarns running the length of a flat pultruded plate sandwiched between glass chopstrand mat surface layers. The glass mat reinforcement provides some transverse reinforcement. The averaged properties of the material system used in this study are shown in Table 2.

Table 2: Description of Jute hybrid bio-composite material system

Material Constituent	Volume Fraction
Jute Yarn	0.360
E-Glass Chopstrand Mat	0.1325
Matrix	0.5075

To get an estimate of the fiber volume fractions, photo microscopy was used to measure the cross-sectional areas of the Jute fibers and chopstrand glass mat layers. Notice in Figure 25 that the Jute fibers are a woven bundle—a non-circular shape.

The Jute fibers are visibly darker than the surrounding matrix and the chopstrand mat glass layers, so this fact is used to apply image analysis algorithms to segment

the fibers from the matrix. In Figure 26, the first steps are taken to create a binary image where segmented areas can be measured.

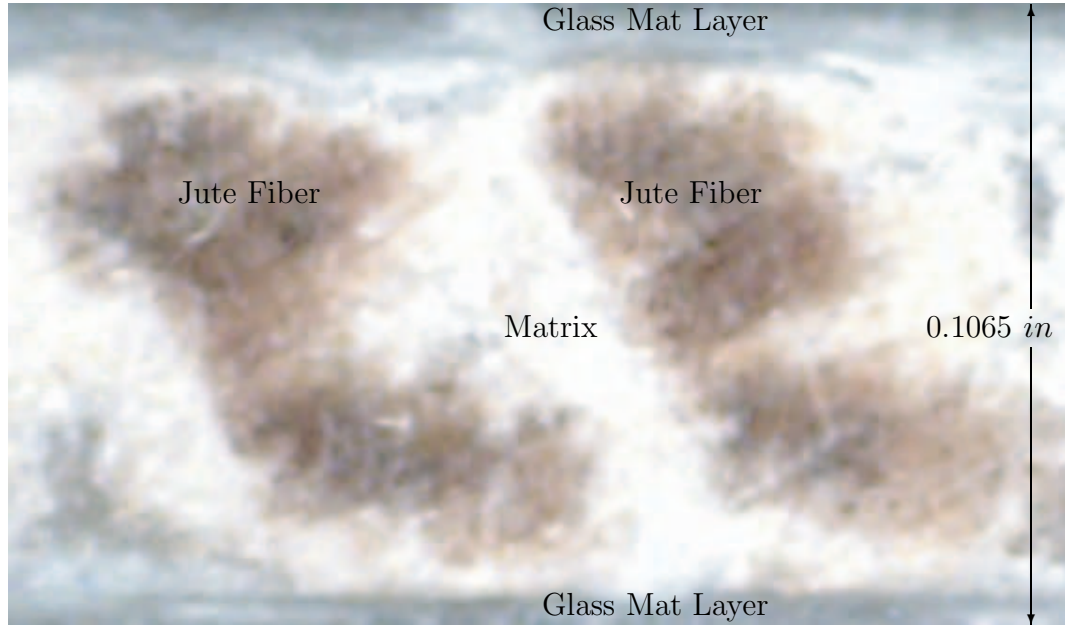


Figure 25: Hybrid Jute/Glass composite with chopstrand mat surface layer



Figure 26: Color similarity algorithms used to identify and segment Jute yarns from background

3.3 Nonlinear Constitutive Models for Bio-Composites

Many experimental and analytical studies have been focused on the nonlinear response of laminated composite materials. Macro-level theories are formulated to characterize the nonlinear response by idealizing the composite as an anisotropic homogeneous medium. Petit [102] proposed an incremental approach for the analysis of symmetric laminates under uniform membrane loading. In their approach, the elastic constants of a lamina are determined as a function of the lamina strains. A lamina failure is identified when any of its strain components exceeds the experimentally obtained limiting strain value. Once a failure mode is detected in the lamina, the corresponding tangent stiffness is set to a high negative value in order to achieve stress unloading in this direction. Their analyses predicted the overall shape of the nonlinear response quite well, while the laminate ultimate failure loads were predicted with acceptable accuracy. Hahn and Tsai [55] used the complementary energy density polynomial function, for a lamina under a plane-stress state, to derive a nonlinear stress-strain relation for laminated composites. An additional fourth-order term of the axial-shear stress is added to the polynomial function. This term represents the nonlinear shear strain. Interaction terms between the three stress components were neglected. Hahn [54] extended this work to model the nonlinear behavior of laminates, and considered the effect of material nonlinearity on the buckling load of a symmetric laminate. Hashin et al. [67] formulated a new nonlinear constitutive model where inelastic transverse and axial shear strains exist in a lamina under plane stress conditions. Each inelastic strain component is an independent quadratic function in terms of the stress invariants raised to a general power. Ramberg-Osgood representation of nonlinear stress-strain curves was used to express the nonlinear axial-shear and transverse stress-strain relations. Predicted nonlinear behavior compared well with experimental results for different laminated composite materials. Jones and

Nelson [77] proposed a material model based on strain energy that accounts for nonlinear behavior under biaxial states of stress. This model can only be applied to multi-axial stress states where the strain energy is lower than the maximum strain energy generated in the uni-axial test results. Since this is often the case when the composite is subject to general multi-axial stress states, different approaches were proposed to overcome this difficulty, Jones and Morgan [76], Abu-Farsakh [7]. Amijima and Adachi [10] introduced a simple technique to represent the shear nonlinearity using piecewise linear segments. Sandhu [112] introduced a technique for solution of the nonlinear laminate equations using piecewise cubic spline functions to represent the lamina uni-axial test data. He also proposed a predictor-corrector iterative method. Nahas [99] presented a similar predictor-corrector technique in which the basic uni-axial stress-strain relations are allowed to have a general nonlinear representation. Kuppuswamy et al. [86] used the Richard and Abbott [106] representation for the nonlinear uni-axial stress-strain relations in a three-dimensional finite element analysis. However, their study uses uncoupled one-dimensional stress-strain relations which do not reflect interaction effects. Pindera and Herakovich [103] and Mathison et al. [96] derived a nonlinear plane stress constitutive model using orthotropic endochronic theory. This theory is based on irreversible thermodynamics with internal variables. Dvorak and Rao [45] proposed a plasticity theory for fibrous composites under axisymmetric deformation. Plastic dilatation and deformation of the composite in the fiber direction were accounted for. A yield function was formed using the stress invariants of a transversely isotropic material and simple hardening and flow rules were derived. Griffin [53] extended Hill's anisotropic plasticity theory, and used the associated plasticity flow rule to determine the plastic increment of strain. A Ramberg-Osgood uni-axial stress-strain relation was used to model nonlinear hardening. Sun and Chen [119] developed a one parameter orthotropic plasticity model for thermoplastic and metal-matrix composite laminates in plane stress. In this model,

one-parameter plastic-potential scalar function is proposed. Only transverse and axial shear stresses are involved in the plastic potential; therefore, plastic deformation in the axial direction of the lamina is neglected. In addition, a power law relation between effective plastic strain and the effective stress is proposed; as a result, a total of three material parameters are needed to fully describe the lamina plastic behavior. Sections 3.1 and 3.2 of this manuscript describe the formulations for nonlinear orthotropic macromechanical models used for bio-composites. Section 3.3 of this manuscript describes the formulation of a multiphase micromechanical constitutive model used for capturing nonlinear anisotropic behavior in bio-composites. Section 4. presents experimental calibration and validation of the models implemented within ABAQUS [2] finite element program as formulated in Section 3.

3.3.1 Anisotropic Deformation Theory (ADT) Based Model

The ADT model presented here is similar to Hashin's [67] anisotropic deformation theory with the addition of inelastic behavior for the σ_{11} stress in the fiber direction.

Decompose the strain into elastic and inelastic parts:

$$\epsilon_{ij} = \epsilon_{ij}^e + \epsilon_{ij}^I \quad (25)$$

Similar to the isotropic case: $\epsilon_{ij}^I = f(J_2)S_{ij}$ We assume:

$$\epsilon_{ij}^I = f(L)\sigma_{ij} \quad (26)$$

$$L = \alpha_{11}^2\sigma_{11}^2 + \alpha_{22}^2\sigma_{22}^2 + \alpha_{66}^2\sigma_{66}^2 \quad (27)$$

$$(28)$$

One dimensional Ramberg Osgood relations in the 22 direction:

$$\epsilon_{22} = \frac{1}{E_{22}}\sigma_{22} + \beta_2 \left(\frac{|\sigma_2|}{\sigma_{02}} \right)^{n_2-1} \sigma_2 \quad (29)$$

$$\epsilon_{22}^I = \beta_2 \left(\frac{|\sigma_2|}{\sigma_{02}} \right)^{n_2-1} \sigma_{22} = \beta_2 \left[\left(\frac{|\sigma_2|}{\sigma_{02}} \right)^2 \right]^{\frac{n_2-1}{2}} \sigma_{22} \quad (30)$$

taking the general form: $\epsilon_{22}^I = f_{22}(L)\sigma_{22}$ then,

$$f_{22}(L) = f_{22}(\alpha_{22}^2 \sigma_{22}^2) = \beta_2 \left[\left(\frac{|\sigma_{22}|}{\sigma_{02}} \right)^2 \right]^{\frac{n_2-1}{2}} \quad (31)$$

and α can be defined as:

$$\alpha_{22}^2 = \sigma_{02}^{-2}; f_{22} = \beta_2 L^{\frac{n_2-1}{2}} \quad (32)$$

$$\alpha_{11}^2 = \sigma_{01}^{-2}; f_{11} = \beta_1 L^{\frac{n_1-1}{2}} \quad (33)$$

$$\alpha_{66}^2 = \sigma_{06}^{-2}; f_{66} = \beta_6 L^{\frac{n_6-1}{2}} \quad (34)$$

Therefore:

$$\epsilon_{11} = \frac{1}{E_{11}}\sigma_{11} - \frac{\nu_{12}}{E_{11}}\sigma_{22} + \beta_1 L^{\frac{n_1-1}{2}}\sigma_{11} \quad (35)$$

$$\epsilon_{22} = -\frac{\nu_{12}}{E_{11}}\sigma_{11} + \frac{1}{E_{22}}\sigma_{22} + \beta_2 L^{\frac{n_1-1}{2}}\sigma_{22} \quad (36)$$

$$\gamma_{12} = \frac{1}{G_{12}}\sigma_{12} + \beta_6 L^{\frac{n_6-1}{2}}\sigma_{12} \quad (37)$$

If the Ramberg Osgood form is:

$$\epsilon = \frac{1}{E}\sigma + \frac{\beta\sigma_o}{E} \left(\frac{\sigma}{\sigma_o} \right)^n \quad (38)$$

$$\epsilon_{22}^I = \frac{\beta_2\sigma_{02}}{E_{22}} \left(\frac{\sigma_{22}}{\sigma_{02}} \right)^{n_2} = \frac{\beta_2}{E_{22}} \left[\left(\frac{|\sigma_{22}|}{\sigma_{02}} \right)^2 \right]^{\frac{n_2-1}{2}} \sigma_{22} \quad (39)$$

$$\epsilon_{22}^I = \frac{1}{E_{22}} f_{22}(L) \sigma_{22} \quad (40)$$

$$f_{22}(L) = f_{22}(\alpha_{22}^2 \sigma_{22}^2) = \beta_2 \left[\left(\frac{|\sigma_{22}|}{\sigma_{02}} \right)^2 \right]^{\frac{n_2-1}{2}} \quad (41)$$

Therefore:

$$\epsilon_{11} = \frac{1}{E_{11}}\sigma_{11} - \frac{\nu_{12}}{E_{11}}\sigma_{22} + \frac{\beta_1}{E_{11}} L^{\frac{n_1-1}{2}}\sigma_{11} \quad (42)$$

$$\epsilon_{22} = -\frac{\nu_{12}}{E_{11}}\sigma_{11} + \frac{1}{E_{22}}\sigma_{22} + \frac{\beta_2}{E_{22}} L^{\frac{n_1-1}{2}}\sigma_{22} \quad (43)$$

$$\gamma_{12} = \frac{1}{G_{12}}\sigma_{12} + \frac{\beta_6}{G_{12}} L^{\frac{n_6-1}{2}}\sigma_{12} \quad (44)$$

Recall:

$$L = \left(\frac{\sigma_{11}}{\sigma_{01}} \right)^2 + \left(\frac{\sigma_{22}}{\sigma_{02}} \right)^2 + \left(\frac{\sigma_{12}}{\sigma_{06}} \right)^2 \quad (45)$$

$$\frac{\partial \epsilon_{11}}{\partial \sigma_1} = \frac{1}{E_{11}} + \frac{\beta_1}{E_{11}} L^{\frac{n_1-1}{2}} + \frac{\beta_1}{E_{11}} \left(\frac{n_1-1}{2} \right) L^{\frac{n_1-3}{2}} \frac{\partial L}{\partial \sigma_{11}} \sigma_1 \quad (46)$$

$$\frac{\partial \epsilon_{11}}{\partial \sigma_2} = \frac{-\nu_{12}}{E_{11}} + \frac{\beta_1}{E_{11}} \frac{n_1-1}{2} L^{\frac{n_1-3}{2}} \frac{\partial L}{\partial \sigma_{22}} \sigma_1 \quad (47)$$

$$\frac{\partial \epsilon_{11}}{\partial \sigma_{12}} = \frac{\beta_1}{E_{11}} \frac{n_1-1}{2} L^{\frac{n_1-3}{2}} \frac{\partial L}{\partial \sigma_{12}} \sigma_1 \quad (48)$$

$$\frac{\partial L}{\partial \sigma_{11}} = \frac{2\sigma_{11}}{\sigma_{01}^2}; \frac{\partial L}{\partial \sigma_{22}} = \frac{2\sigma_{22}}{\sigma_{02}^2}; \frac{\partial L}{\partial \sigma_{12}} = \frac{2\sigma_{12}}{\sigma_{06}^2} \quad (49)$$

The tangent stiffness is therefore:

$$\frac{d\epsilon_{22}}{d\sigma_{11}} = \frac{-\nu_{12}}{E_{11}} + \frac{\beta_2}{E_{22}} \frac{n_2-1}{2} L^{\frac{n_2-3}{2}} \frac{\partial L}{\partial \sigma_1} \sigma_2 \quad (50)$$

$$\frac{d\epsilon_{22}}{d\sigma_{22}} = \frac{1}{E_{22}} + \frac{\beta_2}{E_{22}} L^{\frac{n_2-1}{2}} + \frac{\beta_2}{E_{22}} \left(\frac{n_2-1}{2} \right) L^{\frac{n_2-3}{2}} \frac{\partial L}{\partial \sigma_2} \sigma_2 \quad (51)$$

$$\frac{d\epsilon_{22}}{d\sigma_{12}} = \frac{\beta_2}{E_{22}} \left(\frac{n_2-1}{2} \right) L^{\frac{n_2-3}{2}} \frac{\partial L}{\partial \sigma_{12}} \sigma_2 \quad (52)$$

$$\frac{d\gamma_{12}}{d\sigma_1} = \frac{\beta_6}{G_{12}} \left(\frac{n_6-1}{2} \right) L^{\frac{n_6-3}{2}} \frac{\partial L}{\partial \sigma_1} \sigma_6 \quad (53)$$

$$\frac{d\gamma_{12}}{d\sigma_2} = \frac{\beta_6}{G_{12}} \left(\frac{n_6-1}{2} \right) L^{\frac{n_6-3}{2}} \frac{\partial L}{\partial \sigma_{22}} \sigma_6 \quad (54)$$

$$\frac{d\gamma_{12}}{d\sigma_6} = \frac{1}{G_{12}} + \frac{\beta_6}{G_{12}} L^{\frac{n_6-1}{2}} + \frac{\beta_6}{G_{12}} \left(\frac{n_6-1}{2} \right) L^{\frac{n_6-3}{2}} \frac{\partial L}{\partial \sigma_{12}} \sigma_{12} \quad (55)$$

3.3.2 Anisotropic Potential Theory Model (APT)

The APT model is an energy based nonlinear orthotropic model similar to Hahn-Tsai's [55] nonlinear orthotropic plane stress model with the addition of inelastic terms in the transverse and axial directions.

The energy function can be defined as:

$$\mathbf{W} = \mathbf{W}(\sigma_{11}, \sigma_{22}, \sigma_{12}) = \mathbf{W}(\sigma_1, \sigma_2, \sigma_6) \quad (56)$$

The linear stress vs. strain relations take the form:

$$\epsilon_{11} = \frac{1}{E_{11}}\sigma_{11} - \frac{\nu_{12}}{E_{11}}\sigma_{22} \quad (57)$$

$$\epsilon_{22} = \frac{-\nu_{12}}{E_{22}}\sigma_{11} - \frac{1}{E_{22}}\sigma_{22} \quad (58)$$

$$\gamma_{12} = \frac{1}{G_{12}}\sigma_{12} \quad (59)$$

The complementary energy function, \mathbf{W}^σ , is the sum of the linear and nonlinear cases.

\mathbf{W} is the strain energy density.

$$\mathbf{W}^\sigma = \mathbf{W}^l + \mathbf{W}^{nl} \quad (60)$$

$$\mathbf{W} = \frac{1}{2}\sigma_{ij}\epsilon_{ij} \quad (61)$$

Expanding on the strain energy density from index format:

$$2\mathbf{W}^l = \sigma_{11}\epsilon_{11} + \sigma_{22}\epsilon_{22} + 2\sigma_{12}\epsilon_{12} = \sigma_{11}\epsilon_{11} + \sigma_{22}\epsilon_{22} + \sigma_{12}\gamma_{12} \quad (62)$$

$$2\mathbf{W}^l = \frac{1}{E_{11}}\sigma_{11}^2 - \frac{\nu_{12}}{E_{11}}\sigma_{11}\sigma_{22} - \frac{\nu_{12}}{E_{11}}\sigma_{11}\sigma_{22} + \frac{1}{E_{22}}\sigma_{22}^2 + \frac{1}{G_{12}}\sigma_{12}^2 \quad (63)$$

$$2\mathbf{W}^l = \frac{1}{E_{11}}\sigma_{11}^2 - \frac{2\nu_{12}}{E_{11}}\sigma_{11}\sigma_{22} + \frac{1}{E_{22}}\sigma_{22}^2 + \frac{1}{G_{12}}\sigma_{12}^2 \quad (64)$$

$$2\mathbf{W}_\sigma^{nl} = F_1(\sigma_{11}) + F_2(\sigma_{22}) + F_6(\sigma_6) \quad (65)$$

To account for nonlinearity the 1D Ramberg-Osgood form is implemented in this model.

$$\epsilon = \frac{1}{E}\sigma + \beta \left(\frac{|\sigma|}{\sigma_o} \right)^{\eta-1} \sigma \quad (66)$$

$$\frac{\partial \epsilon}{\partial \sigma} = \frac{1}{E} + \beta \eta \left(\frac{|\sigma|}{\sigma_o} \right)^{\eta-1} \quad (67)$$

The total strain is then the sum of the linear and non-linear parts:

$$\epsilon_{11} = \frac{1}{E_{11}}\sigma_{11} - \frac{\nu_{12}}{E_{11}}\sigma_{22} + \beta_1 \left(\frac{|\sigma_{11}|}{\sigma_{o1}} \right)^{\eta_1-1} \sigma_{11} \quad (68)$$

$$\epsilon_{22} = -\frac{\nu_{12}}{E_{11}}\sigma_{11} + \frac{1}{E_{22}}\sigma_{22} + \beta_2 \left(\frac{|\sigma_{22}|}{\sigma_{o2}} \right)^{\eta_2-1} \sigma_{22} \quad (69)$$

$$\gamma_{12} = \frac{1}{G_{12}}\sigma_{12} + \beta_6 \left(\frac{|\sigma_{12}|}{\sigma_{o6}} \right)^{\eta_6-1} \sigma_{12} \quad (70)$$

Iterative Implementations with Residual Given: $(\epsilon_{11}, \epsilon_{22}, \gamma_{12})$ find $(\sigma_1, \sigma_2, \sigma_6)$

$$\mathbf{R}_1 = \frac{1}{E_{11}}\sigma_{11} - \frac{\nu_{12}}{E_{11}}\sigma_{22} + \beta_1 \left(\frac{|\sigma_{11}|}{\sigma_{o1}} \right)^{\eta_1-1} \sigma_{11} - \epsilon_{11} = 0 \quad (71)$$

$$\mathbf{R}_2 = -\frac{\nu_{12}}{E_{11}}\sigma_{11} + \frac{1}{E_{22}}\sigma_{22} + \beta_2 \left(\frac{|\sigma_{22}|}{\sigma_{o2}} \right)^{\eta_2-1} \sigma_{22} - \epsilon_{22} = 0 \quad (72)$$

$$\mathbf{R}_3 = \frac{1}{G_{12}}\sigma_{12} + \beta_6 \left(\frac{|\sigma_{12}|}{\sigma_{o6}} \right)^{\eta_6-1} \sigma_{12} - \gamma_{12} = 0 \quad (73)$$

$$C_T \equiv \left[\frac{\partial R}{\partial \sigma} \right]^{-1} \quad (74)$$

$$C_T = \begin{bmatrix} \frac{1}{E_{11}} + \beta_1 \eta_1 \left(\frac{|\sigma_{11}|}{\sigma_{o1}} \right)^{\eta_1-1} & \frac{-\nu_{12}}{E_{11}} & 0 \\ \frac{-\nu_{12}}{E_{11}} & \frac{1}{E_{22}} + \beta_2 \eta_2 \left(\frac{|\sigma_{22}|}{\sigma_{o2}} \right)^{\eta_2-1} & 0 \\ 0 & 0 & \frac{1}{G_{12}} + \beta_6 \eta_6 \left(\frac{|\sigma_{12}|}{\sigma_{o6}} \right)^{\eta_6-1} \end{bmatrix}^{-1} \quad (75)$$

Using taylor expansion:

$$R(\sigma) = R(\sigma_1, \sigma_2, \sigma_6) = 0 \quad (76)$$

$$R(\sigma) \cong R(\sigma^{(i)}) + \left[\frac{\partial R}{\partial \sigma} \right] \bigg|_{\sigma^{(i)}} (\sigma^{(i+1)} - \sigma^{(i)}) = 0 \quad (77)$$

$$\Delta \sigma \equiv (\sigma^{(i+1)} - \sigma^{(i)}) = - \left[\frac{\partial R}{\partial \sigma} \right]^{-1} \bigg|_{\sigma^{(i)}} \{ R(\sigma^{(i)}) \} \quad (78)$$

$$\Delta \sigma = -C_T \bigg|_{\sigma^{(i)}} R(\sigma^{(i)}) \quad (79)$$

In general:

$$\epsilon_{11} = \left[\frac{1}{E_{11}} + f_1(\sigma_{11}) \right] \sigma_{11} - \left[\frac{\nu_{12}}{E_{11}} + f_{21}(\sigma_{22}) \right] \sigma_{22} \quad (80)$$

$$\epsilon_{22} = - \left[\frac{\nu_{12}}{E_{11}} + f_{12}(\sigma_{11}) \right] \sigma_{11} + \left[\frac{1}{E_{22}} + f_2(\sigma_{22}) \right] \sigma_{22} \quad (81)$$

$$\gamma_{12} = \left[\frac{1}{G_{12}} + f_6(\sigma_6) \right] \sigma_6 \quad (82)$$

Note that assuming $f_{12} = f_{21} = 0$ implies no nonlinear poisson's effects.

3.3.3 New Formulation for the Nine-Cell Micromechanical Model (Nine-Cell)

The newly developed micromechanical model for the lamina is shown in Figure 27. Previous implementations include a two, four, and multi-cell models developed by Haj-Ali et al. [56, 57, 59–61, 81] for nonlinear analysis of E-glass/vinylester pultruded composites validated under different multi-axial states of stress with and without damage under tension, compression, bending and off-axis. In the Nine-Cell model a unidirectional lamina is represented by a 3-by-3 matrix of constituents with rectangular cross-sections representing the binder and long fibers which account for the 3D mechanical response. The nine cells (subcells) within the Unit Cell (UC) are given properties of the Jute fiber, glass chopstrand mat, and matrix constituents. The micromechanical framework allows a description of the subcells and material constituents that can be used to account for damage mechanisms and overall nonlinear and damage softening behavior. The mechanical response of the UC is determined by satisfying the traction continuity and strain compatibility constraints between the subcells.

The Nine-Cell model is similar to the is a simplified version of the more general case of the High Fidelity Generalized Method of Cells given by Haj-Ali [58], and the derivation here includes the incremental formulation with integration and correction schemes as described in Haj-Ali [56].

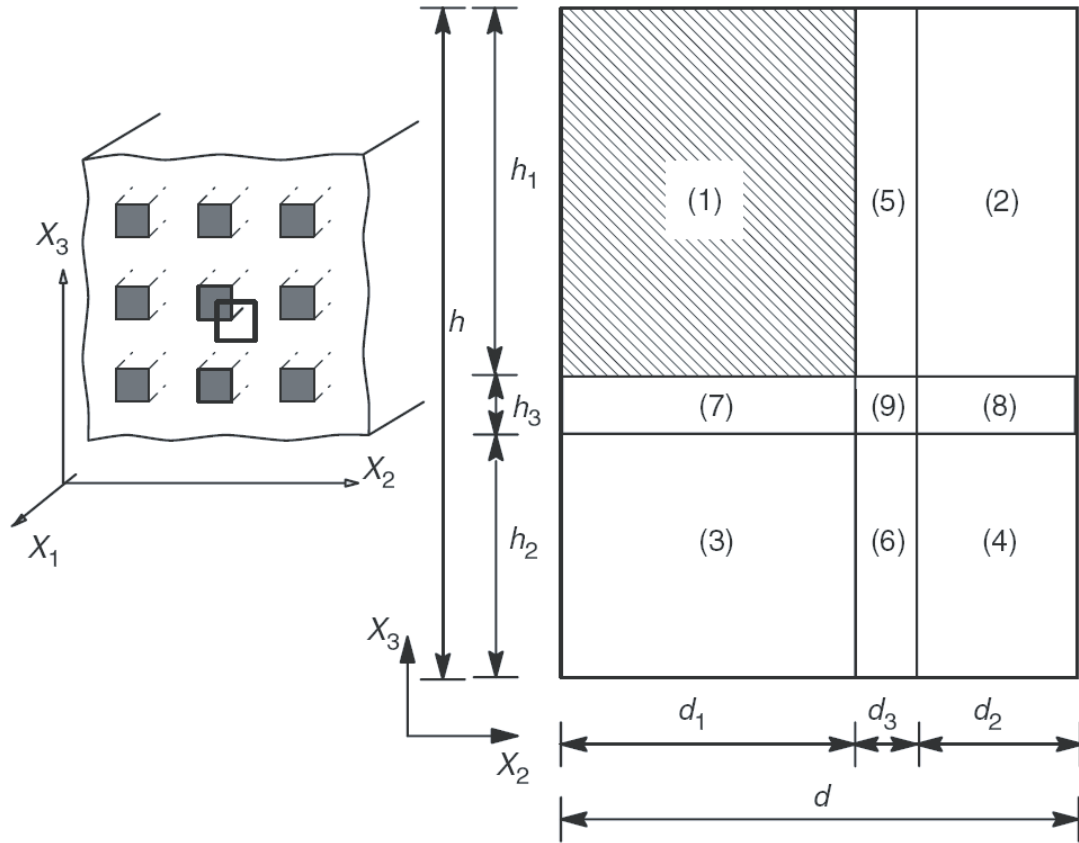


Figure 27: (a) Idealized medium with periodic arrays of long fibers (rectangular cross-sections) showing a quarter UC (bold line), (b) Nine-cell micromodel of rectangular UC

The unidirectional composite shown in Figure 27 consists of long fibers embedded in the matrix system. It is idealized as doubly periodic array of fibers with rectangular cross section. Taking into account symmetry, a quarter UC is used here that consists of nine subcells is used in the formulation. Instead of assigning interface subcells as discussed in [56], all of the cells are used to capture the nonlinear behavior without damage. The first subcell is a fiber constituent, while subcells 2, 3, and 4 represent the matrix constituents. The other subcells, 5–9, represent the interfaces. The long fibers are aligned in the x_1 direction. The other cross-section directions are referred to as the transverse directions. The x_3 direction is called the out-of-plane axis or lamina thickness direction. The nine-cell micromodel is formulated by describing the relations between the average stress and strain components in the different subcells. The new derivations are carried out assuming the unit cell is subject to uniform average strain rate for each time step. Micromechanical modes of deformations, mode 1 to mode 6, are used to describe the relations between the average stress and strain components of the different subcells.

The notations for the stress and strain vectors, defined in this section, are:

$$\sigma_i^{(\alpha)} = [\sigma_{11}, \sigma_{22}, \sigma_{33}, \tau_{12}, \tau_{13}, \tau_{23}]^T \quad i = 1, \dots, 6 \quad (83)$$

$$\epsilon_i^{(\alpha)} = [\epsilon_{11}, \epsilon_{22}, \epsilon_{33}, \gamma_{12}, \gamma_{13}, \gamma_{23}]^T \quad \alpha = 1, \dots, 9 \quad (84)$$

where, (α) denotes the subcell number. The total volume of the UC is taken to be equal to one to simplify the fiber and matrix volume calculations for estimates of the overall mechanical response. The relative volume of each of the nine subcells, denoted by v_α , can be easily calculated from Figure 27. The axial strains in the subcells are the same and equal to the overall strain in the UC. This is basic first order axial displacement continuity and similar to the well-known Voigt model. Therefore, the longitudinal relations (mode 11) are:

$$d\epsilon_1^{(1)} = d\epsilon_1^{(2)} = d\epsilon_1^{(3)} = d\epsilon_1^{(4)} = d\epsilon_1^{(5)} = d\epsilon_1^{(6)} = d\epsilon_1^{(7)} = d\epsilon_1^{(8)} = d\epsilon_1^{(9)} = d\bar{\epsilon}_1 \quad (85)$$

$$v_1 d\sigma_1^{(1)} + v_2 d\sigma_1^{(2)} + v_3 d\sigma_1^{(3)} + \dots + v_9 d\sigma_1^{(9)} = d\bar{\sigma}_1 \sigma \quad (86)$$

Consideration of the interfaces normal to the x_2 direction, yields the traction continuity conditions for modes 22 and 12, respectively. The corresponding strain compatibility conditions for these modes follow from considering the contribution of subcells (1), (2), and (5), the assembly of subcells (3), (4) and (6), and the third row of subcells (7), (8), and (9). These relations are expressed for mode 22 as:

$$d\sigma_2^{(1)} = d\sigma_2^{(2)} = d\sigma_2^{(7)} \quad (87)$$

$$d\sigma_2^{(2)} = d\sigma_2^{(4)} = d\sigma_2^{(8)} \quad (88)$$

$$d\sigma_2^{(5)} = d\sigma_2^{(6)} = d\sigma_2^{(9)} \quad (89)$$

$$v_1 d\epsilon_2^{(1)} + v_2 d\epsilon_2^{(2)} + v_5 d\epsilon_2^{(5)} = (v_1 + v_2 + v_5) d\bar{\epsilon}_2 \quad (90)$$

$$v_3 d\epsilon_2^{(3)} + v_4 d\epsilon_2^{(4)} + v_6 d\epsilon_2^{(6)} = (v_3 + v_4 + v_6) d\bar{\epsilon}_2 \quad (91)$$

$$v_7 d\epsilon_2^{(7)} + v_8 d\epsilon_2^{(8)} + v_9 d\epsilon_2^{(9)} = (v_7 + v_8 + v_9) d\bar{\epsilon}_2 \epsilon \quad (92)$$

For mode 12 or mode 4, the relations are:

$$d\sigma_4^{(1)} = d\sigma_4^{(2)} = d\sigma_4^{(7)} \quad (93)$$

$$d\sigma_4^{(2)} = d\sigma_4^{(4)} = d\sigma_4^{(8)} \quad (94)$$

$$d\sigma_4^{(5)} = d\sigma_4^{(6)} = d\sigma_4^{(9)} \quad (95)$$

$$v_1 d\epsilon_4^{(1)} + v_2 d\epsilon_4^{(3)} + v_7 d\epsilon_4^{(7)} = (v_1 + v_3 + v_7) d\bar{\epsilon}_4 \quad (96)$$

$$v_2 d\epsilon_4^{(2)} + v_4 d\epsilon_4^{(3)} + v_8 d\epsilon_4^{(8)} = (v_2 + v_4 + v_8) d\bar{\epsilon}_4 \quad (97)$$

$$v_5 d\epsilon_4^{(5)} + v_6 d\epsilon_4^{(3)} + v_9 d\epsilon_4^{(9)} = (v_5 + v_6 + v_9) d\bar{\epsilon}_4 \epsilon \quad (98)$$

Consideration of the interfaces normal to the x_3 direction yields the traction continuity conditions for modes 22 and 12, respectively. The corresponding strain compatibility conditions for these modes follow from considering subcells (1) and (3), and subcells (2) and (4), respectively, to be connected in series. These relations are expressed for mode 33 as:

$$d\sigma_3^{(1)} = d\sigma_3^{(2)} = d\sigma_3^{(7)} \quad (99)$$

$$d\sigma_3^{(2)} = d\sigma_3^{(4)} = d\sigma_3^{(8)} \quad (100)$$

$$d\sigma_3^{(5)} = d\sigma_3^{(6)} = d\sigma_3^{(9)} \quad (101)$$

$$v_1 d\epsilon_3^{(1)} + v_2 d\epsilon_3^{(3)} + v_7 d\epsilon_3^{(7)} = (v_1 + v_3 + v_7) d\bar{\epsilon}_3 \quad (102)$$

$$v_2 d\epsilon_3^{(2)} + v_4 d\epsilon_3^{(3)} + v_8 d\epsilon_3^{(8)} = (v_2 + v_4 + v_8) d\bar{\epsilon}_3 \quad (103)$$

$$v_5 d\epsilon_3^{(5)} + v_6 d\epsilon_3^{(3)} + v_9 d\epsilon_3^{(9)} = (v_5 + v_6 + v_9) d\bar{\epsilon}_3 \quad (104)$$

For mode 13, the relations are:

$$d\sigma_5^{(1)} = d\sigma_5^{(3)} = d\sigma_5^{(7)} \quad (105)$$

$$d\sigma_5^{(2)} = d\sigma_5^{(4)} = d\sigma_5^{(8)} \quad (106)$$

$$d\sigma_5^{(5)} = d\sigma_5^{(6)} = d\sigma_5^{(9)} \quad (107)$$

$$v_1 d\epsilon_5^{(1)} + v_3 d\epsilon_5^{(3)} + v_7 d\epsilon_5^{(7)} = (v_1 + v_3 + v_7) d\bar{\epsilon}_5 \quad (108)$$

$$v_2 d\epsilon_5^{(2)} + v_4 d\epsilon_5^{(4)} + v_8 d\epsilon_5^{(8)} = (v_2 + v_4 + v_8) d\bar{\epsilon}_5 \quad (109)$$

$$v_5 d\epsilon_5^{(5)} + v_6 d\epsilon_5^{(6)} + v_9 d\epsilon_5^{(9)} = (v_5 + v_6 + v_9) d\bar{\epsilon}_5 \quad (110)$$

Finally, in the transverse shear mode, the traction continuity at all the interfaces between the subcells must be satisfied. Since the subcells have a constant stress, the relations for the transverse shear mode, mode 23 or mode 6, are expressed as:

$$d\sigma_6^{(1)} = d\sigma_6^{(2)} = d\sigma_6^{(3)} = d\sigma_6^{(4)} = d\sigma_6^{(5)} = d\sigma_6^{(6)} = d\sigma_6^{(7)} = d\sigma_6^{(8)} = d\sigma_6^{(9)} \quad (111)$$

$$v_1 d\epsilon_6^{(1)} + v_2 d\epsilon_6^{(2)} + v_3 d\epsilon_6^{(3)} + \dots + v_9 d\epsilon_6^{(9)} = d\bar{\epsilon}_6 \epsilon \quad (112)$$

It is instructive to recall the definition for the UC average strain:

$$\frac{1}{V} \sum_{\alpha=1}^9 V_{\alpha} d\epsilon_i^{(\alpha)} = d\epsilon_i \quad i = 1, 2, \dots, 6 \quad (113)$$

Note that all the strain compatibility relations in Equations (2)-(7), explicitly satisfy Equation 113. The only independent relation that is not identically satisfied in Equation 113 is the transverse shear case, $i = 6$. Therefore, this relation is added and considered as a compatibility relation. Next, the incremental stress-strain relations are expressed for each subcell as:

$$d\sigma_i^{(\alpha)} = C_{ij}^{(\alpha)} d\epsilon_j^{(\alpha)} \quad i = 1, 2, \dots, 9 \quad (114)$$

The UC average stress increment is:

$$\frac{1}{V} \sum_{\alpha=1}^9 V_{\alpha} d\sigma_i^{(\alpha)} = d\sigma_i \quad i = 1, 2, \dots, 6 \quad (115)$$

For a given average strain increment imposed on the UC, Equations 85 to 115 provide a system of 114 equations. The 114 unknowns are:

$$d\sigma_i, d\sigma_i^{(\alpha)}, d\epsilon_i^{(\alpha)} \quad \alpha = 1, 2, \dots, 9; \quad i = 1, 2, \dots, 6 \quad (116)$$

These unknowns can be further reduced by using the strain compatibility relations and divide the variables into two independent and dependent sets. The combined set

of equations that describe the strain compatibility and the traction continuity equations (micromechanical constraints) can ultimately be written in a general incremental form as:

$$dR_\sigma = \Gamma_i^\sigma(d\sigma^\alpha, d\epsilon^{(\alpha)}, d\epsilon, V_{(\alpha)}, \alpha = 1, 2, \dots, N) = 0; \quad i = 1, \dots, a \quad (117)$$

Equation 117 is the linearized incremental form of the micromechanical relations. It can be solved to generate the tangential incremental update and evaluate the current strain-interaction matrices for the subcells assuming linear material behavior in the subcells along with no damage within the current step. The incremental form of the traction-continuity relations along with its total form, i.e., dR_σ and its total form R_σ , can be used to iteratively solve for the micromechanical equations since the incremental update of the variable from the linearized relation will almost always generate nonlinear response at the constitutive levels of the matrix and interface subcells. The incremental form of the stress-strain relations in all the subcells can be generally expressed in incremental fashion as:

$$dR_\epsilon = \Gamma_j^\epsilon(C^\alpha, d\epsilon^{(\alpha)}, d\epsilon, V_{(\alpha)}, \alpha = 1, 2, \dots, N) = 0; \quad j = 1, \dots, b \quad (118)$$

At any given state of deformations, the linearized micromechanical equations can be arranged in a general compact incremental form as

$$\left[\begin{array}{c} \\ \\ \mathbf{A} \\ \\ \end{array} \right]_{6N \times 6N} \left\{ \begin{array}{c} d\epsilon^{(1)} \\ d\epsilon^{(2)} \\ \dots \\ \dots \\ \dots \\ d\epsilon^{(N)} \end{array} \right\}_{6N \times 1} = \left[\begin{array}{c} \\ \\ \mathbf{D} \\ \\ \end{array} \right]_{6N \times 6} \left\{ \begin{array}{c} \\ \\ d\bar{\epsilon} \\ \\ \end{array} \right\}_{6 \times 1} \quad (119)$$

The left strain vector represents the unknown strains in all the subcells. The matrix, \mathbf{A} , is composed from known values of the current tangent stiffness matrices of the subcells. The right-hand strain vector, $d\bar{\epsilon}$, is the overall UC average strain. Equation 119 can be rearranged by dividing the subcells strain components into two dependent groups with (a) and (b) number of components, respectively to yield a new compact form that can be solved numerically in an efficient manner. The general structure of the linearized micromechanical equations for our micromodel is:

$$\begin{Bmatrix} dR_{\epsilon} \\ dR_{\sigma} \end{Bmatrix}_{\begin{smallmatrix} (a \times 1) \\ (b \times 1) \end{smallmatrix}} \begin{bmatrix} I_{(a \times a)} & \bar{\mathbf{A}}_{ab} \\ \bar{\mathbf{A}}_{ba} & \bar{\mathbf{A}}_{bb} \end{bmatrix}_{\begin{smallmatrix} (a \times b) \\ (b \times b) \end{smallmatrix}} \begin{Bmatrix} d\epsilon_a \\ d\epsilon_b \end{Bmatrix}_{\begin{smallmatrix} (a \times 1) \\ (b \times 1) \end{smallmatrix}} = \begin{bmatrix} \bar{D}_a \\ 0 \end{bmatrix}_{\begin{smallmatrix} (a \times 6) \\ (b \times 6) \end{smallmatrix}} \left\{ \begin{matrix} d\bar{\epsilon} \\ \end{matrix} \right\}_{(6 \times 1)} \quad (120)$$

The bar notation over the components of the (\mathbf{A}) matrix denotes the new arrangement of the terms of the original matrix. This is a general formulation of any UC that may have a different number of subcells as the special case presented here, namely $N = 9$. Once Equation 119 or 120 are solved, the incremental stress in each of the subcells and the average stress of the UC can be back calculated using the incremental stress-strain relations. The incremental strain-concentration matrices are generally expressed by:

$$\begin{bmatrix} B^{(1)} \\ B^{(2)} \\ \vdots \\ B^{(N)} \end{bmatrix} = \begin{bmatrix} & & \\ & \mathbf{A}^{-1} & \\ & & \end{bmatrix} \begin{bmatrix} \mathbf{D} \end{bmatrix} \quad (121)$$

The stress analysis of a micromechanical RUC becomes a straight forward procedure as a result of this formulation. Given an average strain increment and the history of deformations in the subcells, the strain interaction matrices are formed using Equation 121. The strain increments are subsequently formed in each of the

subcells followed by the corresponding stress increments. This procedure is a linearized incremental stress analysis and will be referred to as the trial state. If only this linearized trial analysis is used, two types of error will result at each trial increment, and will accumulate during the analysis. It is important to mention, however, that the strain compatibility and traction continuity constraints are exactly satisfied by the trial state, which is composed of tangential approximations. The first error occurs in the strain increments because the strain-interaction matrices are derived using the tangent stiffness matrices of the subcells at the beginning of the increment. The second error occurs as a result of using the tangent stiffness to compute the stress increment. Therefore, the proposed correction scheme is important in order to accurately account for the nonlinear constitutive (with or without damage) material behavior (prediction) and its associated error in the incremental micromechanical equations.

3.3.4 The HFGMC micromechanical modeling framework

The High Fidelity Generalized Method of Cells (HFGMC) is a computational nonlinear micromechanical model for multi-phase composites. A more thorough review review of the HFGMC model can be found in Aboudi [3] and in Haj-Ali and Aboudi [58] where the modified form now includes nonlinear algorithms for implicit integration with tailored stress correction schemes allowing for iterative error reduction through minimization of the residual vector, and multi-scale features extending the capabilities of the model for greater efficiency in capturing the local and global load re-distribution that is associated with nonlinear and damage effects in large-scale structural computational finite element models consisting of doubly periodic multi-phase composite media. Classical nonlinear micromechanical models of multi-phase materials are capable of capturing the nonlinear effective response of the material but neglect the local spatial variation of the deformation fields within the representative

microstructure. The HFGMC has the capability of predicting local nonlinear mechanical behavior of periodic multi-phase materials subject to remote loading through a modeling framework that allows for a detailed description of the constituents and spatial deformations between the phases. Multiphase composites are analyzed within the HFGMC framework with nonlinear elastic, elastoplastic and viscoplastic constituents Aboudi2004.

The HFGMC has been used to analyze fully coupled electro-magneto-thermo-elastic multi-phase composites [5], fiber-matrix debonding in metal matrix composites [19], thermomechanical analysis of internally cooled structures at elevated temperatures for aerospace engine applications [11], adhesively bonded composite joints [20], and internal pore pressure for the analysis of foam insulation of the external tank of the space shuttle [18]. This framework is based on the homogenization technique of composites with periodic microstructure as depicted by the repeating unit cell (RUC) in Figure 28. The RUC in of a composite material system, Figure 29, is divided into an arbitrary number of rectangular cells each assigned with a material constituent with nonlinear homogeneous properties. The size and constituent volume fraction is defined by the indices $(\beta\gamma)$. The dimensions of the cell along the 2 and 3 axes are denoted by h_β and l_γ , respectively. In the present doubly periodic case of continuous fibers, a local coordinate system $(y_2^{(\beta)}, y_3^{(\gamma)})$ is introduced in each cell whose origin is located at its center, see Figure 29.

The derivation of the HFGMC shown here was developed by Haj-Ali and Aboudi [58]. This model is used to calibrate the material system using values taken from the literature on the constituents of the microstructure and limited experimental testing to achieve a close estimate of the actual nonlinear anisotropic behavior, and then the calibrated material model is used to predict the nonlinear anisotropic behavior under a multi-axial state of stress in a particular hybrid bio-composite system for this study. Volumetric equilibrium, traction and displacement continuities are satisfied in

an average sense by the HFGMC framework with a higher order polynomial form for the displacement field in the unit cell as shown in Figure 28.

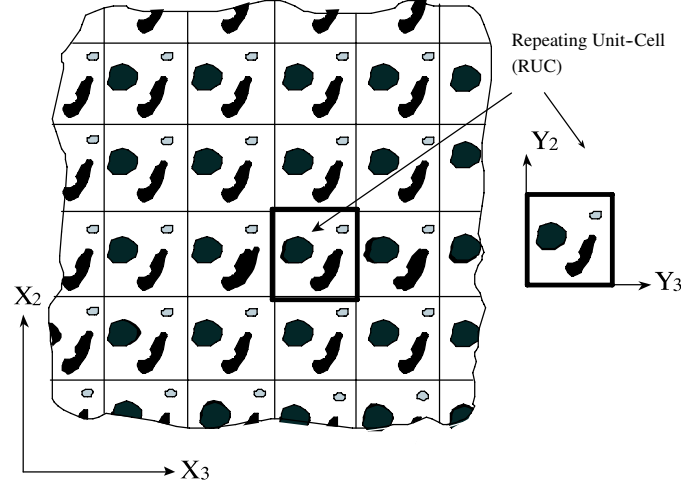


Figure 28: Schematic illustration of a unidirectional periodic array in the global x_2-x_3 plane of multiphase composite media with its repeating unit-cell (RUC), defined with respect to its y_2-y_3 local coordinate system.

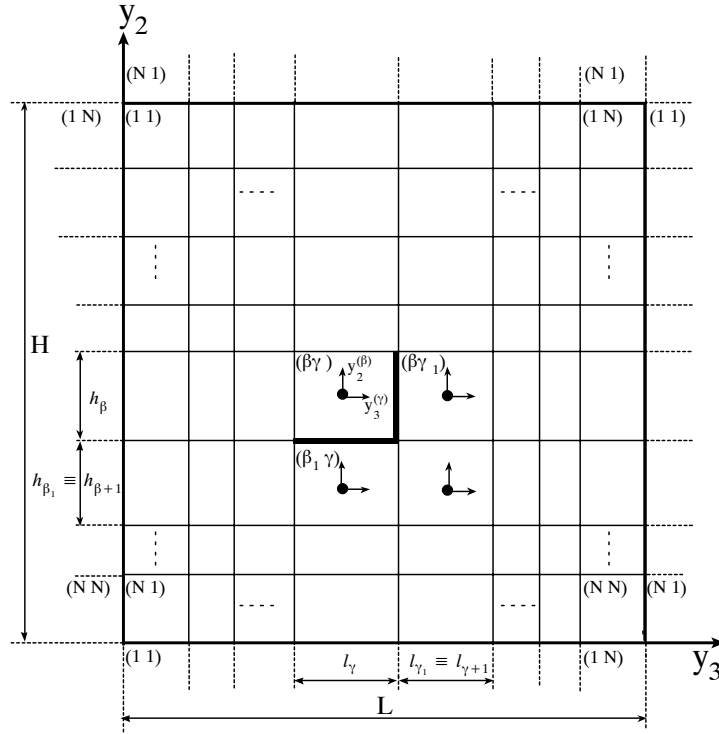


Figure 29: General arrangement of cells and their geometry and coordinate systems for the HFGMC-RUC model. Mirrored cells-interfaces are illustrated to enforce the periodic boundary conditions.

The overall displacement field, \bar{u} , is a function of the global coordinate system. Each subcell has a local displacement field, u , in a local-global coordinance system, x and y .

$$\bar{\mathbf{u}} = \bar{\mathbf{u}}(x) \quad (122)$$

$$\mathbf{u}^{(\beta\gamma)} = \mathbf{u}^{(\beta\gamma)}(x, y) \quad (123)$$

In the framework of the HFGMC model for periodic composites, the displacement vector in the cell $(\beta\gamma)$ is given , e.g. Aboudi [6], by the higher-order polynomial form

$$\begin{aligned} \mathbf{u}^{(\beta\gamma)} &= \bar{u} + \mathbf{W}_{(00)}^{(\beta\gamma)} + y_2^{(\beta)} \mathbf{W}_{(10)}^{(\beta\gamma)} + y_3^{(\gamma)} \mathbf{W}_{(01)}^{(\beta\gamma)} \\ &+ \frac{1}{2}(3y_2^{(\beta)2} - \frac{h_\beta^2}{4}) \mathbf{W}_{(20)}^{(\beta\gamma)} + \frac{1}{2}(3y_3^{(\gamma)2} - \frac{l_\gamma^2}{4}) \mathbf{W}_{(02)}^{(\beta\gamma)} \end{aligned} \quad (124)$$

where $\bar{\epsilon}$ is the externally applied average strain. The coefficient variables vectors, $\mathbf{W}_{(mn)}^{(\beta\gamma)}$, represent the volume averaged displacement in the case of $m = n = 0$, which together with the additional higher-order terms have to be determined.

The strain vector at each cell is defined by

$$\boldsymbol{\epsilon}^{(\beta\gamma)} \equiv \{\epsilon_{11}, \epsilon_{22}, \epsilon_{33}, 2\epsilon_{12}, 2\epsilon_{13}, 2\epsilon_{23}\}^{(\beta\gamma)} \quad (125)$$

After some algebraic manipulations, it is possible to represent the strain vector in the form

$$\boldsymbol{\epsilon}^{(\beta\gamma)} = \bar{\boldsymbol{\epsilon}} + P_{(10)} \mathbf{W}_{(10)}^{(\beta\gamma)} + P_{(01)} \mathbf{W}_{(01)}^{(\beta\gamma)} + P_{(20)} \mathbf{W}_{(20)}^{(\beta\gamma)} y_2^{(\beta)} + P_{(02)} \mathbf{W}_{(02)}^{(\beta\gamma)} y_3^{(\gamma)} \quad (126)$$

where,

$$P_{(10)} = \begin{bmatrix} 0 & 0 & 0 \\ 0 & 0 & 0 \\ 0 & 0 & 1 \\ 0 & 0 & 0 \\ 1 & 0 & 0 \\ 0 & 1 & 0 \end{bmatrix}, \quad P_{(01)} = \begin{bmatrix} 0 & 0 & 0 \\ 0 & 1 & 0 \\ 0 & 0 & 0 \\ 1 & 0 & 0 \\ 0 & 0 & 0 \\ 0 & 0 & 1 \end{bmatrix} \quad (127)$$

and $P_{(20)} = 3P_{(10)}$, $P_{(02)} = 3P_{(01)}$.

The average strain in the cell $(\beta\gamma)$ can be identified as

$$\bar{\epsilon}^{(\beta\gamma)} = \bar{\epsilon} + P_{(10)} \mathbf{W}_{(10)}^{(\beta\gamma)} + P_{(01)} \mathbf{W}_{(01)}^{(\beta\gamma)} \quad (128)$$

The strain influence matrix $\mathbf{B}^{(\beta\gamma)}$ of the cell can be expressed in an incremental form by

$$\Delta \bar{\epsilon}^{(\beta\gamma)} \equiv \mathbf{B}^{(\beta\gamma)} \Delta \bar{\epsilon} = \left[\mathbf{I} + P_{(10)} \hat{\mathbf{D}}_{(10)}^{(\beta\gamma)} + P_{(01)} \hat{\mathbf{D}}_{(01)}^{(\beta\gamma)} \right] \Delta \bar{\epsilon} \quad (129)$$

with \mathbf{I} being the identity matrix. In addition,

$$\hat{\mathbf{D}}_{(10)}^{(\beta\gamma)} \Delta \bar{\epsilon} = \Delta \mathbf{W}_{(10)}^{(\beta\gamma)}, \quad \hat{\mathbf{D}}_{(01)}^{(\beta\gamma)} \Delta \bar{\epsilon} = \Delta \mathbf{W}_{(01)}^{(\beta\gamma)} \quad (130)$$

where $\hat{\mathbf{D}}_{(mn)}^{(\beta\gamma)}$ are determined after the solution of the entire coupled governing equations of the cells.

The resulting linear expansion of the stress vector can be expressed as

$$\boldsymbol{\sigma}^{(\beta\gamma)} = \bar{\boldsymbol{\sigma}}^{(\beta\gamma)} + \boldsymbol{\sigma}_{(10)}^{(\beta\gamma)} y_2^{(\beta)} + \boldsymbol{\sigma}_{(01)}^{(\beta\gamma)} y_3^{(\gamma)} \quad (131)$$

where $\bar{\boldsymbol{\sigma}}^{(\beta\gamma)}$ is the average stress in the cell $(\beta\gamma)$ and $\boldsymbol{\sigma}_{(mn)}^{(\beta\gamma)}$ are higher-order stresses which can be directly expressed in terms of the stress moments defined by

$$\mathbf{S}_{(mn)}^{(\beta\gamma)} = \frac{1}{h_\beta l_\gamma} \int_{-h_\beta/2}^{h_\beta/2} \int_{-l_\gamma/2}^{l_\gamma/2} \boldsymbol{\sigma}^{(\beta\gamma)} (y_2^{(\beta)})^m (y_3^{(\gamma)})^n dy_2^{(\beta)} dy_3^{(\gamma)} \quad (132)$$

These moments were previously employed in the original derivation of the HFGMC (see Aboudi [6]). The current form of the stress vector is exactly equivalent to the original derivation:

$$\boldsymbol{\sigma}_{(10)}^{(\beta\gamma)} = \frac{12}{h_\beta^2} \mathbf{S}_{(10)}^{(\beta\gamma)}, \quad \boldsymbol{\sigma}_{(01)}^{(\beta\gamma)} = \frac{12}{l_\gamma^2} \mathbf{S}_{(01)}^{(\beta\gamma)} \quad (133)$$

The standard pointwise equilibrium equations $\nabla \cdot \boldsymbol{\sigma} = \mathbf{0}$, lead, in the framework of HFGMC theory, to the volume-average form

$$L_2 \boldsymbol{\sigma}_{(10)}^{(\beta\gamma)} + L_3 \boldsymbol{\sigma}_{(01)}^{(\beta\gamma)} = \mathbf{0} \quad (134)$$

where L_2 and L_3 are given by the Boolean matrices:

$$L_2 = \begin{bmatrix} 0 & 0 & 0 & 1 & 0 & 0 \\ 0 & 1 & 0 & 0 & 0 & 0 \\ 0 & 0 & 0 & 0 & 0 & 1 \end{bmatrix}, \quad L_3 = \begin{bmatrix} 0 & 0 & 0 & 0 & 1 & 0 \\ 0 & 0 & 0 & 0 & 0 & 1 \\ 0 & 0 & 1 & 0 & 0 & 0 \end{bmatrix} \quad (135)$$

For the general case of a nonlinear material filling the cell $(\beta\gamma)$, the incremental form of its constitutive relation is given by

$$\Delta\boldsymbol{\sigma}^{(\beta\gamma)} = \mathbf{C}^{(\beta\gamma)} \Delta\boldsymbol{\epsilon}^{(\beta\gamma)} \quad (136)$$

where $\mathbf{C}^{(\beta\gamma)}$ is the proper instantaneous or consistent fourth-order tangent stiffness tensor that is selected based on the considered nonlinear material behavior within the cell, such as total deformation theory, incremental plasticity, nonlinear viscoelasticity, and viscoplasticity. Standard forms of the fourth-order tangent or consistent tangent tensors for these material models can be found in Simo and Hughes [116], Khan and Huang [80] and ABAQUS [2]. For the particular Bodner-Partom viscoplastic theory, Bodner [25], the time-dependent tangent tensor has been derived by Paley and Aboudi [101] in the form

$$C_{ijkl}^{(\beta\gamma)} = \left[\lambda \delta_{ij} \delta_{kl} + \mu (\delta_{ik} \delta_{jl} + \delta_{il} \delta_{jk}) - 2\mu \frac{s_{rt} \dot{\epsilon}_{rt}^P}{s_{pq} \dot{\epsilon}_{pq}} \cdot \frac{s_{ij} s_{kl}}{s_{mn} s_{mn}} \right]^{(\beta\gamma)} \quad (137)$$

where λ and μ are the Lamé' constants of the material filling the cell $(\beta\gamma)$, s_{ij} is the deviatoric part of the stress σ_{ij} in the cell, ϵ_{ij}^P is the corresponding plastic (inelastic) strain component and δ_{ij} is the Kronecker delta.

The incremental forms of the constitutive models for the different phases are used in the linearized formulation of the HFGMC. In addition, the corresponding total integrated constitutive forms are also employed to derive the HFGMC nonlinear equations using total microvariables and stresses in the cells.

The incremental stress is of the form

$$\Delta\boldsymbol{\sigma}^{(\beta\gamma)} = \Delta\bar{\boldsymbol{\sigma}}^{(\beta\gamma)} + \Delta\boldsymbol{\sigma}_{(10)}^{(\beta\gamma)} y_2^{(\beta)} + \Delta\boldsymbol{\sigma}_{(01)}^{(\beta\gamma)} y_3^{(\gamma)} \quad (138)$$

By substituting the incremental strain given by Eq. (126) and comparing with Eq. (138) leads to the following relations

$$\begin{aligned}\Delta \bar{\boldsymbol{\sigma}}^{(\beta\gamma)} &= \mathbf{C}^{(\beta\gamma)} \Delta \bar{\boldsymbol{\epsilon}} + \mathbf{C}^{(\beta\gamma)} P_{(10)} \Delta \mathbf{W}_{(10)}^{(\beta\gamma)} + \mathbf{C}^{(\beta\gamma)} P_{(01)} \Delta \mathbf{W}_{(01)}^{(\beta\gamma)} \\ \Delta \boldsymbol{\sigma}_{(10)}^{(\beta\gamma)} &= \mathbf{C}^{(\beta\gamma)} P_{(20)} \Delta \mathbf{W}_{(20)}^{(\beta\gamma)} \\ \Delta \boldsymbol{\sigma}_{(01)}^{(\beta\gamma)} &= \mathbf{C}^{(\beta\gamma)} P_{(02)} \Delta \mathbf{W}_{(02)}^{(\beta\gamma)}\end{aligned}\quad (139)$$

It should be noted that $\Delta \bar{\boldsymbol{\sigma}}^{(\beta\gamma)}$ is the incremental average stress in the cell. These relations are used in the equilibrium equations, Eq. (135), resulting into

$$L_2 \mathbf{C}^{(\beta\gamma)} P_{(20)} \Delta \mathbf{W}_{(20)}^{(\beta\gamma)} + L_3 \mathbf{C}^{(\beta\gamma)} P_{(02)} \Delta \mathbf{W}_{(02)}^{(\beta\gamma)} = 0 \quad (140)$$

This equation can be equivalently expressed in the compact form

$$A_{2(20)}^{(\beta\gamma)} \Delta \mathbf{W}_{(20)}^{(\beta\gamma)} + A_{3(02)}^{(\beta\gamma)} \Delta \mathbf{W}_{(02)}^{(\beta\gamma)} = 0 \quad (141)$$

where

$$A_{i(mn)}^{(\beta\gamma)} \equiv L_i \mathbf{C}^{(\beta\gamma)} P_{(mn)}, \quad (mn) \neq (00) \quad (142)$$

and

$$A_{i(00)}^{(\beta\gamma)} \equiv L_i \mathbf{C}^{(\beta\gamma)} \quad (143)$$

Next, the traction and displacement continuity are imposed on an integral basis over the interfaces. Consider the two interfaces between the neighboring cells $(\beta\gamma)$ and $(\beta_1\gamma)$, and $(\beta\gamma)$ and $(\beta\gamma_1)$ where $\beta_1 = \beta + 1$ and $\gamma_1 = \gamma + 1$, the displacement continuity conditions are given by

$$\int_{-l_\gamma/2}^{l_\gamma/2} \left[\mathbf{u}^{(\beta\gamma)}|_{y_2^{(\beta)}=-h_\beta/2} - \mathbf{u}^{(\beta_1\gamma)}|_{y_2^{(\beta_1)}=h_{\beta_1}/2} \right] dy_3^{(\gamma)} = \mathbf{0} \quad (144)$$

with $\beta = 1, \dots, N_\beta - 1$ and $\gamma = 1, \dots, N_\gamma$. Similarly, the displacement continuity at the interface whose normal is in the y_3 -direction is

$$\int_{-h_\beta/2}^{h_\beta/2} \left[\mathbf{u}^{(\beta\gamma)}|_{y_3^{(\gamma)}=l_\gamma/2} - \mathbf{u}^{(\beta\gamma_1)}|_{y_3^{(\gamma_1)}=-l_{\gamma_1}/2} \right] dy_2^{(\beta)} = \mathbf{0} \quad (145)$$

with $\beta = 1, \dots, N_\beta$ and $\gamma = 1, \dots, N_\gamma - 1$. The needed displacement periodicity conditions are

$$\int_{-l_\gamma/2}^{l_\gamma/2} \left[\mathbf{u}^{(1\gamma)}|_{y_2^{(1)}=h_1/2} - \mathbf{u}^{(N_\beta\gamma)}|_{y_2^{(N_\beta)}=-h_{N_\beta/2}} \right] dy_3^{(\gamma)} = \mathbf{0} \quad (146)$$

with $\gamma = 1, \dots, N_\gamma$.

$$\int_{-h_\beta/2}^{h_\beta/2} \left[\mathbf{u}^{(\beta 1)}|_{y_3^{(1)}=-l_1/2} - \mathbf{u}^{(\beta N_\gamma)}|_{y_3^{(N_\gamma)}=l_{N_\gamma/2}} \right] dy_2^{(\beta)} = \mathbf{0} \quad (147)$$

with $\beta = 1, \dots, N_\beta$.

The two traction continuity conditions are

$$\int_{-l_\gamma/2}^{l_\gamma/2} \left[L_2 \boldsymbol{\sigma}^{(\beta\gamma)}|_{y_2^{(\beta)}=-h_\beta/2} - L_2 \boldsymbol{\sigma}^{(\beta 1\gamma)}|_{y_2^{(\beta 1)}=h_{\beta 1}/2} \right] dy_3^{(\gamma)} = \mathbf{0} \quad (148)$$

with $\beta = 1, \dots, N_\beta - 1$ and $\gamma = 1, \dots, N_\gamma$.

$$\int_{-h_\beta/2}^{h_\beta/2} \left[L_3 \boldsymbol{\sigma}^{(\beta\gamma)}|_{y_3^{(\gamma)}=l_\gamma/2} - L_3 \boldsymbol{\sigma}^{(\beta\gamma 1)}|_{y_3^{(\gamma 1)}=-l_{\gamma 1}/2} \right] dy_2^{(\beta)} = \mathbf{0} \quad (149)$$

with $\beta = 1, \dots, N_\beta$ and $\gamma = 1, \dots, N_\gamma - 1$. The needed traction periodicity conditions are

$$\int_{-l_\gamma/2}^{l_\gamma/2} \left[L_2 \boldsymbol{\sigma}^{(1\gamma)}|_{y_2^{(1)}=h_1/2} - L_2 \boldsymbol{\sigma}^{(N_\beta\gamma)}|_{y_2^{(N_\beta)}=-h_{N_\beta/2}} \right] dy_3^{(\gamma)} = \mathbf{0} \quad (150)$$

with $\gamma = 1, \dots, N_\gamma$.

$$\int_{-h_\beta/2}^{h_\beta/2} \left[L_3 \boldsymbol{\sigma}^{(\beta 1)}|_{y_3^{(1)}=-l_1/2} - L_3 \boldsymbol{\sigma}^{(\beta N_\gamma)}|_{y_3^{(N_\gamma)}=l_{N_\gamma/2}} \right] dy_2^{(\beta)} = \mathbf{0} \quad (151)$$

with $\beta = 1, \dots, N_\beta$. It should be emphasized that the periodicity relations, Eq. (146)-(146) and (150)-(151), are satisfied by mirroring and extending the cells near the periodic interfaces as shown in Figure 29. Therefore Eqs. (144)-(145) and (146)-(147) are equivalent to the periodic relations by using the proposed mirroring technique. For example, the continuity equations can be applied to satisfy the periodicity conditions by simply performing the shifting operation: $(\beta = N_\beta + 1, \gamma) \implies (1, \gamma)$. Thus Eq.

(144)-(145) and Eq. (148)-(149) can be applied using the outlined mirroring procedure to enforce the periodicity conditions as well.

The four displacement and traction continuity equations, Eq. (144)-(145) and Eq. (148)-(149), can be expressed in the incremental form:

$$\left[\Delta \mathbf{W}_{(00)}^{(\beta\gamma)} - \frac{h_\beta}{2} \Delta \mathbf{W}_{(10)}^{(\beta\gamma)} + \frac{h_\beta^2}{4} \Delta \mathbf{W}_{(20)}^{(\beta\gamma)} \right] - \left[\Delta \mathbf{W}_{(00)}^{(\beta_1\gamma)} + \frac{h_{\beta_1}}{2} \Delta \mathbf{W}_{(10)}^{(\beta_1\gamma)} + \frac{h_{\beta_1}^2}{4} \Delta \mathbf{W}_{(20)}^{(\beta_1\gamma)} \right] = \mathbf{0} \quad (152)$$

$$\left[\Delta \mathbf{W}_{(00)}^{(\beta\gamma)} + \frac{l_\gamma}{2} \Delta \mathbf{W}_{(01)}^{(\beta\gamma)} + \frac{l_\gamma^2}{4} \Delta \mathbf{W}_{(02)}^{(\beta\gamma)} \right] - \left[\Delta \mathbf{W}_{(00)}^{(\beta\gamma_1)} - \frac{l_{\gamma_1}}{2} \Delta \mathbf{W}_{(01)}^{(\beta\gamma_1)} + \frac{l_{\gamma_1}^2}{4} \Delta \mathbf{W}_{(02)}^{(\beta\gamma_1)} \right] = \mathbf{0} \quad (153)$$

$$\begin{aligned} & \left[\mathbf{A}_{2(10)}^{(\beta\gamma)} \Delta \mathbf{W}_{(10)}^{(\beta\gamma)} + \mathbf{A}_{2(01)}^{(\beta\gamma)} \Delta \mathbf{W}_{(01)}^{(\beta\gamma)} - \frac{h_\beta}{2} \mathbf{A}_{2(20)}^{(\beta\gamma)} \Delta \mathbf{W}_{(20)}^{(\beta\gamma)} \right] \\ & - \left[\mathbf{A}_{2(10)}^{(\beta_1\gamma)} \Delta \mathbf{W}_{(10)}^{(\beta_1\gamma)} + \mathbf{A}_{2(01)}^{(\beta_1\gamma)} \Delta \mathbf{W}_{(01)}^{(\beta_1\gamma)} + \frac{h_{\beta_1}}{2} \mathbf{A}_{2(20)}^{(\beta_1\gamma)} \Delta \mathbf{W}_{(20)}^{(\beta_1\gamma)} \right] \\ & = \left[\mathbf{A}_{2(00)}^{(\beta_1\gamma)} - \mathbf{A}_{2(00)}^{(\beta\gamma)} \right] \Delta \bar{\epsilon} \end{aligned} \quad (154)$$

$$\begin{aligned} & \left[\mathbf{A}_{3(10)}^{(\beta\gamma)} \Delta \mathbf{W}_{(10)}^{(\beta\gamma)} + \mathbf{A}_{3(01)}^{(\beta\gamma)} \Delta \mathbf{W}_{(01)}^{(\beta\gamma)} + \frac{l_\gamma}{2} \mathbf{A}_{3(02)}^{(\beta\gamma)} \Delta \mathbf{W}_{(02)}^{(\beta\gamma)} \right] \\ & - \left[\mathbf{A}_{3(10)}^{(\beta\gamma_1)} \Delta \mathbf{W}_{(10)}^{(\beta\gamma_1)} + \mathbf{A}_{3(01)}^{(\beta\gamma_1)} \Delta \mathbf{W}_{(01)}^{(\beta\gamma_1)} - \frac{l_{\gamma_1}}{2} \mathbf{A}_{3(02)}^{(\beta\gamma_1)} \Delta \mathbf{W}_{(02)}^{(\beta\gamma_1)} \right] \\ & = \left[\mathbf{A}_{3(00)}^{(\beta\gamma_1)} - \mathbf{A}_{3(00)}^{(\beta\gamma)} \right] \Delta \bar{\epsilon} \end{aligned} \quad (155)$$

Let us define the vector of incremental variables of each $(\beta\gamma)$ cell as

$$\Delta \mathbf{X}^{(\beta\gamma)} \equiv \left\{ \Delta \mathbf{W}_{(10)}, \Delta \mathbf{W}_{(01)}, \Delta \mathbf{W}_{(00)}, \Delta \mathbf{W}_{(20)}, \Delta \mathbf{W}_{(02)} \right\}^{(\beta\gamma)} \quad (156)$$

Figure 30 illustrates the common interfaces between a cell $(\beta\gamma)$ and its neighboring cells. As previously shown, it is sufficient to consider the continuity conditions at the two interfaces $y_2 = h_\beta/2$ and $y_3 = l_\gamma/2$ (illustrated by bold lines in Figure 30).

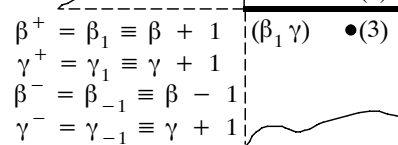


Figure 30: One-cell configuration with its neighboring cells showing its two primary “feed-forward” interfaces along with the location for the stress integration points.

The increment of the residual vector $\mathbf{R}^{(\beta\gamma)}$ for the governing equations is arranged in the order of traction continuity, Eq. (154)-(155), the internal equilibrium equations for the cell, Eq. (141), followed by the displacement continuity, Eq. (152)-(153), written for the above two interfaces:

$$\begin{aligned}\Delta \mathbf{R}^{(\beta\gamma)} &\equiv \left\{ \Delta \mathbf{R}_\sigma, \Delta \mathbf{R}_E, \Delta \mathbf{R}_u \right\}^{(\beta\gamma)} \\ &= \mathbf{T}_1^{(\beta\gamma)} \Delta \mathbf{X}^{(\beta\gamma)} + \mathbf{T}_2^{(\beta_1\gamma)} \Delta \mathbf{X}^{(\beta_1\gamma)} + \mathbf{T}_3^{(\beta\gamma_1)} \Delta \mathbf{X}^{(\beta\gamma_1)} \\ &\quad - \mathbf{D}_1^{(\beta\gamma)} \Delta \bar{\epsilon} - \mathbf{D}_2^{(\beta_1\gamma)} \Delta \bar{\epsilon} - \mathbf{D}_3^{(\beta\gamma_1)} \Delta \bar{\epsilon}\end{aligned}\quad (157)$$

The matrix $\mathbf{T}_1^{(\beta\gamma)}$ operates on the incremental microvariable vector $\Delta \mathbf{X}^{(\beta\gamma)}$ and provides the incremental traction and displacement at the two interfaces within the cell $(\beta\gamma)$. Its structure is given by

$$\mathbf{T}_1^{(\beta\gamma)} = \begin{bmatrix} \mathbf{A}_{2(10)} & \mathbf{A}_{2(01)} & \mathbf{0} & -\frac{h_\beta}{2} \mathbf{A}_{2(20)} & \mathbf{0} \\ \mathbf{A}_{3(10)} & \mathbf{A}_{3(01)} & \mathbf{0} & \mathbf{0} & \frac{l_\gamma}{2} \mathbf{A}_{3(02)} \\ \mathbf{0} & \mathbf{0} & \mathbf{0} & \mathbf{A}_{2(20)} & \mathbf{A}_{3(02)} \\ -\frac{h_\beta}{2} \mathbf{I} & \mathbf{0} & \mathbf{I} & \frac{h_\beta^2}{4} \mathbf{I} & \mathbf{0} \\ \mathbf{0} & \frac{l_\gamma}{2} \mathbf{I} & \mathbf{I} & \mathbf{0} & \frac{l_\gamma^2}{4} \mathbf{I} \end{bmatrix}^{(\beta\gamma)} \quad (158)$$

Similarly, the matrices $\mathbf{T}_2^{(\beta_1\gamma)}$ and $\mathbf{T}_3^{(\beta\gamma_1)}$ operate on the incremental microvariable vectors, $\Delta \mathbf{X}^{(\beta_1\gamma)}$ and $\Delta \mathbf{X}^{(\beta\gamma_1)}$ of the adjacent cells, respectively. They provide the incremental traction and displacement on the other side of the two interfaces. For example, the matrix $\mathbf{T}_3^{(\beta\gamma_1)}$ provides the incremental displacement and stress within the cell $(\beta\gamma_1)$ needed to complete the continuity conditions at the common interface of the adjacent cell $(\beta\gamma)$. These two matrices are of the form

$$\mathbf{T}_2^{(\beta_1\gamma)} = \begin{bmatrix} -\mathbf{A}_{2(10)} & -\mathbf{A}_{2(01)} & \mathbf{0} & -\frac{h_\beta}{2} \mathbf{A}_{2(20)} & \mathbf{0} \\ \mathbf{0} & \mathbf{0} & \mathbf{0} & \mathbf{0} & \mathbf{0} \\ \mathbf{0} & \mathbf{0} & \mathbf{0} & \mathbf{0} & \mathbf{0} \\ -\frac{h_\beta}{2} \mathbf{I} & \mathbf{0} & -\mathbf{I} & -\frac{h_\beta^2}{4} \mathbf{I} & \mathbf{0} \\ \mathbf{0} & \mathbf{0} & \mathbf{0} & \mathbf{0} & \mathbf{0} \end{bmatrix}^{(\beta_1\gamma)} \quad (159)$$

$$\mathbf{T}_3^{(\beta\gamma_1)} = \begin{bmatrix} \mathbf{0} & \mathbf{0} & \mathbf{0} & \mathbf{0} & \mathbf{0} \\ -\mathbf{A}_{3(10)} & -\mathbf{A}_{3(01)} & \mathbf{0} & \mathbf{0} & \frac{l_{\gamma_1}}{2}\mathbf{A}_{3(02)} \\ \mathbf{0} & \mathbf{0} & \mathbf{0} & \mathbf{0} & \mathbf{0} \\ \mathbf{0} & \mathbf{0} & \mathbf{0} & \mathbf{0} & \mathbf{0} \\ \mathbf{0} & \frac{l_{\gamma_1}}{2}\mathbf{I} & -\mathbf{I} & \mathbf{0} & -\frac{l_{\gamma_1}^2}{4}\mathbf{I} \end{bmatrix}^{(\beta\gamma_1)} \quad (160)$$

The \mathbf{D}_i matrices can be viewed as the contribution to the local stresses at the considered two interfaces of the corresponding cells from the externally applied global strain field. Their structure is given by

$$\mathbf{D}_1^{(\beta\gamma)} = \begin{bmatrix} -\mathbf{A}_{2(00)} \\ -\mathbf{A}_{3(00)} \\ 0 \\ 0 \\ 0 \\ 0 \end{bmatrix}^{(\beta\gamma)} \quad \mathbf{D}_2^{(\beta_1\gamma)} = \begin{bmatrix} \mathbf{A}_{2(00)} \\ 0 \\ 0 \\ 0 \\ 0 \\ 0 \end{bmatrix}^{(\beta_1\gamma)} \quad \mathbf{D}_3^{(\beta\gamma_1)} = \begin{bmatrix} 0 \\ \mathbf{A}_{3(00)} \\ 0 \\ 0 \\ 0 \\ 0 \end{bmatrix}^{(\beta\gamma_1)} \quad (161)$$

It is interesting to note that the displacement continuity and equilibrium equations expressed in terms of the incremental micro-variables result in a set of homogeneous algebraic equations. This fact is useful for condensation purposes of the overall system of equations as will be shown later.

The final system of the tangential governing equations is obtained by assembling the contributions from all the cells by utilizing the expressions given by Eq. (157). Figure 31 illustrates the form of the global tangential system of equations highlighting the contribution of a general cell $(\beta\gamma)$.

The expanded form of the vector of variables is

$$\Delta \mathbf{X} = \left\{ \Delta \mathbf{X}^{(11)}, \Delta \mathbf{X}^{(12)}, \dots, \Delta \mathbf{X}^{(N_\beta N_\gamma)} \right\} \quad (162)$$

Alternatively, it is possible to perform the assembly on a cell-by-cell basis where in

Figure 31: Overall tangential system of equations for the HFGMC-RUC model indicating the contribution of cell ($\beta\gamma$) to the system and showing a row of complete equations for this cell.

such a case all indicted matrices in this figure will be solely computed from the cell stiffness and assembled on a column basis.

It is possible to dramatically reduce the computational effort by employing a condensation procedure. To this end, the previously identified homogeneous and non-homogeneous equations at the cell level can be grouped into two parts. The re-partitioned system has the form

$$\begin{bmatrix} \mathbf{A}_{\sigma\sigma} & \mathbf{A}_{\sigma u} \\ \mathbf{A}_{u\sigma} & \mathbf{A}_{uu} \end{bmatrix} \begin{Bmatrix} \Delta \mathbf{X}_\sigma \\ \Delta \mathbf{X}_u \end{Bmatrix} = \begin{bmatrix} \mathbf{D} \\ \mathbf{0} \end{bmatrix} \{ \Delta \bar{\epsilon} \} \quad (163)$$

The terms $\mathbf{A}_{\sigma\sigma}$ and \mathbf{A}_{uu} in Eq. (163) involve the traction continuity (non-homogeneous equations) on the one hand, and the equilibrium and displacement continuity (homogeneous equations) on the other hand. The off diagonal terms $\mathbf{A}_{\sigma u}$ and $\mathbf{A}_{u\sigma}$ involve the mixed terms that emerge from re-partitioning the system of equations. The two parts of the vector of variables, $\Delta \mathbf{X}_\sigma$ and $\Delta \mathbf{X}_u$, have similar definitions. The solution can be represented symbolically as:

$$\Delta \mathbf{X} = \mathbf{A}^{-1} \mathbf{D} \Delta \bar{\epsilon} \equiv \hat{\mathbf{D}} \Delta \bar{\epsilon} \quad (164)$$

where the square matrix \mathbf{A} that appears on the left-hand-side of Eq. (163) has the dimension $15N_\beta N_\gamma \times 15N_\beta N_\gamma$ in a non-condensed form. However, by performing the condensation procedure the dimension of the condensed system reduces to $6N_\beta N_\gamma \times 6N_\beta N_\gamma$.

The overall (global) tangential stiffness matrix defined from the effective incremental stress-strain relation, $\Delta \bar{\sigma} = \mathbf{C}^* \Delta \bar{\epsilon}$, of the composite can be obtained by determining the influence matrices $\mathbf{B}^{(\beta\gamma)}$ defined by the incremental form of Eqs. (128)-(130). The needed matrices $\hat{\mathbf{D}}_{(10)}^{(\beta\gamma)}$ and $\hat{\mathbf{D}}_{(01)}^{(\beta\gamma)}$ can be identified from $\hat{\mathbf{D}}$ in Eq.

(164) which can be partitioned as follows

$$\hat{\mathbf{D}}^{(\beta\gamma)} = \begin{bmatrix} \hat{\mathbf{D}}_{(10)} \\ \hat{\mathbf{D}}_{(01)} \\ \hat{\mathbf{D}}_{(00)} \\ \hat{\mathbf{D}}_{(20)} \\ \hat{\mathbf{D}}_{(02)} \end{bmatrix}^{(\beta\gamma)}, \quad (165)$$

Consequently, the effective tangential stiffness of the composite can be readily evaluated as follows (Haj-Ali [57], Aboudi [6])

$$\mathbf{C}^* = \frac{1}{HL} \sum_{\beta=1}^{N_\beta} \sum_{\gamma=1}^{N_\gamma} h_\beta l_\gamma \mathbf{C}^{(\beta\gamma)} \mathbf{B}^{(\beta\gamma)} \equiv \sum_{\beta=1}^{N_\beta} \sum_{\gamma=1}^{N_\gamma} h_\beta l_\gamma \mathbf{B}^{T(\beta\gamma)} \mathbf{C}^{T(\beta\gamma)} \quad (166)$$

which shows the symmetry of the effective tangential stiffness of the composite.

Next, we derive the residual vector of the governing equation for a characteristic cell $(\beta\gamma)$ that is needed in order to obtain the error of the nonlinear system during the iterative solution. The total (rather than incremental) interfacial displacements and stresses are determined from the total strains derived from the trial microvariables. These field variables are evaluated at both sides of the neighboring cells as illustrated in Figure 30. The locations of the integration stress points are indicated by the solid circles. It should be noted that the displacement residuals are explicitly zero since they do not involve stiffness variables. The residual vector of cell $(\beta\gamma)$ is given by:

$$\mathbf{R}^{(\beta\gamma)} = \begin{bmatrix} \int [L_2 \boldsymbol{\sigma}^{(\beta\gamma)} - L_2 \boldsymbol{\sigma}^{(\beta_1\gamma)}] dy_3^{(\gamma)} \\ \int [L_3 \boldsymbol{\sigma}^{(\beta\gamma)} - L_3 \boldsymbol{\sigma}^{(\beta\gamma_1)}] dy_2^{(\beta)} \\ L_2 \boldsymbol{\sigma}_{(10)}^{(\beta\gamma)} - L_3 \boldsymbol{\sigma}_{(01)}^{(\beta\gamma)} \\ 0 \\ 0 \end{bmatrix} \longrightarrow \begin{bmatrix} L_2 \boldsymbol{\sigma}^{(\beta\gamma)_1} - L_2 \boldsymbol{\sigma}^{(\beta_1\gamma)_3} \\ L_3 \boldsymbol{\sigma}^{(\beta\gamma)_2} - L_3 \boldsymbol{\sigma}^{(\beta\gamma_1)_4} \\ L_2 \boldsymbol{\sigma}_{(10)}^{(\beta\gamma)} - L_3 \boldsymbol{\sigma}_{(01)}^{(\beta\gamma)} \\ 0 \\ 0 \end{bmatrix} \quad (167)$$

where the first two components define the traction continuities in a total form, whereas the third term stands for the total form of the equilibrium equations in the cell. The

transition from the mathematical definition of the residual vector to its numerical form is expressed by the two parts of Eq. (167). The equilibrium equations involve higher-order stresses that are obtained from the total stress values evaluated at the stress integration points:

$$\boldsymbol{\sigma}_{(10)}^{(\beta\gamma)} = \frac{1}{h_\beta} \left(\boldsymbol{\sigma}^{(\beta\gamma)_3} - \boldsymbol{\sigma}^{(\beta\gamma)_2} \right); \quad \boldsymbol{\sigma}_{(01)}^{(\beta\gamma)} = \frac{1}{l_\gamma} \left(\boldsymbol{\sigma}^{(\beta\gamma)_2} - \boldsymbol{\sigma}^{(\beta\gamma)_4} \right) \quad (168)$$

The cell's residual vector $\mathbf{R}^{(\beta\gamma)}$ is used in the process of assembling the overall residual vector of the HFGMC model \mathbf{R}_{HFGMC} given by

$$\mathbf{R}_{HFGMC} = \left\{ \mathbf{R}^{(11)}, \dots, \mathbf{R}^{(\beta\gamma)}, \dots, \mathbf{R}^{(N_\beta N_\gamma)} \right\} \quad (169)$$

This residual vector should be equal to zero in order to solve for the nonlinear HFGMC equations. This is numerically achieved by requiring that its norm should be sufficiently small. In the case where a mixed stress and strain combination is applied (e.g., a uniaxial transverse loading defined by: $\bar{\epsilon}_{22} \neq 0$ and $\bar{\sigma}_{ij} = 0$ for all other components), an additional global residual vector, \mathbf{R}_G , must be introduced, (for the above uniaxial transverse loading, $\mathbf{R}_G = \{\bar{\sigma}_{11}, \bar{\sigma}_{33}, \bar{\sigma}_{23}, \bar{\sigma}_{13}, \bar{\sigma}_{12}\}$), The condition that $\mathbf{R}_G = \mathbf{0}$ should be satisfied together with $\mathbf{R}_{HFGMC} = \mathbf{0}$.

3.4 Calibration and Verification

Figure 32 shows the stress vs. strain relation for the Jute/chopstrand mat material system in tension in the fiber direction. The elastic modulus is taken between 1000-3000 μ strain as discussed in the ASTM D3039 test method.

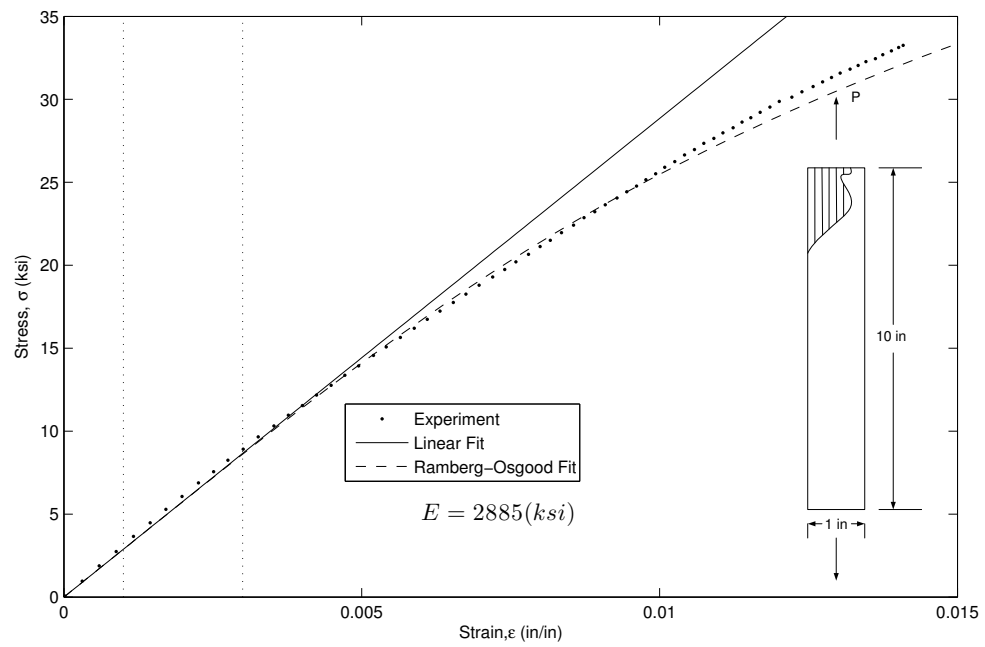


Figure 32: Jute/glass chopstrand mat system as tested in tension in the fiber direction

Figure 33 shows the stress vs. strain relation for the Jute/chopstrand mat material system in compression in the transverse fiber direction. The elastic modulus is taken between $1000\text{-}3000\mu$ strain as discussed in the ASTM D3039 test method.

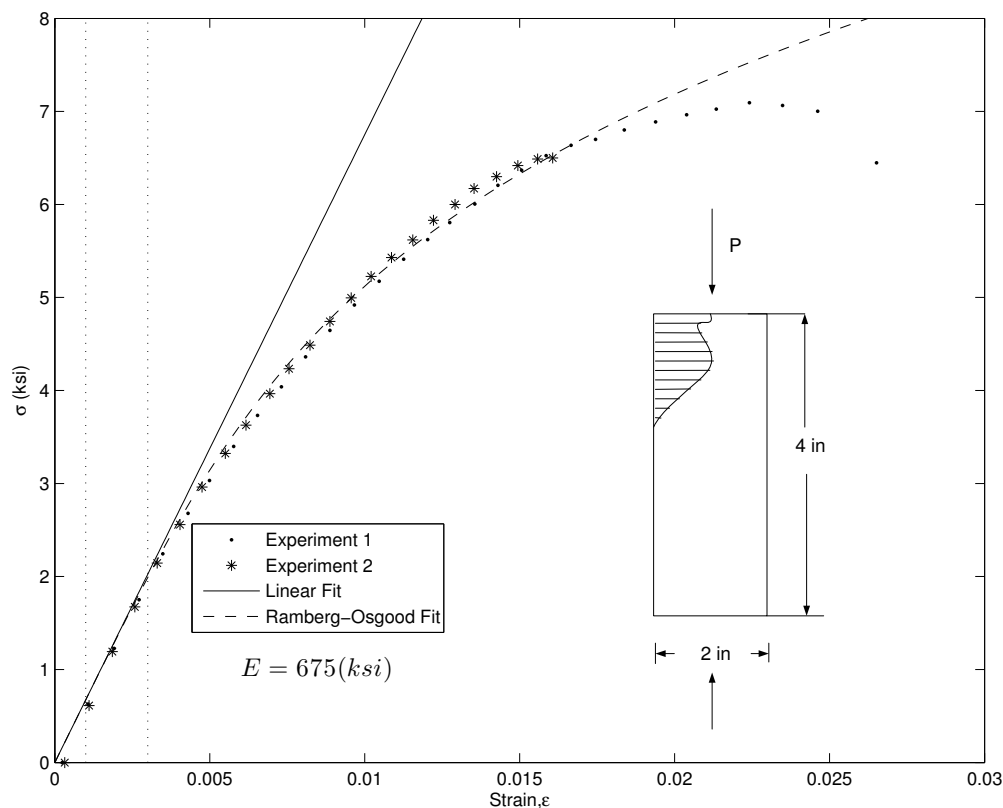


Figure 33: Jute/glass chopstrand mat system as tested in compression in the transverse fiber direction

Figure 35 shows the shear stress vs. shear strain relation for the Jute/chopstrand mat material system as tested in an Iosipescu test fixture. The elastic shear modulus is taken between $1000\text{-}3000\mu$ strain as discussed in the ASTM D5379 test method. Table 2 shows the nominal specimen dimensions.

Figure 34 shows the actual specimen manufactured to the dimensions show in Table 3 and strain gauged as discussed in ASTM D5379.

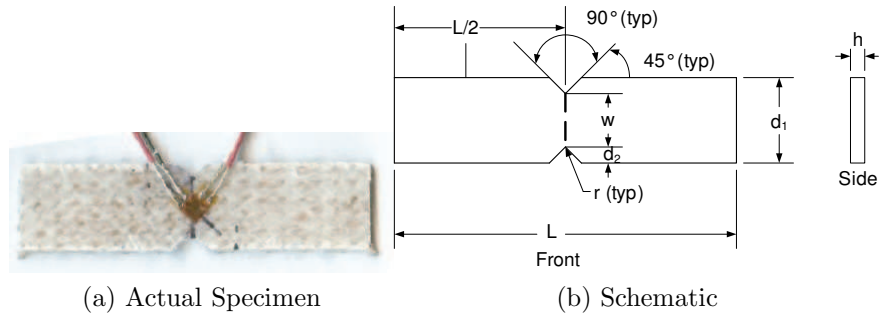


Figure 34: Jute/glass chopstrand mat v-notch specimen as tested with the Iosipescu fixture

Table 3: Nominal V-notch Specimen Dimensions

$d_1 = 20.0 \text{ mm [0.75 in.]}$
$d_2 = 4.0 \text{ mm [0.15 in.]}$
$h = \text{as required}$
$L = 76.0 \text{ mm [3.0 in.]}$
$r = 1.3 \text{ mm [0.05 in.]}$
$w = 12.0 \text{ mm [0.45 in.]}$

The linear and nonlinear shear properties for constituents in the Nine-Cell model were modified from literature by fitting the overall model behavior to the experimental shear data as shown in Figure 35. The ADT and APT models used the mean of the

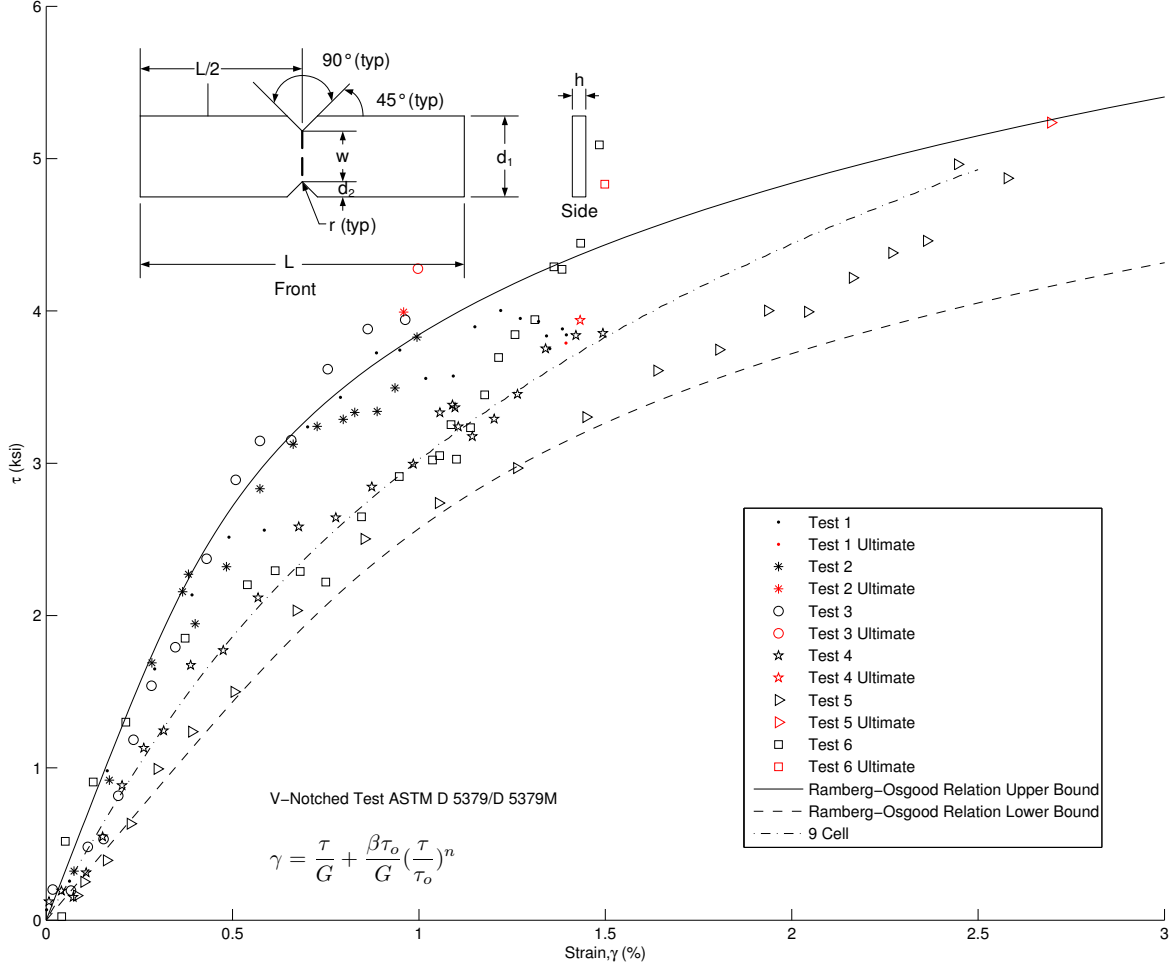


Figure 35: Jute/glass chopstrand mat system as tested in shear with the Iosipescu fixture

The experimentally determined orthotropic elastic materials properties of the Jute/Glass Chopstrand Mat system are shown in table 4.

Table 4: Unidirectional elastic material properties of Jute with chopstrand mat

E_{11} MPa (ksi)	E_{22} MPa (ksi)	G_{12} MPa (ksi)	ν_{12}	Thickness mm (in)
19890 (2885)	4650 (675)	3172 (460)	0.36	2.71 (0.1065)

Fitting the experimental results to the Ramberg-Osgood relations $\epsilon = \frac{\sigma}{E} + \frac{\beta\sigma_0}{E}(\frac{\sigma}{\sigma_0})^n$ results in the calibrated Ramberg-Osgood relations and parameters for Jute/glass chopstrand mat shown in Table 5.

Table 5: Calibrated Ramberg-Osgood Relations and Parameters for Jute / Glass Chopstrand Mat

<i>Modulus</i> MPa (ksi)	σ_0 (ksi)	β	n
$E_{11} = 19890$ (2885)	$\sigma_{0,11} = 345$ (50.)	$\beta_{11} = 1$	$n_{11} = 4.0$
$E_{22} = 4650$ (675)	$\sigma_{0,22} = 48$ (7.)	$\beta_{22} = 1$	$n_{22} = 4.0$
$G_{12} = 4210$ (548)	$\tau_0 = 30.$ (4.3)	$\beta_{12} = 1$	$n_{12} = 5.0$

Table 6: Ultimate material properties of Jute with chopstrand mat

σ_{T11} MPa (ksi)	σ_{C22} MPa (ksi)	K_{TL} $MPa \cdot m^{1/2} (ksi \cdot in^{1/2})$
277 (40.2)	47.0 (6.8)	22.0 (20.)

Table 7 gives the linear orthotropic properties used for the Jute Yarn and E-Glass Chop strand mat material constituents. Overall orthotropy would be satisfied in the RUC with the combination of all constituents in the RUC. Table 8 shows the nonlinear properties used to describe the matrix using Ramberg-Osgood relations.

Table 7: Fiber linear elasetic properties used in the Nine-Cell RUC

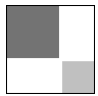



Fiber	E_{11} GPa (ksi)	E_{22} GPa (ksi)	ν_{12}	G_{12} GPa (ksi)	G_{23} GPa (ksi)
Jute Yarn	46.9 (6800)	3.45 (500)	0.11	4.83 (700)	4.83 (700)
E-glass Mat	6.89 (1000)	6.89 (1000)	0.25	5.52 (800)	5.52 (800)

Table 8: Nine-Cell RUC Isotropic Nonlinear Matrix Material Properties (Ramberg-Osgood Relations)

Material	E_{11} GPa (ksi)	ν_{12}	α	S_o MPa (ksi)	η
Matrix	4.14 (600)	0.3	1	27.6 (4)	4

Figure 36 shows a schematic representation of a Repeating Unit Cell used here to show how the Xl and Xh parameters are used to describe the micromechanical geometry. Notice that the subcells are rectangular and 6 parameters are needed for the 3 by 3 geometry. Nine parameters are needed for the material identification of the subcells.

Table 9: Nine-Cell RUC geometry for equivalent constituent volume fractions

System	Geometry	XH 1	XH 2	XH 3	XL 1	XL 2	XL 3
1		1.	0.06	0.6066758	1.	0.06	0.6066758
2		0.076369	1.	0.076369	0.70486	1.	0.70486
3		0.173	1.	0.173	0.53186	1.	0.53186
4		0.184028	1	0.184028	0.515228	1	0.515228

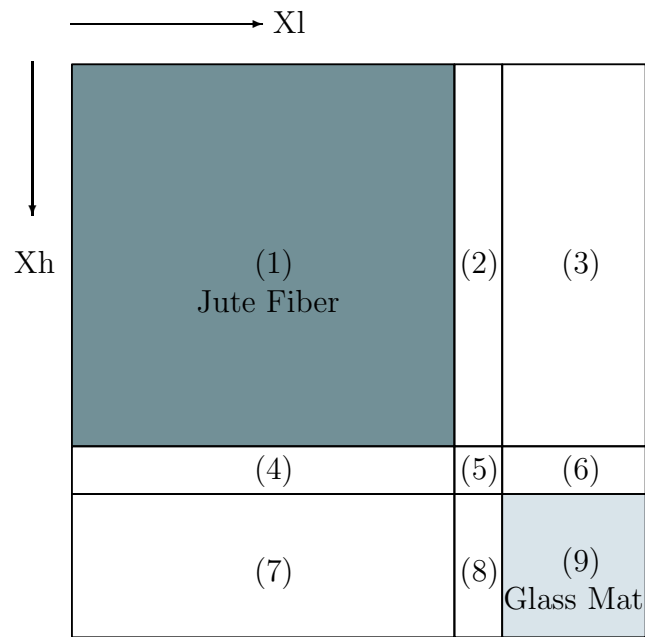



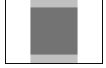
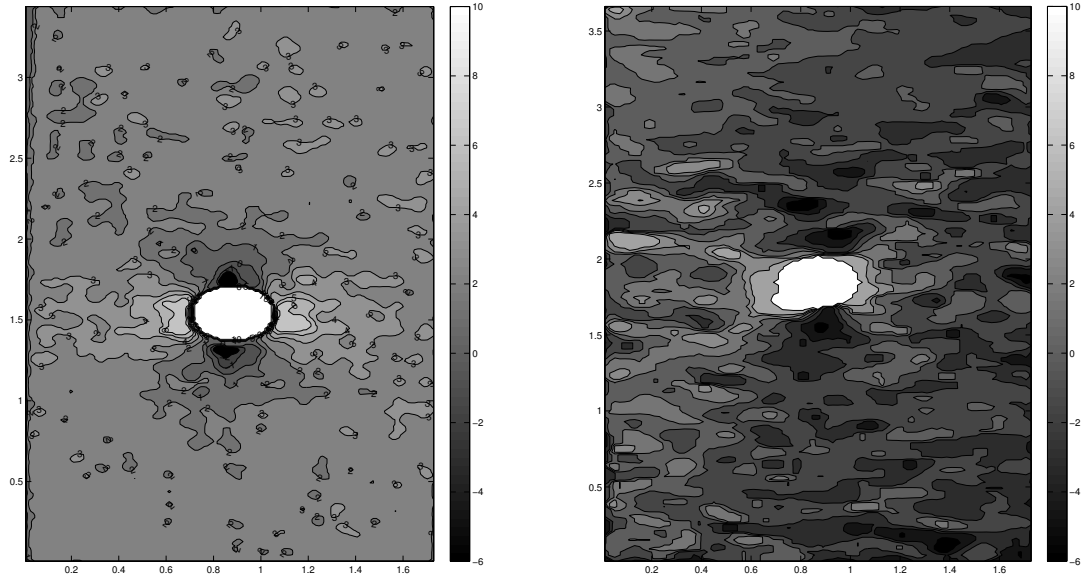


Figure 36: Nine-Cell RUC geometry for System 1

Table 10: Nine-Cell RUC in-plane cell properties for equivalent volume fractions

System	Geometry	E_{11} MPa (ksi)	E_{22} MPa (ksi)	ν_{12}	G_{12} MPa (ksi)
1		19950 (2893)	5390 (782)	0.27	2390 (347)
2		19950 (2893)	5100 (739)	0.25	2520 (366)
3		19930 (2890)	5150 (747)	0.25	2300 (333)
4		19940 (2892)	4960 (720)	0.25	2540 (369)



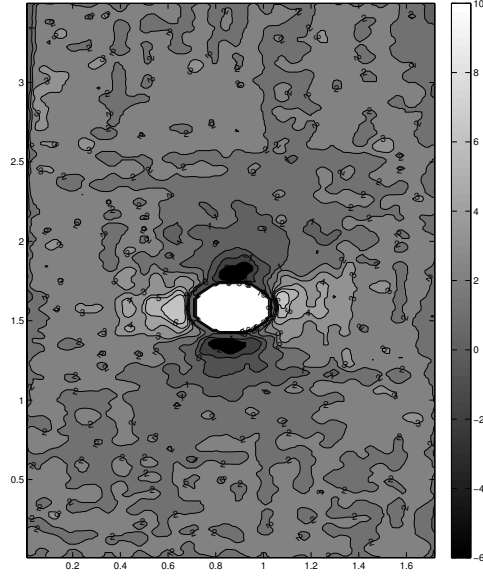
(a) TSA: 1 Hz, ± 200 lb load amplitude

(b) Digital Image Correlation at 400 lb load

Figure 37: Contour map of TSA image scaled to predicted remote axial stress and contour map of calculated axial stress from an optical strain analysis method of an open-hole specimen (Specimen 1) of Jute with chopstrand mat surface layer

Figure 37 shows the same open-hole specimen analyzed experimentally using TSA as shown in Fig. 37.a and with Digital Image Correlation (DIC) as shown in Fig. 37.b. The TSA values are scaled by the remote axial stress and the DIC values are scaled by the axial modulus to simplify correlation with the proposed computational models.

Figure 37 shows the same open-hole specimen analyzed experimentally using TSA as shown in Fig. 37.a. The TSA values are scaled by the remote axial stress to simplify correlation with the proposed computational models.



(a) TSA: 1 Hz, ± 200 lb load amplitude

Figure 38: Contour map of TSA image scaled to predicted remote axial stress and contour map of calculated axial stress from an Digital Image Correlation method of an open-hole specimen (Specimen 2) of Jute with chopstrand mat surface layer

Figure 39 shows the two macromechanical nonlinear orthotropic computational models used in this study.

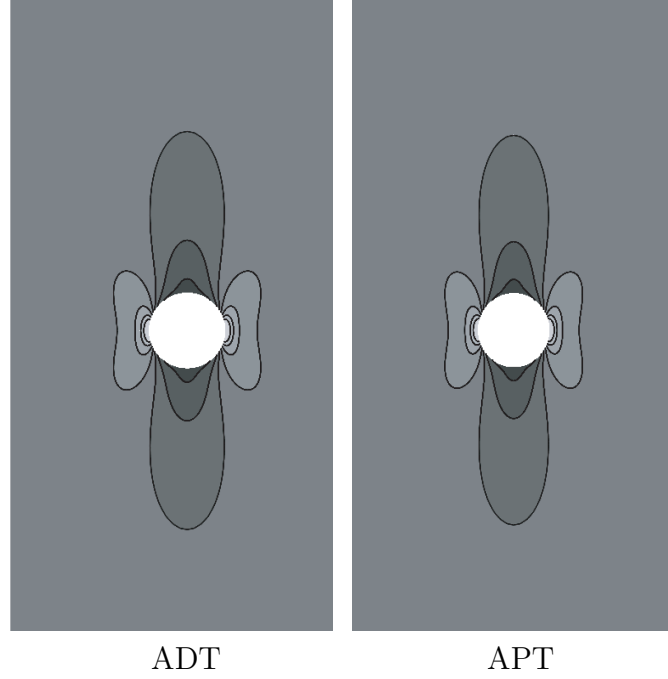


Figure 39: Contour map of predicted remote axial stress of open-hole specimen Jute with chopstrand mat surface layer showing ADT and APT Models

Figure 40 shows a linear orthotropic response compared to the Nine-Cell constitutive model and the two macromechanical nonlinear orthotropic computational models used in this study.

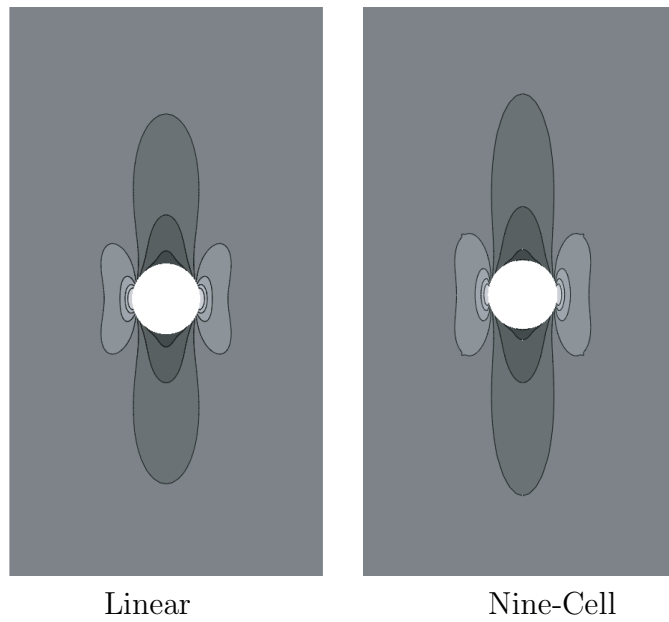


Figure 40: Contour map of predicted remote axial stress of open-hole specimen Jute with chop strand mat surface layer showing Linear and Nine-Cell Models

In addition to the qualitative analysis shown for the multi-axial state of stress modeled in Figures 39 and 40, a line interrogation is shown in Figure 41 to show the prediction capabilities of the Nine-Cell model.

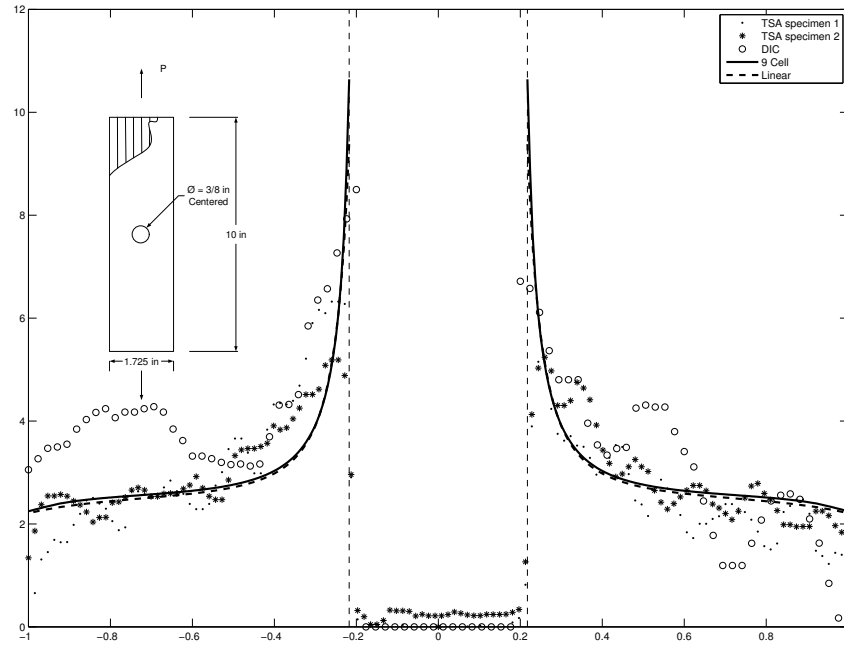


Figure 41: Axial Stress line interrogation on open-hole specimen for 400lb loading on Jute with chop strand mat material system showing the prediction capabilities of the Nine-Cell Model and Linear orthotropic models

The prediction capabilities are shown quantitatively for the Nine-Cell model in Figure 42 using a horizontal line interrogation of the axial stress across the open hole for a 400 lb loading.

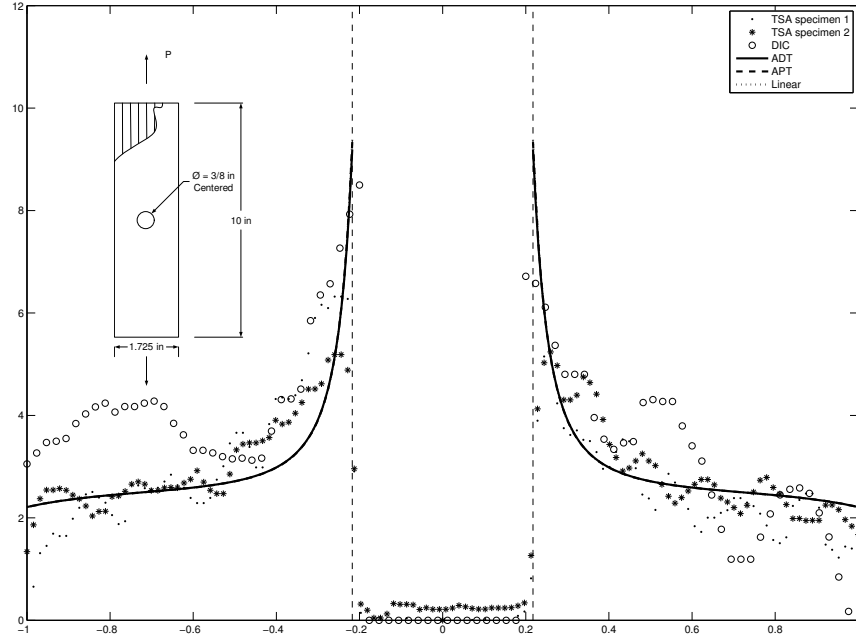


Figure 42: Axial Stress line interrogation on open-hole specimen for 400lb loading on Jute with chop strand mat material system showing the prediction capabilities of the ADT, APT and Linear orthotropic models

In addition to the macro and micromechanical models the Extended finite element fracture modeling framework (XFEM) is applied here to model the pregressive damage in the biocomposite coupons. The XFEM is calibrated using experimentally derived fracture parameters. The energy release rate was calculated from the translaminar fracture toughness tests, and damage initiation principal stresses were taken from the ultimate uni-axial strength values. Linear orthotropic material properties were assigned to the elements. Eccentrically Notched Tension specimens manufactured from Jute/ Glass Chopstrand Mat panels were tested, and the results are shown in Figure 43.

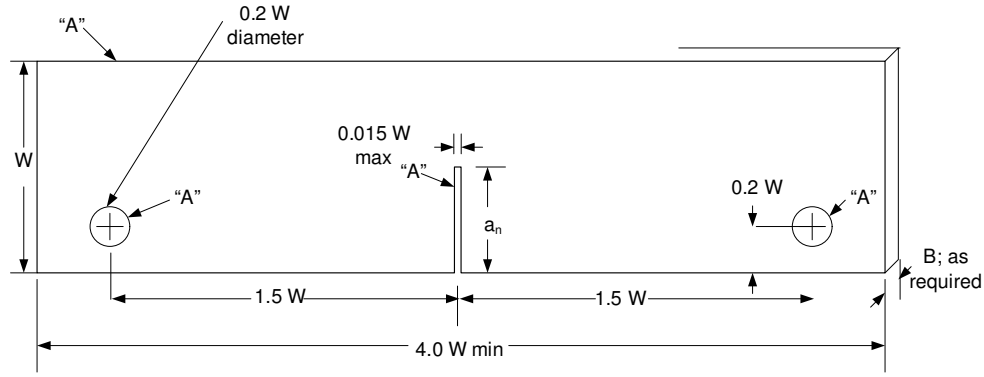


Figure 43: Translaminar Fracture Toughness Test Specimen Schematic

Ultimate properties of the Jute/glass chopstrand mat system are shown in Table 6. To calculate the translaminar fracture toughness ASTM E1922 gives the following equation: $K = \frac{P}{BW^{1/2}} \alpha^{1/2} [1.4 + \alpha] [3.97 - 10.88\alpha + 26.25\alpha^2 - 38.9\alpha^3 + 30.15\alpha^4 - 9.27\alpha^5] / [1 - \alpha]^{3/2}$. Where K = applied stress intensity factor, $\text{MPa } m^{1/2}$, P = applied load, MN , $\alpha = a/W$ (dimensionless), a_n = notch length, m , B = specimen thickness, m , and W = specimen width.

The opening mode energy release rate, G_I , for a crack under plane stress conditions in an orthotropic material is related to the mode-I SIF through relations given by Suo et al. [121]:

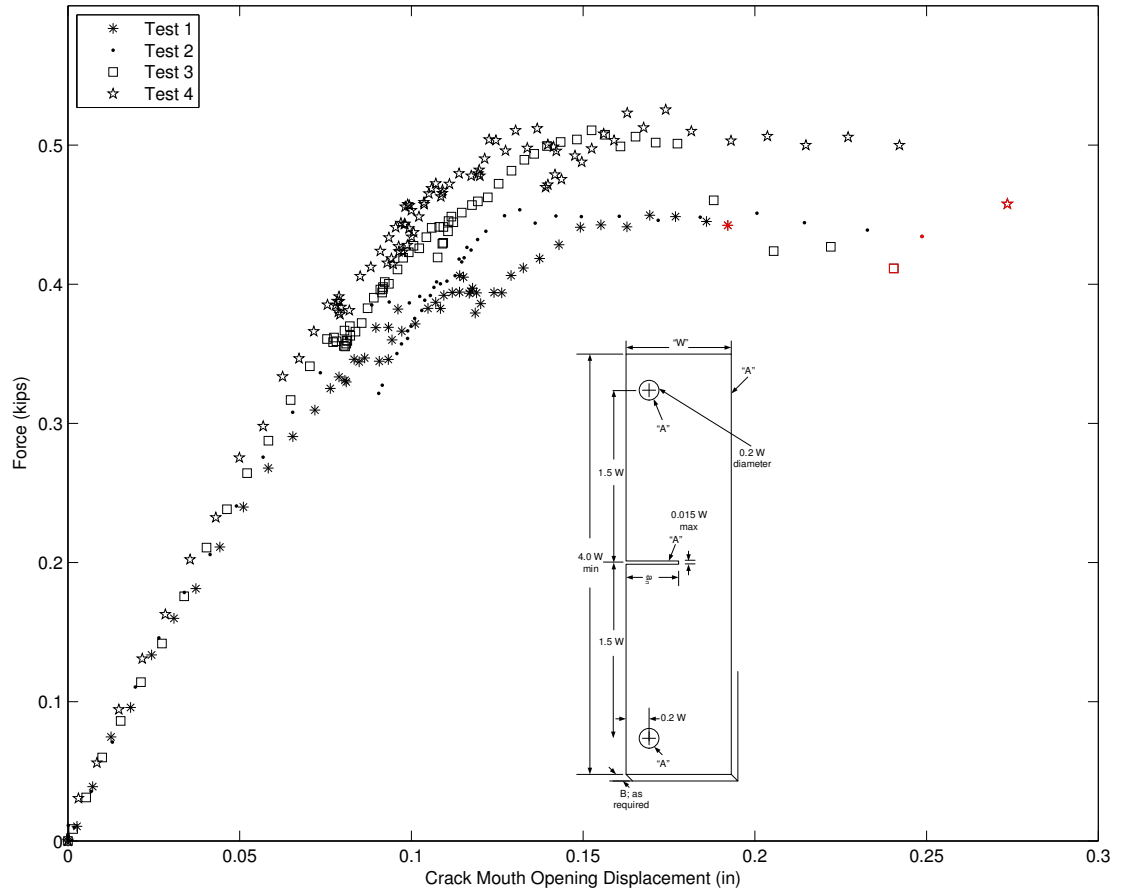


Figure 44: Results of the Translaminar Fracture Toughness Test on Jute/Glass Chop-strand using the Eccentrically Loaded Single Edge Notched Tension Specimen

$$\mathbf{G}_1 = \left(s_{11}s_{22} \frac{1+\rho}{2} \right)^{1/2} \lambda^{-1/4} K_I^2 \quad (170)$$

where s_{ij} are the compliances and the two parameters, q and λ , are measures of the in-plane material orthotropy

$$\lambda = \frac{s_{11}}{s_{22}} = \frac{E_2}{E_1}, \quad \rho = \frac{2s_{12} + s_{66}}{2\sqrt{s_{11}s_{22}}} = \frac{(E_1E_2)^{1/2}}{2G_{12}} - (\nu_{12}\nu_{21})^{1/2} \quad (171)$$

ABAQUS 6.9 allows users to model propagating cracks without prescribing the crack path with the XFEM framework using a version of the superimposed element formulation originally introduced by Hansbo et al. [64]. The method was then incorporated into a traditional FEM framework by Song et al. [117]. At this point the commercially available XFEM framework is limited to linear continuum elements (CPE4, CPS4, C3D4, C3D8) with or without reduced integration. The framework does not allow for crack branching, interacting cracks, multiple cracks within an element, or cracks turning more than 90 degrees within an element.

Figure 45 shows the remote axial stress vs. strain at location 1 (Centered horizontally and 1.63 inches above the open hole). The APT Model shows the greatest nonlinearity, but all of the models are close for the prediction of stress/ strain response at location 1.

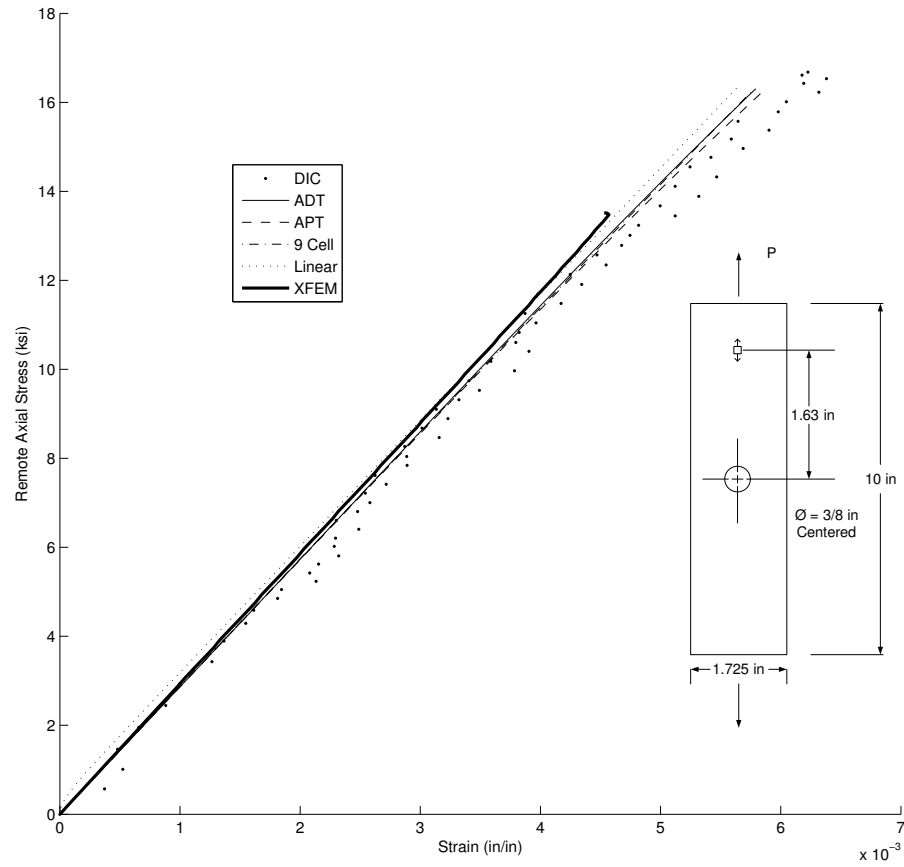


Figure 45: Remote Stress vs. Remote Axial Strain, Image Correlation at Location 1 used for validation of the ADT, APT, Nine-Cell models, Linear, and XFEM orthotropic models

Figure 46 shows the remote axial stress vs. strain at location 2 (Centered vertically and at the edge of the open hole). Again the APT Model shows the greatest nonlinearity, followed by the ADT and Nine-Cell models. The linear model is shown here as a control for comparative purposes.

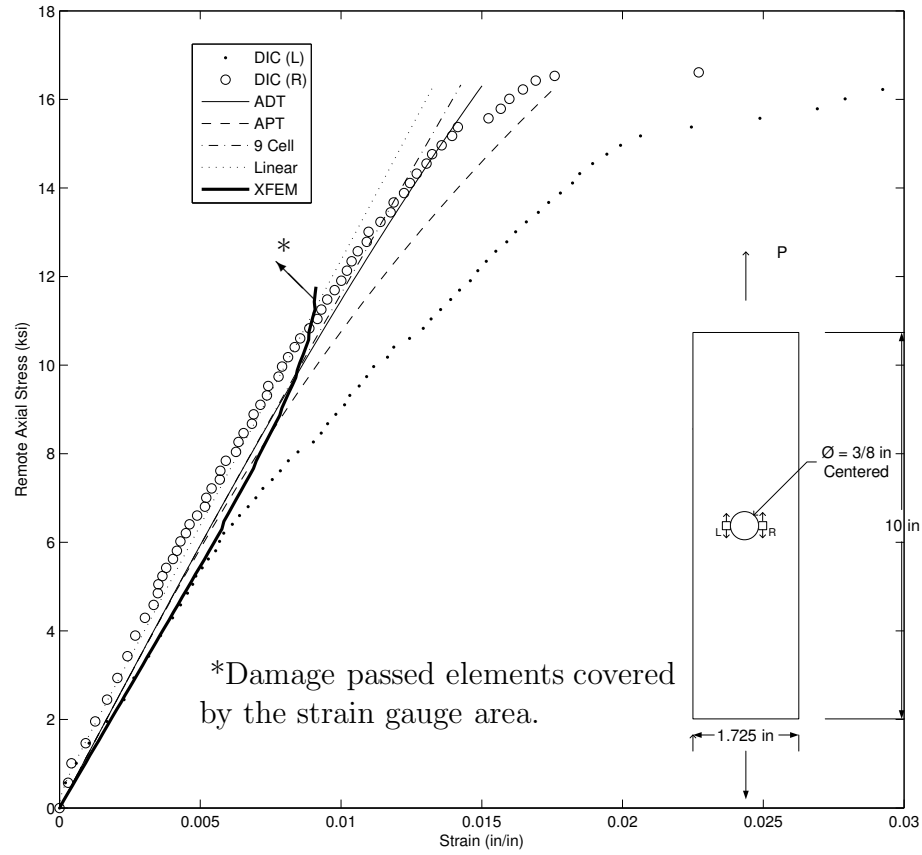


Figure 46: Remote Stress vs. Axial Strain at Open Hole Edge, Image Correlation at Location 2 used for validation of the ADT, APT, Nine-Cell models, Linear, and XFEM orthotropic models

Figure 47 shows the remote axial stress vs. strain at location 3 (Centered vertically and 0.625 inches from the center of the open hole). The ADT model shows the greatest nonlinear behavior followed by the APT and Nine-Cell models. The linear model is shown here as a control for comparative purposes.

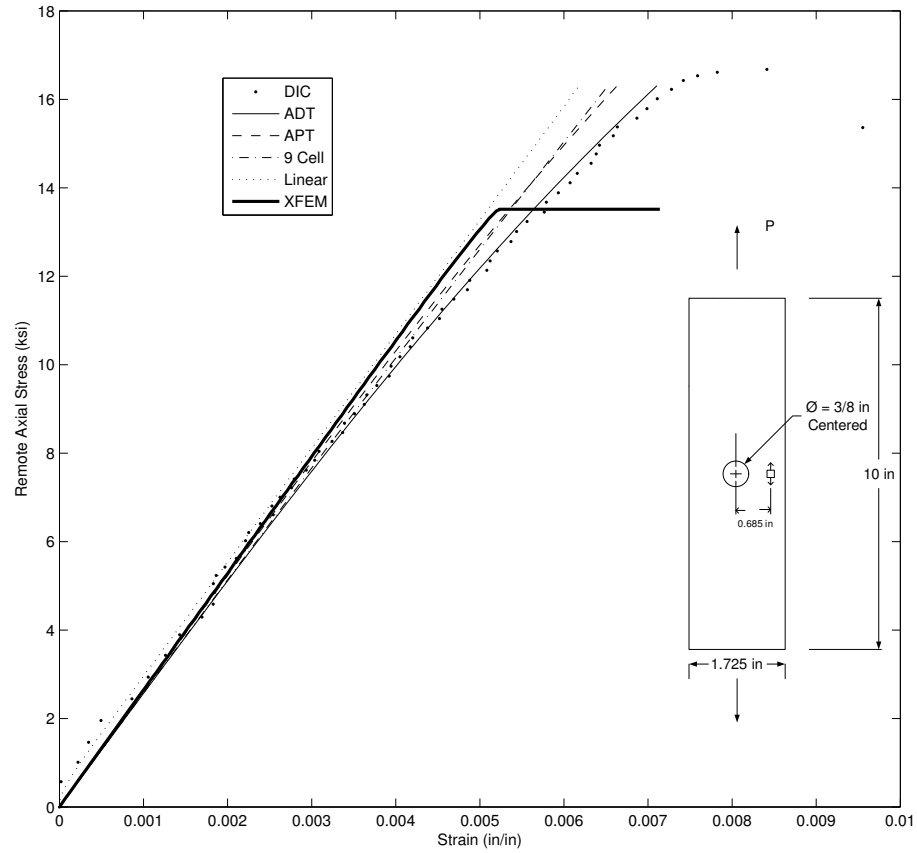


Figure 47: Remote Stress vs. Axial Strain, Digital Image Correlation at Location 3 used for validation of the ADT, APT, Nine-Cell models, Linear, and XFEM orthotropic models

Figure 48 shows the remote axial stress vs. strain across the open hole (3/4 in gauge length extensometer). The ADT model shows the greatest nonlinear behavior followed by the APT and Nine-Cell models. The linear model is shown here as a control for comparative purposes.

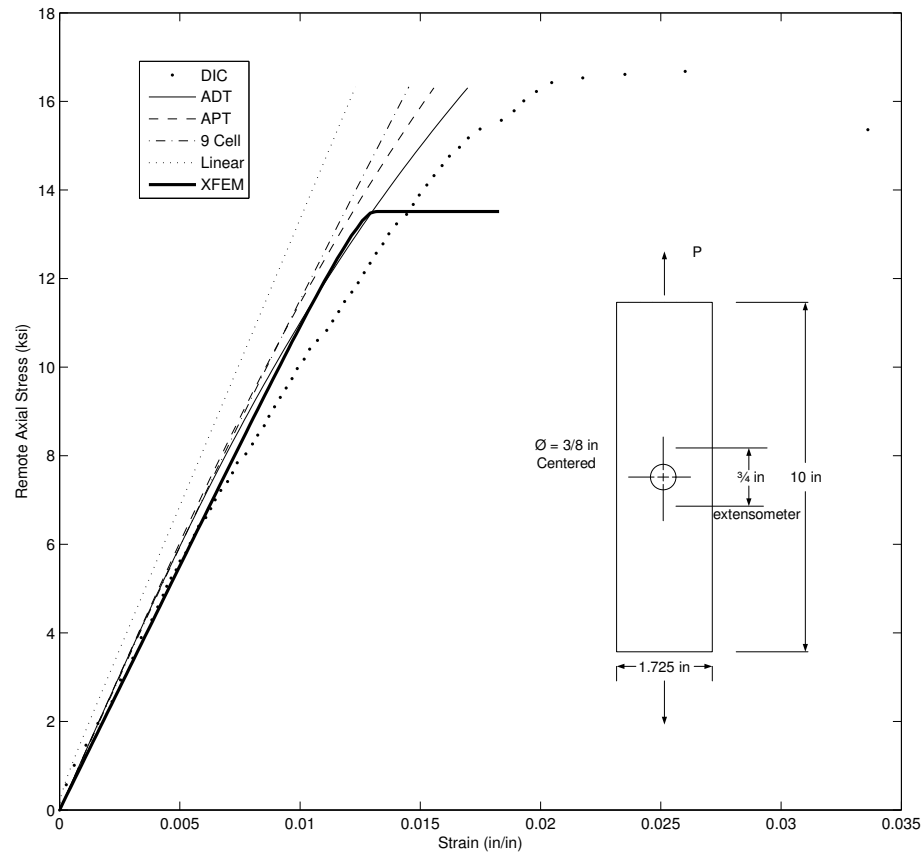


Figure 48: Remote Stress vs. Axial Strain, Digital Strain Analysis using 3/4 inch gauge length extensometer over the open hole used for validation of the ADT, APT, Nine-Cell models, Linear, and XFEM orthotropic models

CHAPTER IV

THERMOELASTIC STRESS ANALYSIS FOR FAILURE INITIATION AND PROGRESSION IN COMPOSITE LAP SHEAR JOINTS

4.1 Introduction

An experimental technique using infrared (IR) thermography is presented to characterize damage initiation and progression in fiber reinforced polymeric (FRP) single lap shear joints. This experimental work formed the basis for a damage initiation investigation on single lap joints in the Master's Thesis by Shane Johnson [73] along with additional experimental work with acoustic emission and clip gauges. The acoustic emission and clip gauge results were taken out, and the TSA results are shown here as a basic explanation of how damage initiates in a static case. This is essential because the work is expanded on for experimental fatigue damage analysis using similar methodology, and the same damage progression is expected for single lap joints. In addition to the experimental work computational fracture models for single lap joints are developed in the next chapter. Two composite lap joint systems are tested. The first consists of carbon-reinforced woven and the second is made of laminated orthotropic plates. The resin layer used for the bonded lap-joints is the FM300K adhesive with an approximate thickness of 10 mils. Thermoelastic Stress Analysis (IR-TSA) is proposed to detect expressions of damage initiation at the surface or the edge of the joint areas. Tests are also conducted with side and direct view IR measurements detecting the crack tip location and progression with increasing applied mean load. Several samples are removed from loading after initial cracking is detected and underwent micrographic inspection to characterize the nature of their

failure initiation. The proposed IR testing schemes indicate a good ability to detect expressions of damage initiation in the glue lines near the edge area. Moreover, crack tip and free surface are also detected as loading progressed, thus IR provides a means of gauging the severity of damage. The demonstrated IR ability to detect initiation and progression in lap joints is well suited for future long-term fatigue tests and can be used to compare the mechanical performance of various FRP joints. This manuscript is divided into three parts. In the first part, the IR-TSA setup is introduced. The second part gives motivation for IR-TSA and introduces two techniques for capturing static damage initiation on lap joints. The third part presents the results of the two IR-TSA methods and the discussion follows.

4.2 Proposed IR-TSA Testing Set-up

The areas of interest for this study and viewing window for IR images are shown in Figure 50. A schematic showing the expected IR image results from the front view is shown in Figure 51. The initial break-up in the adhesive fillet is the initial expected state of damage; failure initiation can be defined as the formation of discontinuities in the external bondline of the single lap shear joint. Photomicroscopy will focus on the areas of discontinuities as detected from infrared thermography to confirm the IR-TSA damage observation. A DeltaTherm DT1500 thermoelasticity measurement system [1] was used to acquire the thermal measurements. This system has an infrared array detector synchronized with the applied cyclical loading in order to measure the transient thermoelastic effect and filter out the IR emissions not associated with the material strain energy releases. The infrared detector acts as a transducer, which converts the incident radiant energy into electrical signals. A lock-in analyzer (a signal-processing unit) extracts the thermoelastic information from the detectors output signal by using the reference signal from the loading device. The TSA-IR system uses the reference signal to reject any non-stress related thermal emissions.

The Delta-Therm has a thermal resolution of approximately 1 mK for image exposure times of one minute or less. Figure 49 shows the testing setup. The IR camera captures images at rates of more than 400 frames per second. The applied load signal is used to integrate synchronized TSA images that correspond to peak values of loading. The integration of the captured images is a temporal smoothing process performed over a specified period. In this study, a period of 1-2 min was used. The cyclic load was applied using an MTS 810servo-hydraulic test system with a 22.2 kN(50 kip) capacity. The accuracy of the recorded strains is within 50 microstrostrains and the load is within 0.22 kN (50lb).



Figure 49: Infrared camera and the IR-TSA experimental setup

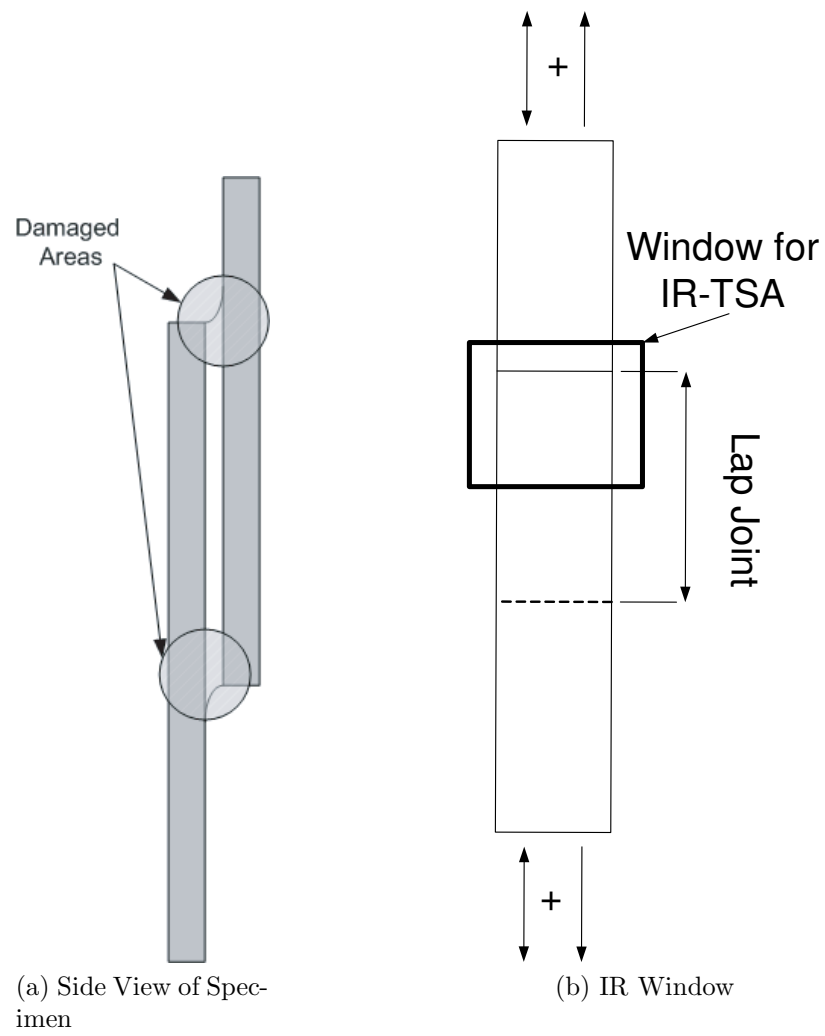


Figure 50: Areas of interest and IR Window

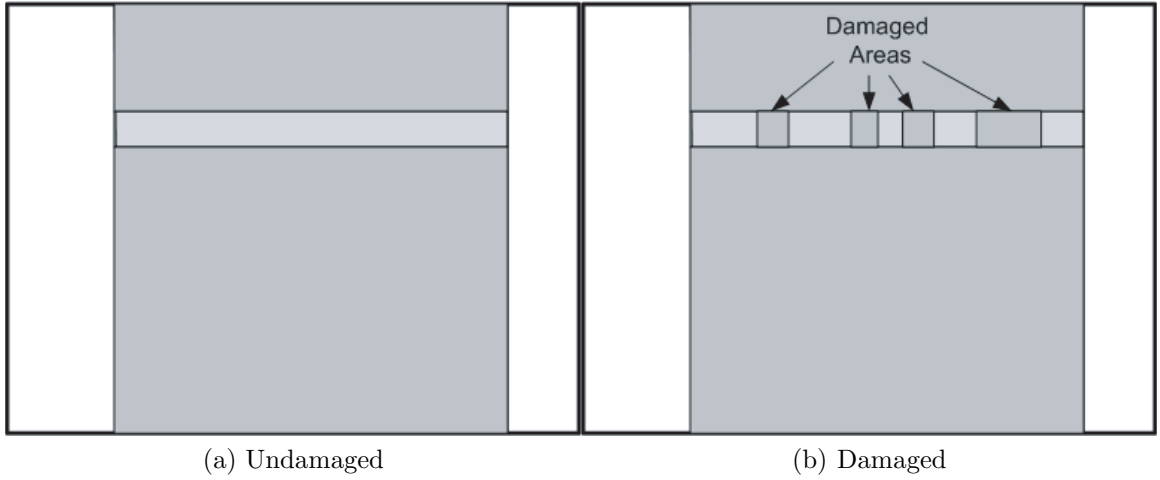


Figure 51: Schematic for Expected IR Front View of Lap Joint

4.3 Proposed IR Testing Approach

Infrared thermography was applied on composite lap-joints to provide a means of measuring temperature changes on the surface due to applied cyclic loading. Two joint types were examined. These include long and short bond geometries made of carbon-reinforced woven and quasi-isotropic laminated parts. The overall goal was to characterize damage evolution with an emphasis on detecting failure initiation. Progression of damage is linked to spatial temperature changes in composite single lap shear joints which prompts the use of an IR-TSA technique. The IR-TSA technique shows promise as a refinement over other testing techniques used in detecting failure initiation and progression in composite single lap shear joints. The motivation of focusing the IR testing for initiation on the bond line can be explained through a FE stress analysis of a typical lap joint. This geometry was modeled in the Abaqus general purpose commercial FE code [2] with 2620 CPE4 plane strain elements. The ends of the specimen are fixed as noticed by the lack of rotation in Figure 53. The properties used in the model are listed in Table 11.

Table 11: Unidirectional material properties of IM7/epoxy composite laminate

E_{11} $GPa(ksi)$	E_{22} $GPa(ksi)$	G_{12} $GPa(ksi)$	ν_{12}	$Ply\ Thickness\ mm(in)$
142.6 (20,700)	8.39 (1220)	3.9 (566)	0.34	.16 (0.0063)

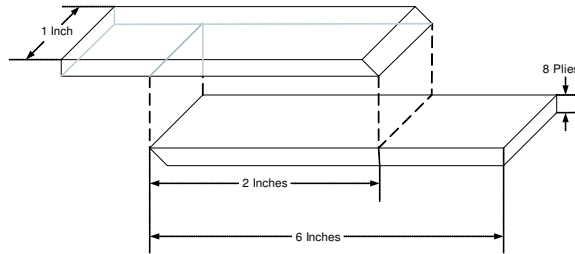


Figure 52: Single Lap Joint specimen geometry made from IM7 Quasi-isotropic laminates



Figure 53: Deformed single lap joint

The FE analysis of a typical IM7/epoxy quasi-isotropic single lap joint (Figure 67) is used to show that the majority of the shear stress in a single lap shear joint is confined to a relatively small region near the external bond line (Figure 54) while the interior bond area is relatively unloaded. There is a stress intensity at the bond edge, and high peel stresses are the main cause of failure initiation at this location in single lap joints. A snapshot of the FE results in the form of peel stresses in this loaded joint as shown in Figure 55 gives insight into the extent of the localized singularity and the bond edge.

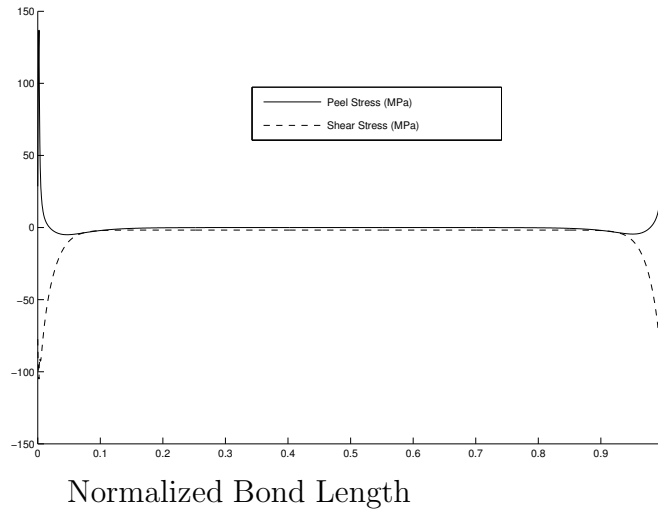


Figure 54: Peel and shear stresses in a typical IM7/Epoxy quasi-isotropic single lap shear joint

Two IR-Thermography testing methods, termed Method-A and Method-B were applied in the proposed experiment to detect damage initiation of the lap shear joints. In Method-A, the load is applied monotonically and paused at select levels for short durations. During this time, a small cyclic incremental load is applied and coupled

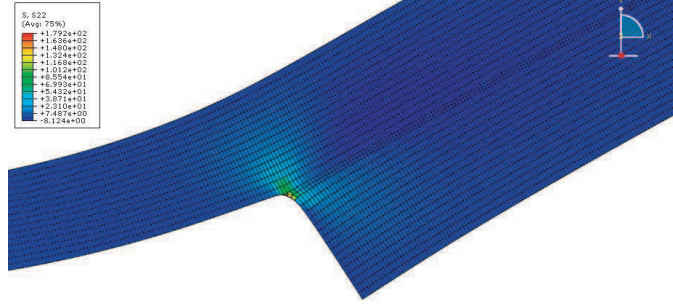


Figure 55: Localized stress intensity at bond edge, FE results showing peel stresses at bond edge on a deformed IM7/Epoxy quasi-isotropic single lap joint

with the IR-TSA measurements (Figure 56). In Method-B, once the applied load has reached a desired level the loading is reversed to a small mean load for a short duration, in which a cyclic load is applied to be coupled with the IR-TSA measurement. The process continued on by increasing load magnitudes followed by applied cyclic loading can be repeated until ultimate failure is reached. Method-A was primarily used for damage progression while Method-B was used to detect initiation. It should be mentioned that the later method was time consuming and can be hard to automate due to the need to process each result to determine that initiation has occurred. The advantage of Method-B lies in its ability to detect damage at an unloaded state, and this method prevents additional damage to the joint due to the added cyclic loading. Failure initiation was defined in this experiment as a stress drop at points on the external edge of the bond.

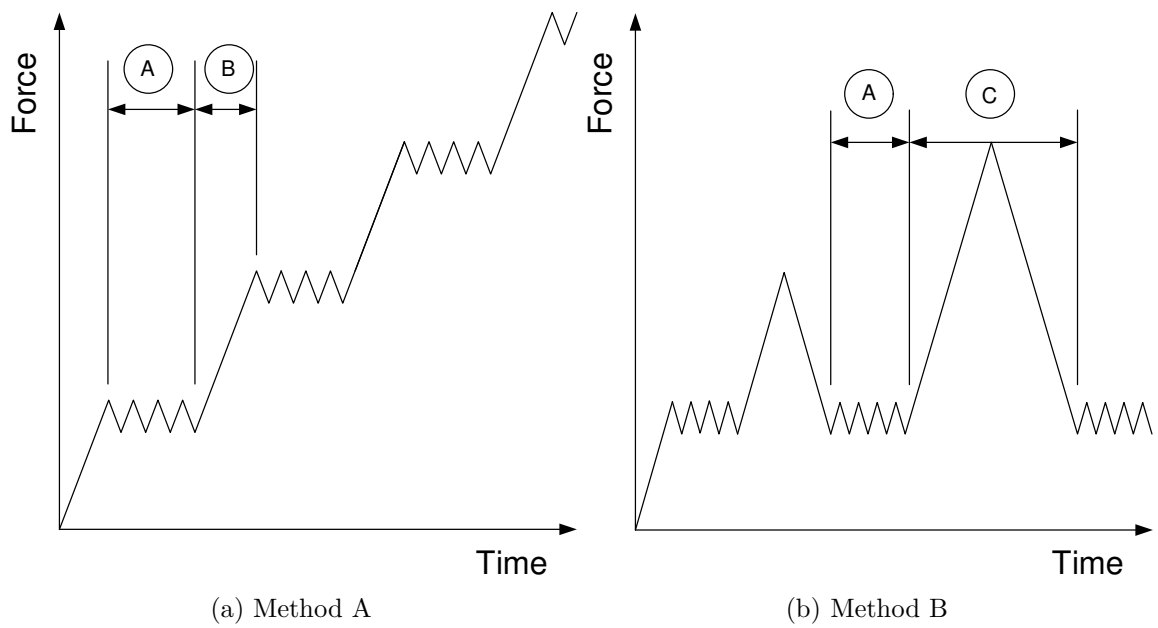


Figure 56: Two proposed IR-TSA Test Methods. Method-A: a static load step is applied, followed by a cyclic loading about this loading level. Method-B: a static load is applied and unloaded followed by cyclic loading at a pre-specified load and cyclic load amplitude. The next applied static load level is increased.

4.4 Results

Representative results are presented to examine the proposed testing methods. Initiation in both Method-A and Method-B is defined as a distinct difference and stress drop in the stress concentration at the bondline. A series of specimens was tested using Method A. Figure 57 shows the measured TSA response to test Method-A with a woven long-bond lap-shear joint. It is interesting to note that the continuous stress concentration in the external bondline present at a mean load of 200 lb and how the IR line is diminished with increased loading up to 4,400 lb. Discontinuities in this continuous line of stress concentration are present in the woven long-bond specimen as early as 1750 lb. The same damage patterns are seen in lap-joints made from uni-tape long bond specimen as shown in Figure 58 also tested with Method-A; however, the crack front is more easily detected by monitoring the side of the uni-tape long bond specimen.

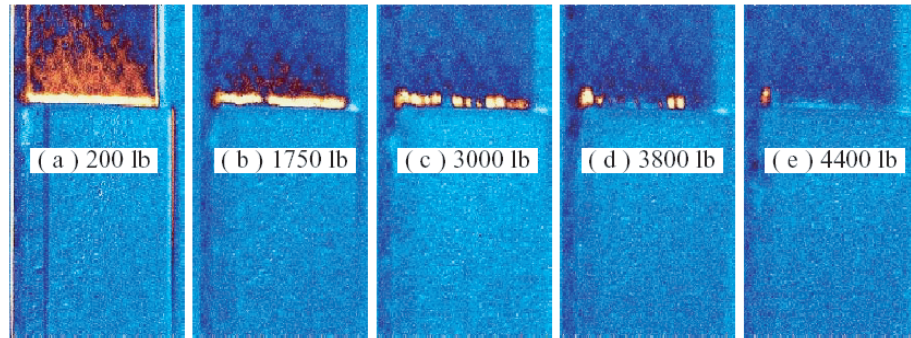


Figure 57: Front and side view of the crack front formation in long-bond single-lap shear joint made with woven plates and tested with Method A, ultimate failure occurs immediately following the 4,450 lb load level. Signature of crack tip is visible from the side view at the 4,400 lb load level.

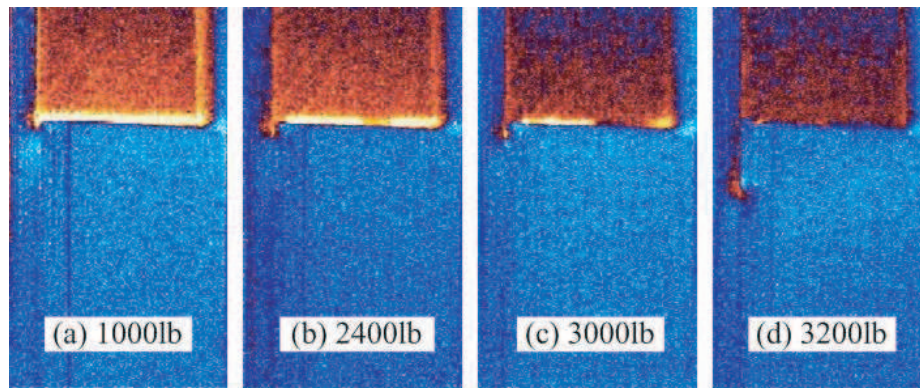


Figure 58: Front and side view of the crack front formation at the bond edge in long-bond single-lap shear joint made from uni-tape plates tested with Method A, ultimate failure occurs immediately following the 3,300 lb load level. Signature of crack tip is visible from the side view at the 3,200 lb load level.

The following series of specimens include short-bond lap joints made of woven and uni-tape plates shown in Figures 59 and 60 were tested using Method-B. The external bond in both cases has initial discontinuities and nonuniformity. This is detected from the early IR-TSA measurements unlike the long-bond case. The continuous stress concentration seen in Figure 57 above is not always the initial case due to slight differences in the manufacturing at the bondline. An attempt was made in each specimen to reach a condition of a discontinuous bondline in order to determine the early stages of crack formation.

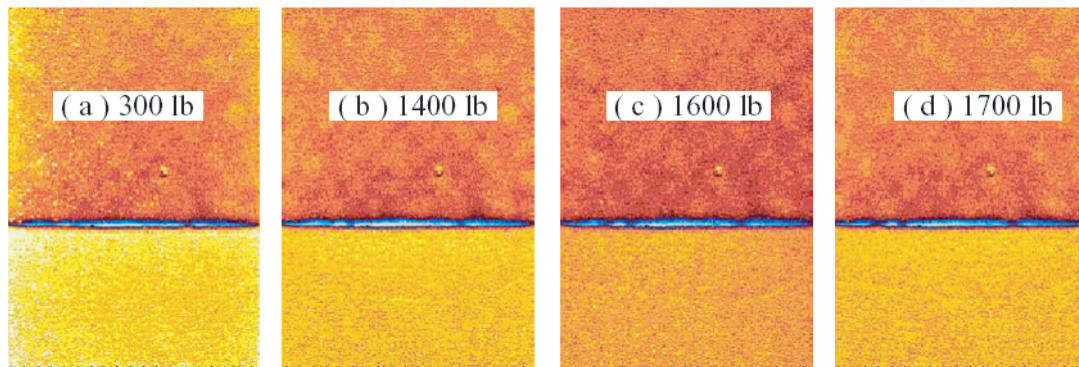


Figure 59: Early stages of crack formation and damage initiation in short-bond single-lap shear joint made from woven plates tested with procedure B preserved after a maximum load level of 1700lb. Noticeable changes in the bond line IR measurement from (c) to (d).

Figure 60 demonstrates the difference between the response of the woven short bond specimen and the uni-tape short bond specimen. The uni-tape short bond specimens emit relatively very little acoustic or thermal responses to loading compared to the other specimen types. Figure 8 shows how failure initiation was captured utilizing TSA.

Several specimens were preserved after noticeable bond line damage initiation has occurred and taken for further investigation using destructive sectioning coupled with photo-microscopy. The major assumption in the proposed testing technique is once a noticeable IR damage detection has occurred in the bond line, damage within the

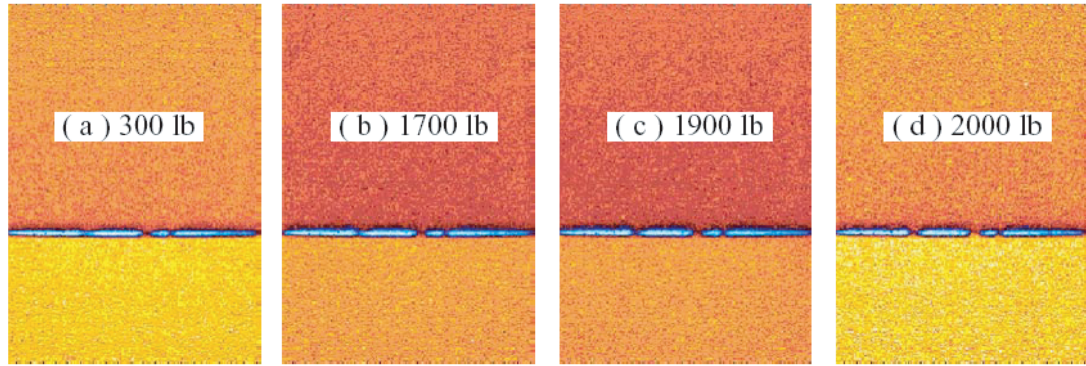


Figure 60: Early stages of crack formation and damage initiation in short-bond single lap-shear joint made with uni-tape plates tested with Method B and preserved after a maximum load level of 2000lb. Increasing changes in bondline IR emission indicating damage progression from (b) to (c) and (c) to (d).

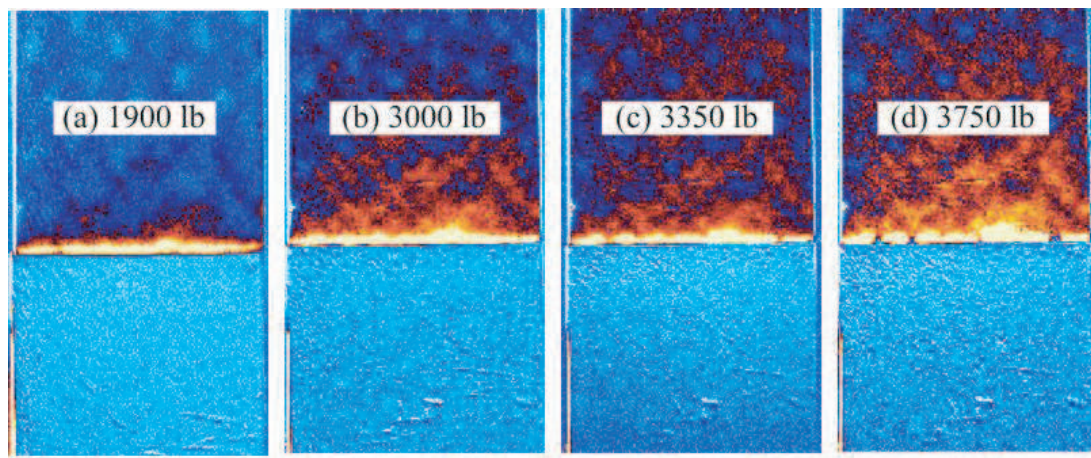


Figure 61: Early stages of crack formation and damage initiation in long-bond single lap shear joint made from woven plates tested with Method B and preserved after a maximum load level of 3750lb. Increasing changes in bondline IR emission indicating damage progression from (b) to (c) and (c) to (d). Noticeable drop in stress concentration from (c) to (d).

joint area should be visually evident. Specimens were removed from testing prior to ultimate failure once thermography, showed that initial failure may have occurred. This allowed for marking of the specimens at the locations where the suspected failure initiation occurred. The objective of the failure analysis was to document, if possible, the nature and extent of this initial damage. Prior to sectioning the specimens for micro graphic inspection, each specimen was ultrasonically inspected for evidence of

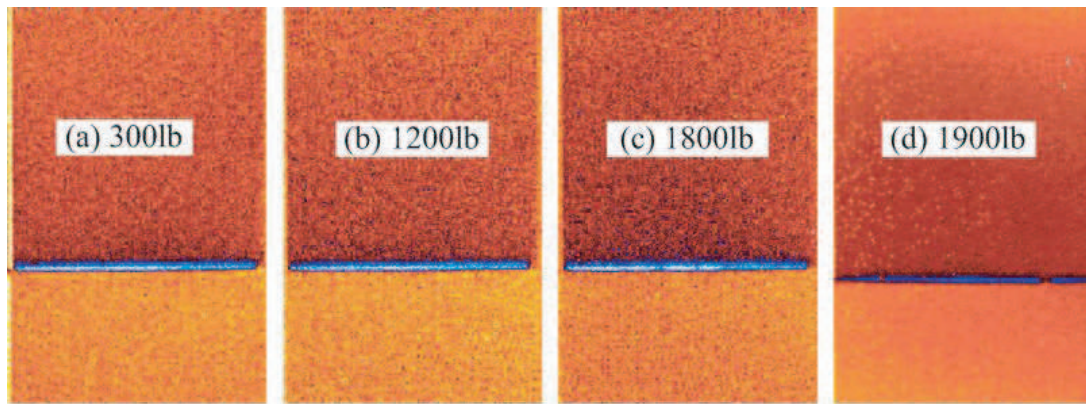


Figure 62: Early stages of crack formation and damage initiation in long-bond single-lap shear joint made from uni-tape plates tested with Method B and preserved after a maximum load level of 1900lb. Increasing changes in bondline IR emission indicating damage progression from (c) to (d). Noticeable drop in stress concentration from (c) to (d).

macroscopic flaws (e.g. delaminations greater than 1/4 diameter). As expected no evidence of this type of damage could be found at the resolution of the C-scan system used. Each specimen was then sectioned and potted in preparation for micrographic inspection. Potted specimens were ground down to points near the marked IR-TSA initiation flaw points using coarse grit paper. At this point specimens were polished down to the flaw points while being checked frequently for indications of cracking. In most cases, evidence of micro-cracking was documented at the sites suspected of failure. Several examples of photos taken at 50X and 200X magnifications are provided. Figure 63 through 64 show several photo-microscope images that correlate well with the above assumption and provide a substantial confirmation to the proposed IR damage initiation and progression method.

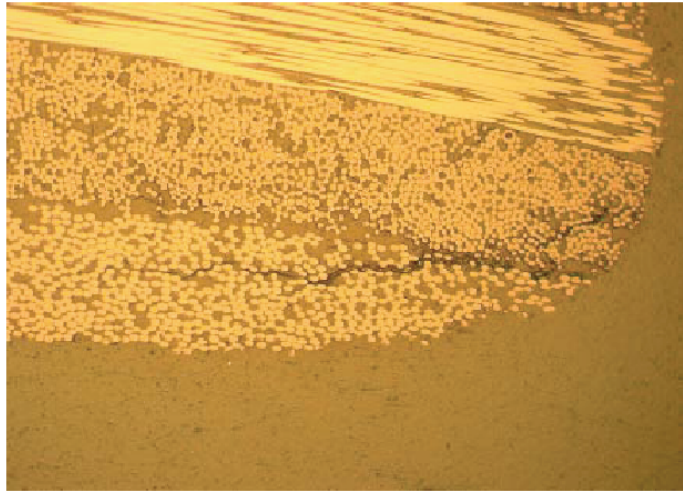


Figure 63: Photograph showing micro-cracking in short bond line fabric specimen #1 (200X) corresponding to IR-TSA measurement in Figure 59.



Figure 64: Photograph showing disbonding at the adhesive interface in short bondline fabric specimen #4 (200X)



Figure 65: Photograph showing micro-cracking in short bond line uni-tape specimen #5 (50X) corresponding to IR-TSA in Figure 60.

CHAPTER V

A STOCHASTIC FATIGUE DAMAGE MODEL FOR COMPOSITE SINGLE LAP SHEAR JOINTS BASED ON MARKOV CHAINS AND THERMOELASTIC STRESS ANALYSIS

5.1 *Introduction*

Quantitative damage detection in composite single lap joints during fatigue is difficult and not practical with many traditional experimental methods. The objective of this study is to build on the existing experimental methods previously used for investigations on static damage initiation by applying stochastic Markov chain methods to model the fatigue damage evolution in composite single lap-joints subjected to cyclic mechanical loadings and monitored in-situ by Thermoelastic Stress Analysis. Thermoelastic stress analysis (TSA) discussed more in detail in the introduction has been used in various fracture and fatigue studies for a quantitative alternative to deformation measurements, and those more relevant to this study are discussed here. Potter et al. [104,105] developed techniques to investigate the thermoelastic effect in laminated composites. Bakis and Reifsnider [13] used laminate analysis and micromechanical formulations to develop predictions of the thermoelastic signal, and good agreement was found between their analytical analysis and experiments, with differences due possibly to material heterogeneity and laminate surface conditions. They also investigated the effect of the cyclic loading frequency on the thermoelastic signal to find spurious non-adiabatic effects above 30 Hz. Dulieu-Barton et al. [42] developed a temperature correction methodology for fiber reinforced polymeric materials and

metals to account for a mean ambient temperature effect during TSA measurements. Their methodology is better able to filter out effects outside of the cyclic loading such as the operator handling the specimen during acquisition or heat flow from the grips to the specimen during cyclic loading. Cavaliere et al. [33, 34] applied TSA techniques to measure crack growth in-situ during fatigue damage while capturing stress fields translated from thermoelastic stress analysis developed to measure stress intensity factors (SIFs) for notched metal matrix composite specimens. Tomlinson and Marsavina [127] and Diaz et al. [39, 40] used Muskhelishvili's solution to calculate SIFs for fracture analysis of metallic materials using TSA techniques providing methods to determine the crack tip location and residual stresses in their study. El-Hajjar and Haj-Ali [48, 63] proposed a TSA calibration technique to quantitatively map the IR signal to the sum of in-plane strains in orthotropic laminate composites, and the experimental results compared well with a finite element analysis of thick section composites with an transversely isotropic surface layer. Emery et al. [50] similarly developed calibration techniques relating the in-plane strains and material properties to predict the thermoelastic signal in orthotropic laminates taking into account the surface characteristics. Haj-Ali et al. [62] also developed IR-TSA methods with and without transversely isotropic surface coatings to measure the sum of normal in-plane strains to show that mixed mode SIFs can be calculated using their method and the Lekhnitski's anisotropic elasticity solution for the stress field ahead of a crack. TSA techniques were applied by Johnson et al. [74] to investigate the fatigue behavior of pultruded materials to obtain an averaged TSA response related to fatigue damage evolution. In their study the compliance showed lower sensitivity under the fatigue loading than TSA measurements. Johnson [73] also tested S2-glass/E733FR open-hole specimens with a $[45/0/45/90]_s$ lay-up sequence to verify that TSA could be related to intermittent compliance measurements and developed

to capture cumulative fatigue data in-situ. A limited number of specimens was examined; therefore, it could not be used to predict fatigue damage evolution. This Markov chain method presented here was developed by Wei et al [132] for analyzing cumulative damage effects in notched laminated composites although similar approaches can be found in the literature [110, 137]. The temperature correction methodology developed by Dulieu-Barton [42] is recommended but was not taken into account in this study because the damage severity in single-lap joints with thin adherends can be determined by TSA by locating the debonding fronts with acceptable accuracy using the algorithms discussed in this paper. The material system in combination with the open-hole specimen geometry chosen for the previous study [132] with open-hole specimens was difficult to analyze due to a host of competing damage mechanisms creating non-adiabatic effects that had to be filtered out by post processing algorithms before the cumulative damage model could be calibrated. The choice of single lap joints allows for a better test of the modeling framework by limiting the analysis to a single damage mechanism, debonding of the joint adherends. This also simplifies the experimental analysis and increases the accuracy of the calibration by limiting the role of non-adiabatic effects in the TSA measurements. Of course, it is impossible to eliminate the influence of irreversible heating arising from frictional effects on the delaminated part, but efficient algorithms are developed in this study for analyzing the joints by decoupling the bonded portion from the delaminated portion where the non-adiabatic effects emanate from through an efficient set of image analysis algorithms. This paper specifically employs TSA techniques and new post processing image analysis algorithms during constant amplitude fatigue for uni-directional S2-glass/E733FR composite lap-joints to define new damage metrics. The TSA signal from the surface of S2-glass/E733FR single lap joints is captured continuously during constant amplitude fatigue loadings. Damage metrics are developed for the composite samples based on developing delamination fronts as evaluated by the thermoelastic

stress analysis (TSA) technique. The TSA damage index at the last fatigue cycle is used to calibrate the Markov chain models (MCMs). Markov chain models are employed with the TSA damage index to predict fatigue behavior for a maximum stress corresponding to 65% and 55% of the ultimate stress. Next, new stochastic S-N curves utilizing the calibrated Markov damage model are also introduced. The damage predictions of the MCMs are then examined at different fatigue cycles. A new method is proposed to construct a predictive stochastic S-N curve utilizing the MCMs for lap joints. The numerical results from the experiments are utilized along with Markov chain theories to predict the fatigue behavior accounting for variability in S2-glass/E733FR lap-joints. The proposed TSA with MCMs is shown to be very effective in predicting the damage evolution and allowed constructing stochastic S-N curves for composite single lap shear joints.

5.2 Testing Setup

A DeltaTherm DT1500 thermoelasticity measurement system [1] was used to acquire the thermal measurements. This system has an infrared array detector synchronized with the applied cyclical loading in order to measure the transient thermoelastic effect and filter out the IR emissions not associated with the material strain energy releases. The infrared detector acts as a transducer, which converts the incident radiant energy into electrical signals. A lock-in analyzer (a signal-processing unit) extracts the thermoelastic information from the detectors output signal by using the reference signal from the loading device. The TSA-IR system uses the reference signal to reject any non-stress related thermal emissions. Figure 66 shows the testing setup. The IR camera captures images at rates of more than 400 frames per second. The applied load signal is used to integrate synchronized TSA images that correspond to peak values of loading. The integration of the captured images is a temporal smoothing process performed over a specified period. In this study, a period of 1

min was used and images are acquired every 3 minutes. TheDeltaTherm was set to a consistent electronic iris of 37%. The cyclic load was applied using an MTS 810servo-hydraulic test system with a 22.2 kN(50 kip) capacity. The accuracy of the recorded strains is within 50 microstrostrains and the load is within 0.22 kN (50lb). Out-of-plane displacements are noticeable due to rotation during fatigue loading because of the relatively high loadings, but in-plane displacements in the bonded area are very small so there was no need for motion compensation.



Figure 66: Fatigue Test Setup for S2-glass/E733FR Single Lap Joints

The proposed IR-TSA technique provides a high resolution full-field thermal map of the surface of a cyclically loaded material developed here to describe fatigue damage evolution in FRP single lap joints. Fatigue damage, such as delamination, matrix cracking, fiber debonding, and fiber breaking, can cause stiffness degradation and spatial stress redistribution on the surface and between the layers. Thus, the thermoelastic signal acquired over the bonded area changes during damage events. Thermoelastic stress analysis of undamaged material relies on reversibility of the load to obtain adiabatic conditions and increase the accuracy by integrating the IR images. However, long integration periods with the lock-in filter will cause an averaging of the TSA signal from damaged areas experiencing friction with the TSA signal from undamaged area experiencing little non-adiabatic effects.. For the case of monitoring fatigue damage using TSA, it is desired to strike a balance between accuracy achieved through long integration periods and obtaining TSA integrated images associated with changing damage states. Integrated TSA images of the specimens were integrated for 1 min and obtained every 3 minutes (900 cycles) during the fatigue loading using an automatic acquisition process in combination with a reference signal to correlate the raw IR detector data to with the cyclically varying load. The infrared camera setup is shown in Figure 1. The fatigue test is stopped when the lap joint separates. The full-field thermal data can then be applied to characterize damage evolution. In this study, fatigue experiments are conducted under two different applied maximum stresses. Four S-2 glass lap-joint laminates are tested under the fatigue loading of 65% of their static ultimate stress. A second series of tests consists of five specimens with same lay-up and geometry is tested under fatigue loadings of 55% of the ultimate stress. The MCMs are used to provide the damage evolution during fatigue for these two sets of experiments. Nine FRP specimens are cut with a diamond abrasive wet saw from monolithic 12 inch by 16 inch unidirectional S2-glass/E733FR thin panels into 1.0 inch by 10 inch coupons (where a 2 inch overlap

is at the mid-length). The joined parts were formed by co-curing, and there is no indication of fiber waviness in the adherends. The panels are manufactured using an autoclave following the pre-preg manufacturers specifications (curing cycles). The lay-up sequence of the specimens is unidirectional and the average (5 repeated tests) measured elastic properties are listed in Table 12.

Table 12: Unidirectional material properties of S2-glass/epoxy composite laminate

E_{11} GPa(ksi)	E_{22} GPa(ksi)	G_{12} GPa(ksi)	ν_{12}	Ply PlyThickness mm(in)
48.4 (7020)	12.5 (1820)	4.51 (655)	0.3	.22 (0.009)

Typical specimen and dimensions are illustrated in Figure 67. The overall testing program including the number of specimens tested at different stress levels is shown in Table 13. The average quasi-static ultimate strength of the single lap joints is 274 MPa or 39.79 ksi. The specimens are sprayed with flat black paint and cyclically loaded in tension-tension load control with a maximum load corresponding to 65% of their ultimate strength. The applied cyclic maximum stress is 178 MPa (25.8 ksi) with a stress ratio of 0.1 and a frequency of 5Hz. The second set of five specimens follows the same test procedure using the 55% ultimate stress.

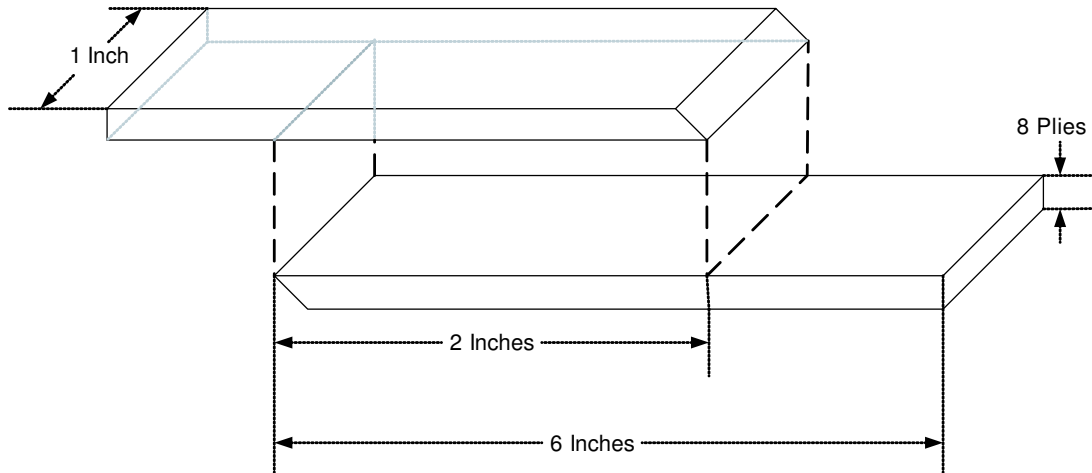


Figure 67: S2-glass/E733FR Single Lap Joint specimen geometry

5.3 Fatigue damage metrics using IR-TSA

One of the major failure modes observed on the surface of the lap-joint is delamination resulting from the stress intensity at the debonding front. The thermal surface field is complicated during damage, especially after delamination because additional thermal excitations are induced by friction and other non-adiabatic effects. To represent the effects of delamination, different metrics may be applied to the TSA data as shown in equation 172. The algorithm for analyzing the TSA images was developed in MATLAB.

$$[TSAx, TSAy] = \text{gradient}(\text{medfilt2}(TSA)) \quad (172)$$

$$TSAy_{front} = (\text{abs}(TSAy) > 100) \quad (173)$$

$$[M, TSAcontiguous] = \text{bwboundaries}(TSAy_{front}) \quad (174)$$

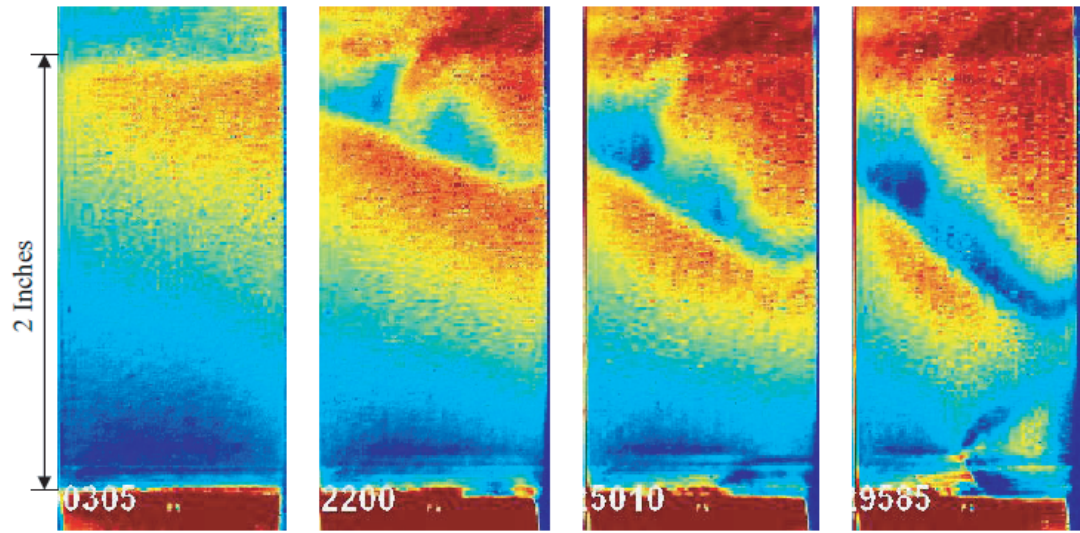
$$TSA_{stats} = \text{regionprops}(TSAcontiguous, 'PixelList') \quad (175)$$

First, the raw data is accumulated in a particular image in the form of in-phase, out-of-phase and resultant data so that an objective autophase algorithm can be performed to account for variation of phase over the field of view. The in-phase TSA image is shown in Figure 4. A median filter is then applied to the in-phase data using a 3 by 3 neighborhood smoothing process to reduce noise while preserving the edges, and a one-dimensional numerical gradient of the data is then applied in both the x and y directions with the default spacing between points of one. Spatial gradients, such as $\frac{\partial TSA}{\partial y}$ (TSAy), can be applied to the image to capture the debonding front ($TSAy_{front}$), and a threshold can be set to filter out areas with low spatial gradients

Table 13: Number of test specimens and applied stresses

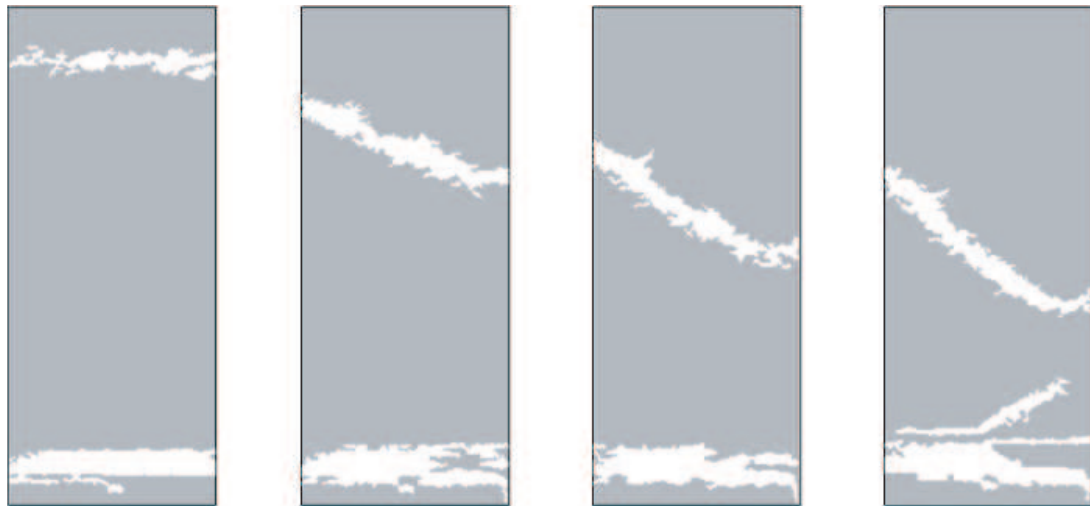
<i>Applied stress level</i>	<i>Number of specimens (ID)</i>	σ_{max} MPa(ksi)	σ_{min} MPa(ksi)
65%	4 (1 to 4)	178 (25.8)	17.8 (2.58)
55%	5 (5 to 9)	150 (21.8)	15 (2.18)

as shown in Figure 69 where y represents the axial axis of the specimen in the loading direction. A matrix of binary values is then acquired through a filtering process that obtains only the high magnitude of values of the one dimensional gradient in the y direction, TSA_y . The gradient threshold of 100 that obviously depends on the application and material system here was chosen arbitrarily, but this threshold value met the requirement of a consistent value that yielded a contiguous region for both the upper and lower debonding fronts regardless of the intensity of the applied loading. The one dimensional gradient in the y direction, TSA_y , is shown in Figure 69. At this point any algorithm can be used to separate the upper debonding front from the lower front for the purpose of calculating damage metrics; however, MATLAB simplifies the process of locating and defining contiguous regions through a combination of the `bwboundaries` and `regionprops` functions. The upper and lower debonding fronts are then separate data sets stored within the variable TSA_{stats} . Of course, the debonding fronts approach each other as the cycles increase, and the specimen never reverts to a previous damage state. Once the debonding fronts are spatially defined, the area between the fronts can be used as a damage metric as shown in Figure 70. The undamaged area $A(N_i)$ is used to define the damage metric (variable), where N_i is the fatigue cycle. For comparison with more simple algorithms, the shortest distance between the debonding fronts can also be taken as a metric for damage as shown in Figure 71.



(a.) 300 Cycles (b.) 12,200 Cycles (c.) 25,000 Cycles (d.) 29,600 Cycles

Figure 68: Typical evolution of maximum IR-TSA spatial gradients for increasing fatigue cycles



(a.) 300 Cycles (b.) 12,200 Cycles (c.) 25,000 Cycles (d.) 29,600 Cycles

Figure 69: Typical evolution of maximum IR-TSA spatial gradients for increasing fatigue cycles

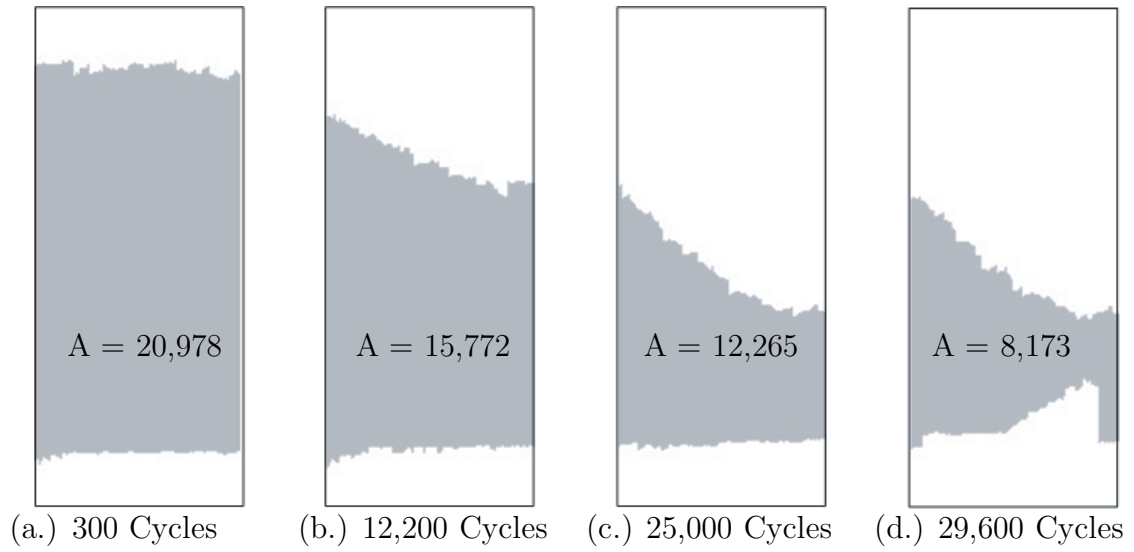


Figure 70: Area measures to evaluate the typical damage evolution as defined by differential IR-TSA under increasing fatigue cycles

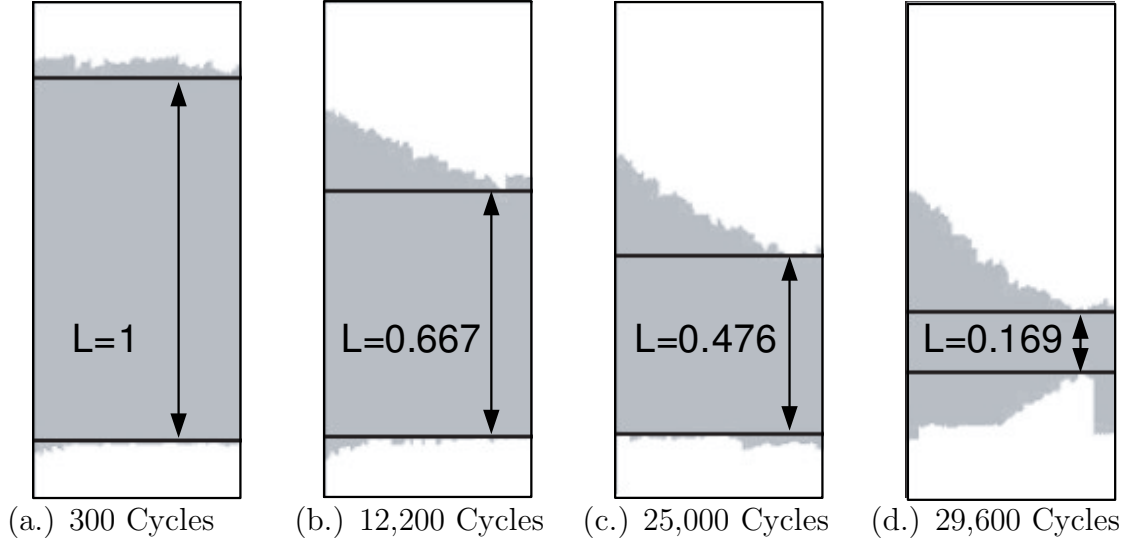


Figure 71: Normalized effective bond length measures to evaluate the typical damage evolution as detected by IR-TSA under increasing fatigue cycles

The damage metric is related to the undamaged/healthy region (gray area in Fig. 70). The latter can be utilized to define the TSA area damage index. The shear lap region is initially undamaged, and the healthy region decreases as the fatigue cycle increases. When the decreasing healthy area cannot take the applied stresses, the lap-joint specimen reaches final fracture. Therefore, the TSA area damage index can be expressed by:

$$D^{(area)}(N_i) = 1 - \frac{A(N_i)}{A(N_0)} \quad (176)$$

where N_i is fatigue cycle, and $A(N_i)$ is the undamaged area at a given fatigue cycle, N_i .

Similarly, a different damage index utilizing the difference of debonding fronts can be defined. The top and bottom debonding fronts, shown in Fig. 71, approach each other from the edges of the lap joint. The shortest distance between the debonding fronts decreases due to the fatigue process. The damage index for the difference of debonding fronts can be defined as:

$$D^{(diff)}(N_i) = 1 - \frac{L(N_i)}{L(N_0)} \quad (177)$$

where $L(N_i)$ is the shortest distance between debonding fronts at a given fatigue cycle, N_i . It is interesting to note that the damage indices, $D(\text{area})$ and $D(\text{diff})$, are not necessarily one when the specimens fracture, especially for specimens subjected to higher stress levels. This is because the final fracture occurs within a TSA integration interval, and the TSA method can only capture the last image with the small remaining undamaged area. However, this dramatic fracture is expected within 900 fatigue cycles maximum (integration interval used in this study). The image more close to the final failure can be achieved by shortening the integration time if needed. Similar trends are shown in the damage indices of area and length based metrics and the process is irreversible. Thus, the damage evolution metric of the specimens can be used with the Markov chain theory, and their fatigue behaviors can then be stochastically constructed.

5.4 A cumulative damage model using Markov chain theory

This section introduces a stochastic cumulative damage (CD) method to describe fatigue damage progression. Previously developed IR-TSA test methods [132] by the authors have been used in this study. The work of Wei [131] and Rowatt [109] provide a more thorough review of the Markov Chain Method for cumulative fatigue. The Markov chain consists of a probability transition matrix (PTM) and distribution. Let π_0 be a row vector representing a damage distribution at different damage states for the Markov chain. The initial damage distribution, $\{1, 0, \dots, 0\}$, can be expressed as where all samples are at their undamaged state. The distribution at step n can be expressed as:

This section introduces a stochastic cumulative damage (CD) method to describe fatigue damage progression. Previously developed TSA test methods [132] by the

authors have been used in this study. The Markov chain consists of a probability transition matrix (PTM) and distribution. Let be a row vector representing an assumed initial distribution for the Markov chain. The distribution at step n can be expressed as:

$$\pi_n = \pi_0 P^n \quad (178)$$

where the P is the PTM. For a CD model, the PTM with b+1 damage states can be express as:

$$P = \begin{bmatrix} p_0 & q_0 & 0 & 0 & 0 \\ 0 & p_1 & q_1 & 0 & 0 \\ 0 & 0 & \ddots & \ddots & 0 \\ 0 & 0 & 0 & p_{b-1} & q_{b-1} \\ 0 & 0 & 0 & 0 & 1 \end{bmatrix}, \quad (179)$$

where the p's and q's are conditional probabilities that determine if the current damage state remains or proceeds to the next state, respectively. If the PTM is constant through the entire damage process, then the process is termed stationary. The probability for the first damage state to proceed at the y-th trial is given by:

$$f(y) = p^{y-1}q \quad (180)$$

which is a geometric distribution. Therefore, the p and q variables can be obtained from:

$$r = \frac{VAR}{EX} = \frac{p}{q}; p + q = 1 \quad (181)$$

where EX and VAR are expected value and variance of the geometric distribution, respectively.

Up to this point, the Markov theory for stochastic processes has been introduced, and therefore, the fatigue damage evolution through cycles can be constructed once the required parameters in the Markov chain are calibrated from experiments. The variance and mean value of the fatigue cycles for a specific damage state or index (e.g., failure when the damage index equals one) can be defined. Then, the Markov chain model shown in Eq. (178) can be constructed and used for describing the fatigue damage evolution.

5.5 TSA results and Stochastic S-N curves

Figures 72 and 73 show the TSA undamaged area and debonding difference damage index for the specimens subjected to 65% and 55% stress levels, respectively. Similar trends are shown in the damage indices of area and length based metrics. Figure 72 shows how the TSA Damage Indices progress towards failure, and the data is bounded by the Markov Chain Model as described in the previous section. The data for specimen 4 in the 65% stress level was taken out of Figure 72 because failure occurs in over 2×10^4 cycles, and it is more critical to predict a lower bound on the data.

Table 14 shows the Markov Chain parameters required to calibrate the models in Figure 72 and 73.

Table 14: Number of test specimens and applied stresses

<i>Applied stress level</i>	<i>#Damage States</i>	<i>P</i>	<i>Q</i>
55%	6	0.0001818	0.9998182
65%	6	0.0006246	0.9993754

One of the advantages of the proposed TSA method is that the fatigue process can be monitored continuously without any interruption due to taking the measurements. Therefore, it is possible to show through an S-N curve progression how the average

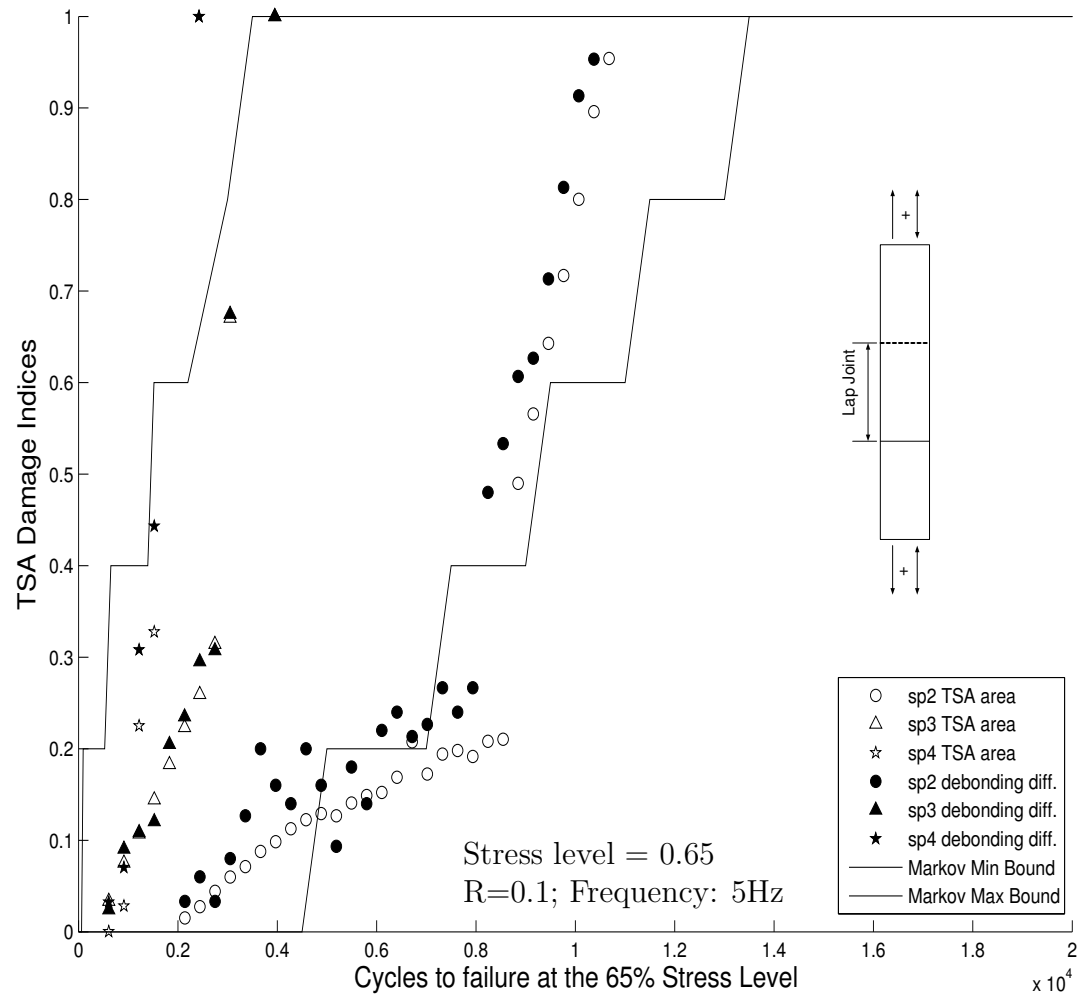


Figure 72: Fatigue damage indices of shear lap joints subjected to stress level of 0.65

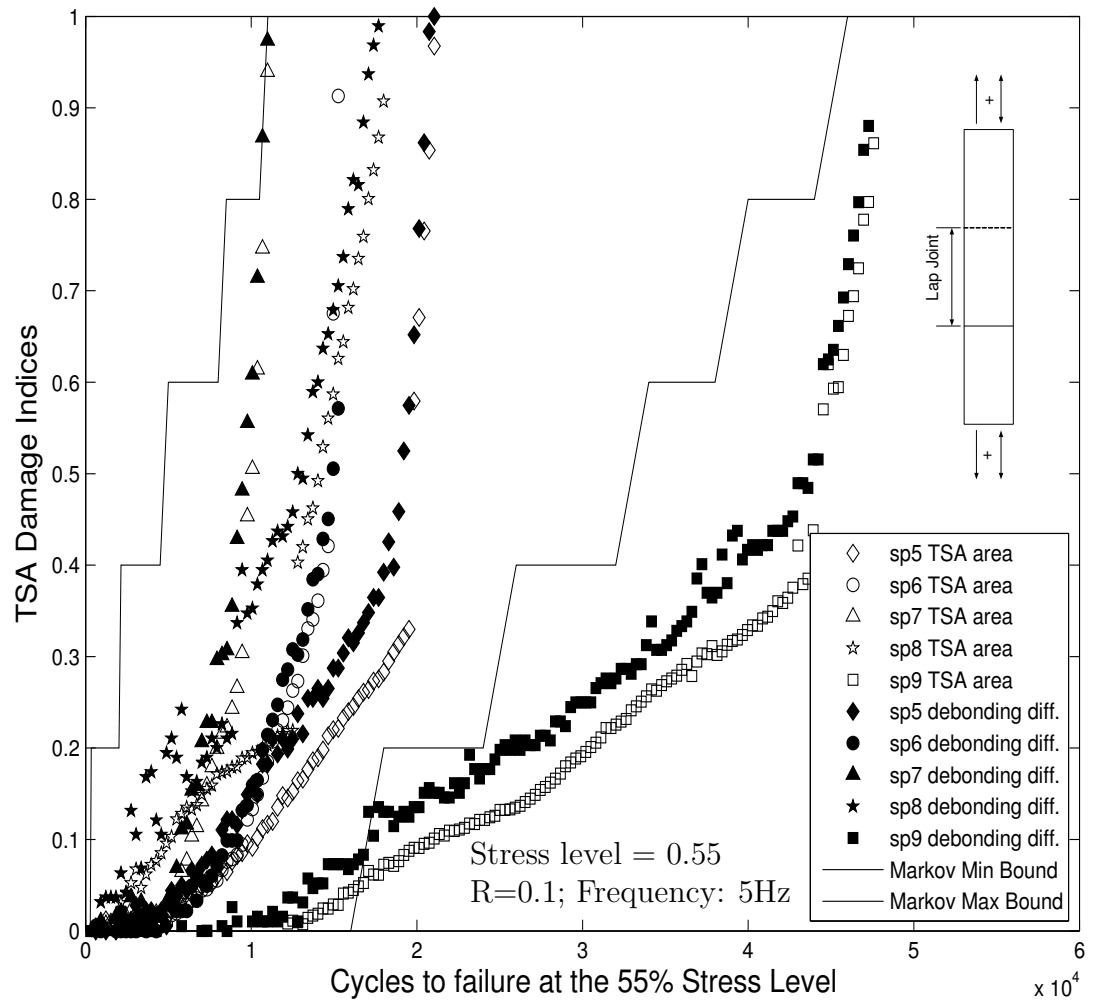


Figure 73: Fatigue damage indices of shear lap joints subjected to stress level of 0.55

specimen progresses through fatigue cycles from one damage state to the next at various stress levels. The S-N curves are constructed based on the two different tested stress levels. The Minimum Markov Chain Bounds in Figure 11 indicate at the stress levels tested where 20% delamination, 40% delamination, and failure as predicted with the model. Also shown in the figure is the average experimental data for the area TSA data to show the difference between the prediction and the average measured case. They are fitted to go through the mean cycles to failure of the specimens subjected to two stress levels. The average shear stress is simply the ratio of remote force and the area of overlap region. Three different damage indices, 0.4, 0.2, and 0.1, are also selected to generate the progression of S-N curves. The S-N curves with larger damage indices are expected to have larger fatigue cycles. The fatigue cycles for the 55% stress level show relatively less shifting in logarithmic scale. Therefore, the S-N curves exhibit the progression in slope as well.

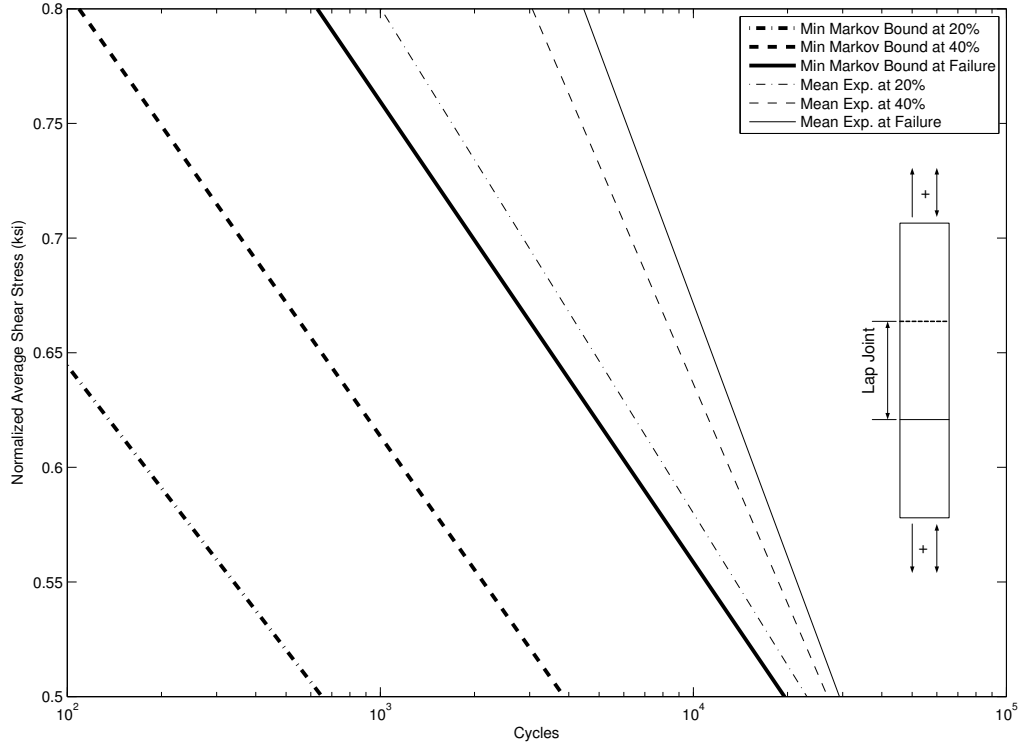


Figure 74: S-N curve progression for damage index of TSA area

Stochastic S-N curves of the limited number of tested specimens can be constructed utilizing Markov chain theory. Figure 76 illustrates the iterative algorithm sweeping the entire fatigue cycles to obtain the stochastic S-N curves. We first calibrate the number of damage states, $b+1$ used in Eq. 179, of the specimens subjected to the same applied stress level. The mean and variance of the cycles to failure are applied in Eq. 181, and then the number of damage states in the PTM can be determined by the convergence of the mean cycles to failure from Markov chain prediction and from tested data. This calibrated number of damage states is used with a mean cycles to failure function in the MCM. The mean cycles to failure function is a logarithmic function which goes through the mean cycles to failure of the two sets of specimens of two stress levels. A trial variance, $Var^{(tr)}$, is used in the calibrated MCM to obtain the output mean cycles to failure, $N_f^{MCM(AVG)}$. If the output mean cycles

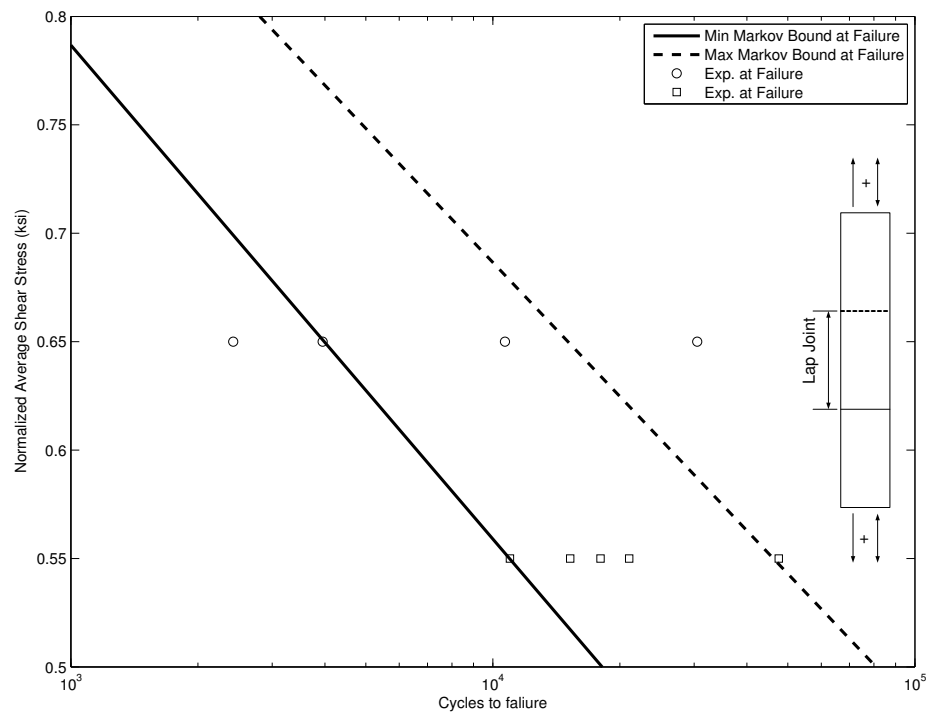


Figure 75: Constructed stochastic SN data based on two limited data sets and previously calibrated MCM

to failure, $N_f^{MCM(AVG)}$ does not converges to the input mean cycles to failure, N_f , of the current fatigue cycle. The algorithm iterates by increasing the previous trial variance, $Var^{(tr)}$, by a small increment, ΔVAR , and then repeat the iteration until the mean cycles to failure, $N_f^{MCM(AVG)}$ converges. Once the iteration has converged, the trial variance, $Var(tr)$, is calculated based on the previously converged variance. The procedure is executed through the entire fatigue cycles in order to obtain the variance or the distribution of the cycles to failure at a different stress level with no tested data. Therefore, the complete stochastic S-N curve of the tested material is obtained. The proposed stochastic algorithm for the construction of S-N curves is discussed in Steps 1-3 in Figure 76, and a schematic representation is shown in Figure 77.

Step 1. Initialize variables

INITIALIZE $N_f^{(0)}, \Delta N_f, VAR^{(0,0)}, \Delta VAR, \Delta X$ —duty cycle, $j = 0$,
 $i_{max} = N_f^{(final)} / \Delta N_f$

Step 2. Find convergent MCM variance for each i-step

LOOP $i = 1, 2, 3, \dots, i_{max}$

$N_f^{(i)} = N_f^{(i-1)} + \Delta N_f$

$VAR^{(i,j)} = VAR^{(i-1,j)}$

Step 3. j-iterations for variance within current i-step

$j = j + 1$

$VAR^{(i,j)} = VAR^{(i,j-1)} + \Delta VAR$

CALCULATE p, q USING Eq. 1

INITIALIZE X

$m_f = \text{Integer}(N_f^{(i)} / \Delta X)$

LOOP $m = 1, 2, 3, \dots, m_f$

$X = X + \Delta X$

$\pi_X^{(m)} = \pi_0 P^X$

CALCULATE $N_f^{MCM(AVG)}, N_f^{MCM(MAX)}, N_f^{MCM(MIN)}$

IF $|N_f^{MCM(AVG)} - N_f^{(i)}| > TOL$, THEN GOTO Step 3

ELSE GOTO Step 2

Figure 76: Proposed algorithm for generating stochastic S-N curves using previously calibrated MCMs.

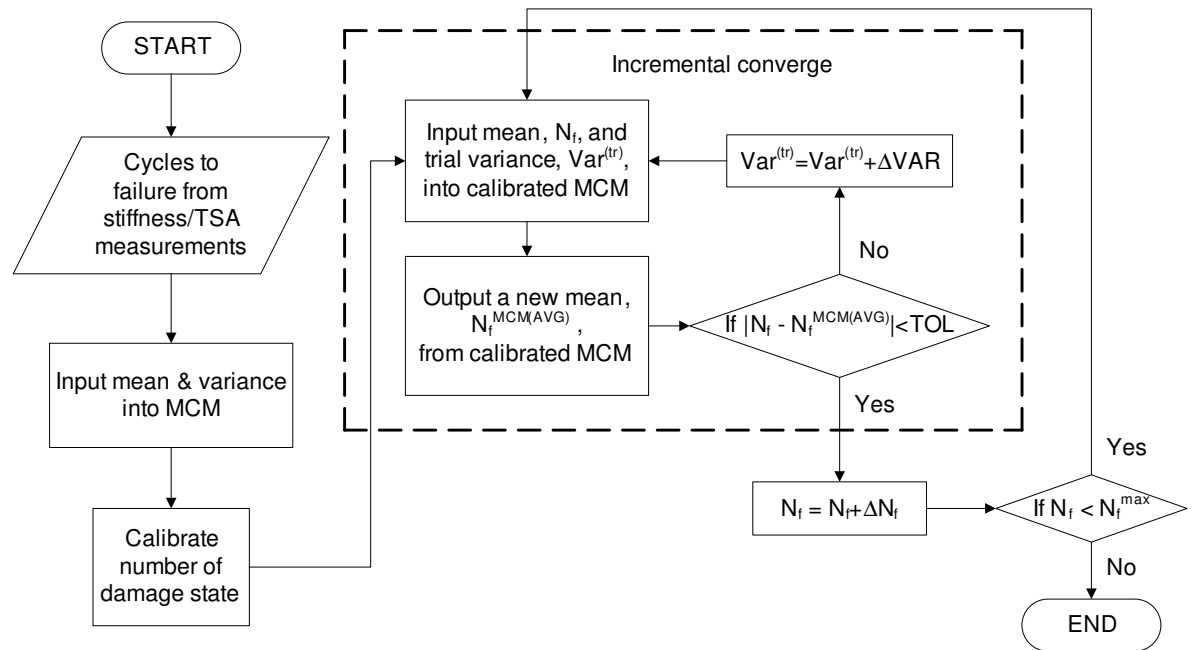


Figure 77: Schematic representation of the construction of stochastic SN curves.

5.6 TSA results and Stochastic S-N curves

This section presents preliminary results on different joint types. This experimental analysis provides qualitative behavior on the mode of damage progression and limited quantitative data on delamination and fracture. Further investigation is beyond the scope of this study. Figures 78, 79, 80, show TSA images of quasi-isotropic lay-ups for an IM7 laminate, single-lap joint, and single nested overlap joint. Figures 81, 82, 83, 84 show TSA images of quasi-isotropic lay-ups for S2-Glass/Epoxy laminate, single lap joint, and single nested overlap joint during fatigue testing respectively.

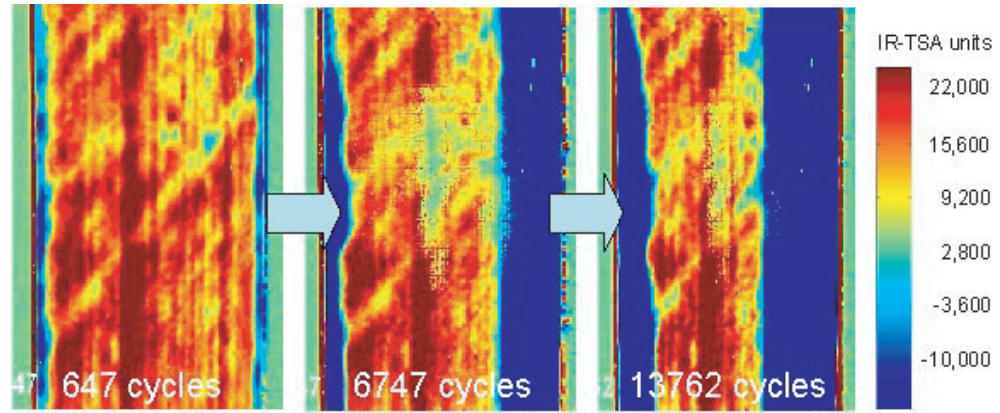


Figure 78: Thermoelastic Stress Analysis for Fatigue of an IM7 Laminate

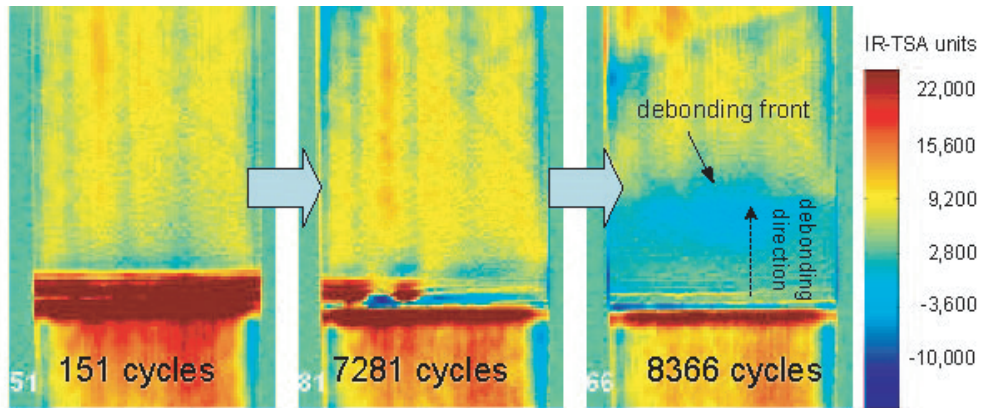


Figure 79: Thermoelastic Stress Analysis for Fatigue of an IM7 Single Lap Joint

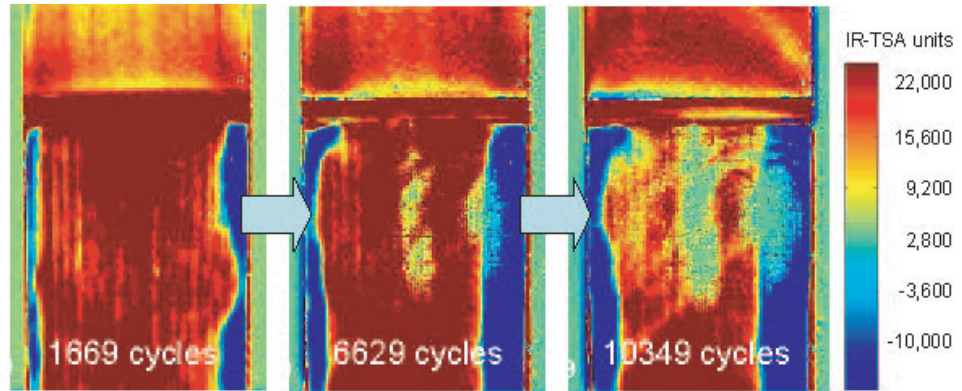


Figure 80: Thermoelastic Stress Analysis for Fatigue of an IM7 single nested overlap joint

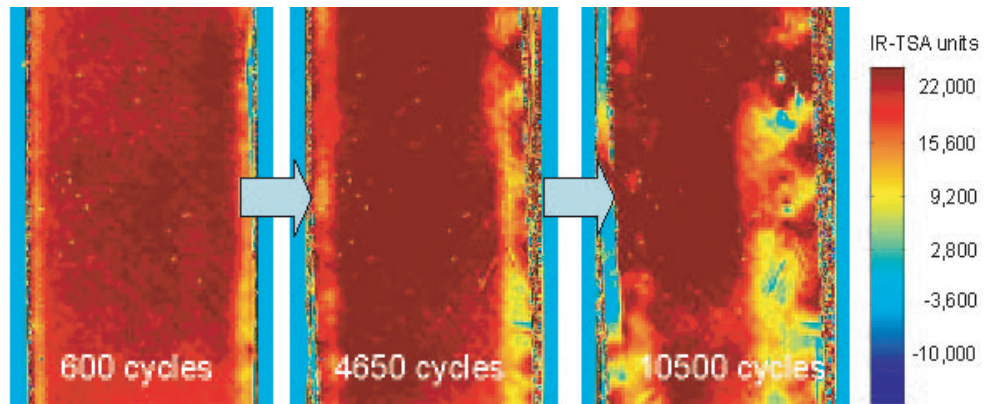


Figure 81: Thermoelastic Stress Analysis for Fatigue of a Unidirectional S2-Glass/Epoxy Laminate

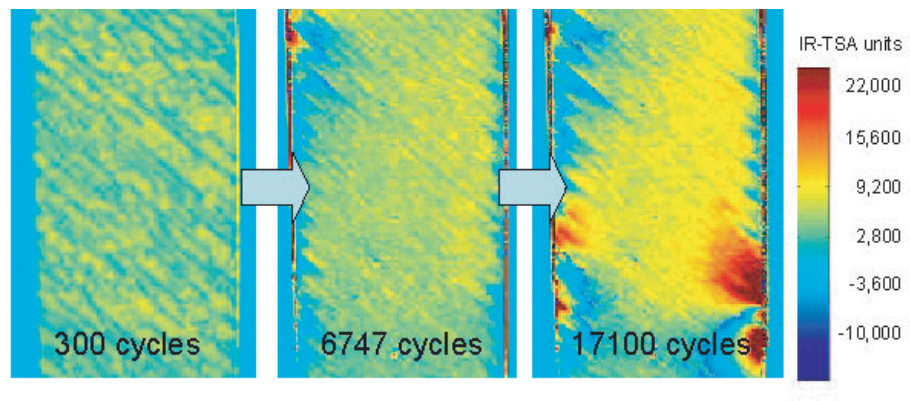


Figure 82: Thermoelastic Stress Analysis for Fatigue of a Quasi-Isotropic S2-Glass/Epoxy Laminate

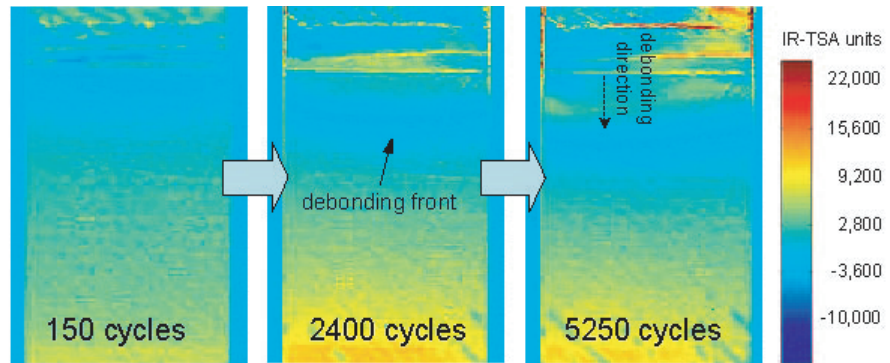


Figure 83: Thermoelastic Stress Analysis for Fatigue of a Quasi-Isotropic S2-Glass/Epoxy Single Nested Overlap Joint

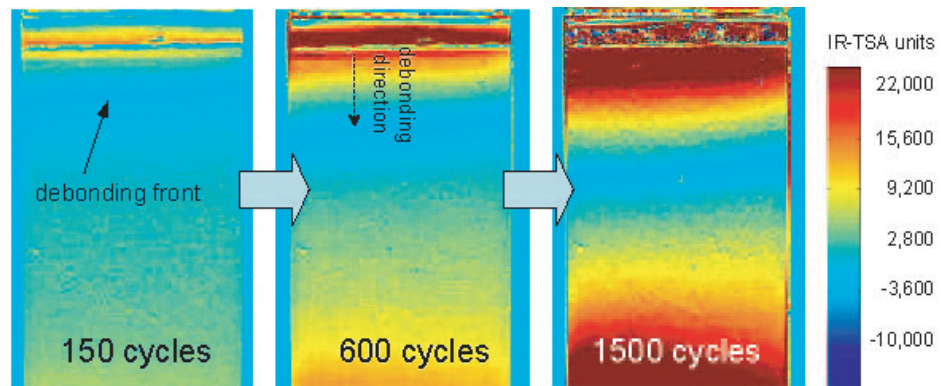


Figure 84: Thermoelastic Stress Analysis for Fatigue of a Quasi-Isotropic S2-Glass/Epoxy Single Nested Overlap Joint

CHAPTER VI

CONCLUSION

6.1 Quantitative Thermoelastic Stress Analysis

A experimental thermoelastic stress/strain analysis (TSA) technique was used to investigate multi-axial behavior variety of FRP composites including Carbon/epoxy, S2-glass/epoxy, and thick-section E-glass/polyester laminates. The new method relates the Thermoelastic signal to the sum of the normal surface strains in FRP composites, and it provides a full-field measurement of the strain invariant that can be used to verify computational models. If an additional isotropic surface coat is not applied to the surface of FRP laminates, two calibration constants may be needed to describe the system under a multi-axial state of stress. Further testing is needed to provide insight into the effects of the thickness of the isotropic coating and alternative surface coatings in order to guarantee the required adiabatic conditions. In addition, experimental methods using two calibration constants to eliminate the need for coating can be the subject of further research.

6.2 Analytical and Experimental Analyses for Jute Hybrid Bio-Composites

The linear and nonlinear mechanical behavior of Jute hybrid bio-composites was investigated, and new nonlinear micromechanical and macromechanical modeling approaches are developed for the analysis of the materials. Two of these nonlinear anisotropic homogeneous models assume that the material is under a state of plane stress. The third is a nonlinear 3D micromechanical model using a cohesive micromechanical model, a special case (Nine-Cell) of the more general High Fidelity Generalized Method of Cells (HFGMC) proposed by Aboudi [101] and modified by

Haj-Ali and Aboudi [58]. The three models proposed in the analytical study were able to capture the nonlinearity inherent in the material. The models from are calibrated from uniaxial experiments and validated under a multi-axial state of stress with Thermoelastic Stress Analysis (TSA) and Digital Image Correlation (DIC) using full-field stress-strain analysis of plates with a hole. The Nine-Cell model required linear orthotropic values taken from the literature in the axial and transverse directions to describe the jute yarn in addition to experimental stress vs. strain data in shear to calibrate the initial shear modulus in all of the constituents and nonlinear parameters for the matrix. This calibration allowed the Nine-Cell model to capture the nonlinearity in all directions. The Nine-Cell model was validated under uni-axial and multi-axial states of stress via full-field stress/strain analysis via digital image correlation (DIC) and Thermoelastic Stress Analysis (TSA) for the hybrid bio-composite system. The Nine-Cell model can be implemented for different fiber/matrix constituents with confidence of predictability with limited set of experimental tests. The ADT and APT models were able to capture more nonlinearity than the Nine-Cell model, but the macromechanical models required uni-axial calibrations in the axial, transverse, and shear modes to capture the nonlinear parameters. While these hybrid composites have relatively low modulus, their material consistency lends them to be used in many structural applications. Hybrid bio-composites are environmentally friendly and can provide a sustainable alternative to existing engineering materials in several applications.

6.3 Damage Initiation of FRP Lap Joints

Critical Stress and VCCT fracture criterion were developed with finite element models to predict damage initiation in graphite epoxy single lap joints. Two different quasi-isotropic lay-ups are compared for the purpose of investigating damage initiation in the lap joints. The models predict different responses for different lay-ups. The effect

of suppressing free-edge delamination on joint strength through re-ordering of the stacking sequence for eight-ply symmetric quasi-isotropic laminate was investigated under both monotonic and cyclic loading. A 15% improvement in UTS was observed for the free-edge delamination suppressed $[45/90/-45/0]_s$ laminates as compared to the original $[0/\pm 45/90]_s$ laminates. Experiments show that a lay-up with a higher static strength does not also correspond to a higher fatigue limit. The models show a greater correlation to the fatigue limit because damage initiation is predicted at a higher stress level for the $[0/\pm 45/90]_s$ lay-up compared to the $[45/90/-45/0]_s$.

To further investigate damage initiation in single lap joints, two new experimental techniques are developed to investigate the static damage initiation using TSA in FRP lap joints. The experimental results using testing Method-B show that TSA results and acoustic emission are closely related. An accumulation of acoustic responses is followed by TSA responses which show changes in the stress concentration at the bondline. This observation correlates well the finite element results showing that the majority of the shear stress in single lap shear joints is confined at or near the bondline while the interior bond of the joint is relatively unloaded. The infrared response at the bondline measured utilizing TSA in both Methods A and B show that failure initiation can be defined as the formation of discontinuities in the external bondline of the single lap joint. The combination of acoustic emission and TSA provides a wealth of information used for damage detection. Acoustic emission alone provides information on micro-cracking and the accumulation of those cracks to saturation impending ultimate failure, but infrared thermography provides a refinement on detecting the damage severity or a visual inspection of the location of damage. Specimens tested with Method-B are to be tested destructively focusing on the areas of discontinuities from infrared thermography. The latter confirm the IR-TSA damage observation.

This study presented an effective new IR-TSA method for detecting damage initiation and progression in single-lap composite joints. The proposed full-field method

was correlated with AE and mechanical load-deformation measurements. Select results were presented for long and short bond area joints as well as fabric versus quasi-isotropic uni-tape laminates. These results show a promising potential to extend the proposed new testing technique to other joint types and composite structural components for static and fatigue performance evaluation.

6.4 Stochastic Fatigue of FRP Lap Joints

A new in-situ fatigue degradation monitoring for S2-glass composite laminated lap joints using TSA techniques is utilized to predict failure. The proposed remote sensing method continuously captures the damage data during the test spatially, and this is seen as a major improvement on traditional contact methods (mechanical stiffness/strength measures, radiography, photoelasticity, and acoustic emission for investigating the fatigue life of FRPs) where the test must be stopped or where the severity of a damage event cannot be fully captured. The TSA images are post processed to provide two damage metrics, TSA area and length measures between debonding fronts within the single lap joint. The TSA area represents the remaining undamaged bonded region providing strength in shear, and the debonding front difference represents the remaining bonded length in the loading direction. The two damage metrics show similar trends in the overall fatigue process. In addition, the continuous monitoring makes the progression of S-N curves possible. Traditionally S-N curves are defined by final separation. However, the progression of the S-N curves provides engineers a more convenient approach to define different failure states to predict maintenance scheduling for laminated joints. Where previous fatigue studies on MCM were used to predict failure at one stress level using traditional contact based measurements, the proposed MCM requires calibrations from limited number of experiments and can effectively provide the entire stochastic S-N curve for the tested material systems. The new stochastic S-N curve method using Markov chain theory is

validated using two different stress levels for laminated lap joints using non-traditional test methods. A major goal of this study is to predict the complete stochastic S-N curve at a given damage state instead of damage evolution under one stress level. Therefore, the constant conditional probabilities in the PTM are calibrated from the experimental data directly show sufficient capabilities to construct the entire stochastic S-N curve. Massive fatigue testing efforts can be saved, and satisfactory results can be obtained by the proposed MCM. Future work may include novel joint types (such as: the reverse bent, wavy lap, or nested joint types) where fatigue performance is enhanced but damage progression and resistance becomes more complicated. The stochastic analysis offered in this study can also be used with failure criteria and provide reliability for new material/structural systems at various applied load levels.

6.5 Future Work

6.5.1 Fatigue of Lap Joints

Work with Thermoelastic Stress Analysis on joints will continue with an evaluation of different lay-up sequences and different joint types with new stochastic, computational and analytical fracture models for delamination in FRP Joints. Limited experimental analysis of different joint types is shown in Section 5.6. TSA has proven an excellent tool for in-situ evaluations of fatigue behavior in joints, and differences in behavior of FRP laminates, single lap joints, single nested overlap joints have been analyzed with this technique. Damage is accumulated in nested single overlap joints in the adherends at the joint ends, and failure occurs when the overlap fractures fully followed by debonding in the joint as seen in the single lap joint.

6.5.2 Fatigue of 3D Woven Fiber Reinforced Polymeric Material Systems

Fracture in FRP materials is complicated due to the various competing damage mechanisms, such as matrix cracking, fiber bridging, fiber rupture, fiber pullout, microbuckling, and delamination. More specifically, fracture and damage behavior in FRP materials is complicated as a result of their inherent heterogeneous and anisotropic nature which leads to fracture branching (a lack of self similar crack growth) and crack growth under unstable mixed modes. Fatigue damage further complicates the design with FRPs for the purpose of service life prediction because of competing failure mechanisms. A well-known method for characterizing the fatigue behavior in terms of applied stress-life (S-N) curve is widely adopted for metallic materials as well as FRP materials. Crack formation and growth is particularly important for conventional laminates, because cracks can run to and coalesce in the resin rich layers between plies, leading to failure by delamination. However, this failure mode is not present in 3D woven composites, because unreinforced resin layers do not exist in them. In addition, there is evidence to suggest that the 3D woven fibers act as crack stoppers which limit the extent of damage in a cracked composite. Since, 3D woven composites are insensitive to crack growth could lead to a redefinition of what really constitutes failure in them. Unfortunately, failure criteria intended to protect against delamination failure are often applied to 3D woven composites in aerospace structures in spite of the fact that delamination is not a failure mode for them. In reality, it is likely that these composites can be operated at higher strains or for longer design lives without fear of failure, which could lead to weight savings and/or performance improvements. It has been theorized that it may be more appropriate to design this type of composite to an S-N curve, similar to metal fatigue, than to a static strength. This would constitute a radical change in the way composite structures are designed, and it is anticipated that there would be significant resistance to the approach without substantial experimental verification. It is therefore profitable

to develop an innovative computational modeling program using a combination of probabilistic and deterministic models to account for the average behavior and variability in test results for 3D woven composites. It is necessary to capture spatial variability in the microstructure with micromechanical models like HFGMC to provide the theoretical motivation necessary on damage mechanisms in 3D composites (specifically, matrix cracking and fiber bridging) to implement changes in design. It is also necessary to validate these models with stiffness measurements and innovative experimental mechanics techniques such as TSA during in-situ fatigue for continuous full-field expressions of damage in combination with photomicroscopy for enhanced views of the microstructure for more full verification of the predicted results. The overall goal of this specific computational and experimental research program expands the use of composite technology in industry by furthering the use of 3D composites by theoretically and experimentally verifying the enhanced structural reliability provided by redundant load paths exploited by the material that eliminate delamination as damage mechanism and provide new failure criteria based on the actual damage mechanisms exposed by the fatigue of 3D woven composites.

REFERENCES

- [1] *DeltaTherm*. Stress Photonics Inc., Madison, WI, 2001.
- [2] *ABAQUS Theory Manual*. Dassault Systmes Simulia Corp., Providence, RI, USA, 2007.
- [3] ABOUDI, J. Micromechanical analysis of composites by the method of cells. *Appl. Mech. Rev.* *42*, 7 (1989), 193–221.
- [4] ABOUDI, J. *Mechanics of Composite Materials - A Unified Micromechanical Approach*. Elsevier, Amsterdam, New York, 1991.
- [5] ABOUDI, J. Micromechanical analysis of fully coupled electro-magneto-thermo-elastic multi-phase composites. *Smart Mater. Struct.* *10* (2001), 867–877.
- [6] ABOUDI, J. The generalized method of cells and high-fidelity generalized method of cells micromechanical models - a review. *Mech. Adv. Materl. Struct* *11* (2004), 329–366.
- [7] ABU-FARSAKH, G. New material models for nonlinear stress-strain behaviour of composite materials. *Composites* *20* (1989), 349.
- [8] AHMED, K. S., AND VIJAYARANGAN, S. Tensile, flexural and interlaminar shear properties of woven jute and jute-glass fabric reinforced polyester composites. *Journal of Materials Processing Technology* *207*, 1-3 (2008), 330 – 335.
- [9] AKIL, H. M., CHENG, L. W., MOHD ISHAK, Z. A., ABU BAKAR, A., AND ABD RAHMAN, M. A. Water absorption study on pultruded jute fibre reinforced unsaturated polyester composites. *Composites Science and Technology* *69*, 11-12 (2009), 1942–1948. doi: DOI: 10.1016/j.compscitech.2009.04.014.
- [10] AMIJIMA, S. ADACHI, T. Nonlinear stress-strain response of laminated composites. *J. Compos. Mater.* *13* (1979), 206–218.
- [11] ARNOLD, S., BEDNARCYK, B., AND ABOUDI, J. Analysis of internally cooled structures using a high order theory. *Comput. Struct.* *82* (2004), 659–688.
- [12] AVILA, A. F., AND DE O. BUENO, P. An experimental and numerical study on adhesive joints for composites. *Composite structures* *64* (2004), 513–537.
- [13] BAKIS, C., AND REIFSNIDER, K. The adiabatic thermoelastic effect in laminated fiber composites. *Journal of Composite Materials* *25* (1991), 809–830.

- [14] BAKIS, C. E., YIH, H. R., STINCHCOMB, W. W., AND REIFSNIDER, K. L. Damage initiation and growth in notched laminates under reversed cyclic loading. *Composite Material: Fatigue and Fracture 2* (1989), 66–83.
- [15] BANK, L. C. Shear properties of pultruded glass frp materials. *J. Mater Civil Eng. 2* (1990), 118–22.
- [16] BANK, L. C., AND YIN, J. Failure of web-angle junction in postbuckled pultruded I-beams. *Journal of Composites for Construction* (1999), 17784.
- [17] BARONE, S., AND PATTERSON, E. Polymer coatings as strain witness in thermoelasticity. *Journal of strain analysis 33*, 3 (1998), 223–232.
- [18] BEDNARCYK, B., ABOUDI, J., ARNOLD, S., AND SULLIVAN, R. Analysis of space shuttle external tank spray-on foam insulation with internal pore pressure. *J. Engrg. Mat. Tech. 130* (2008).
- [19] BEDNARCYK, B., ARNOLD, S., ABOUDI, J., AND PINDER, M.-J. Local field effects in titanium matrix composites subject to fiber-matrix debonding. *Int. J. Plasticity 20* (2004), 1707–1737.
- [20] BEDNARCYK, B., AND YARRINGTON, P. Elasto-plastic analysis of tee joints using hot-smac. Tech. rep., 2004.
- [21] BISANDA, E. T. N. The manufacture of roofing panels from sisal fibre reinforced composites. *Journal of Materials Processing Technology 38*, 1-2 (1993), 369–379. doi: DOI: 10.1016/0924-0136(93)90209-O.
- [22] BISANDA, E. T. N., AND ANSELL, M. P. The effect of silane treatment on the mechanical and physical properties of sisal-epoxy composites. *Composites Science and Technology 41*, 2 (1991), 165–178. doi: DOI: 10.1016/0266-3538(91)90026-L.
- [23] BISANDA, E. T. N., AND ANSELL, M. P. *J Mater Sci 27* (1992), 16901700.
- [24] BLEDZKI, A., FARUK, O., AND SPERBER, V. Cars from bio-fibres. *Macromolecular Materials and Engineering 291* (2006), 449–457.
- [25] BODNER, S. *Unified Plasticity for Engineering Applications*. Kluwer, New York, 2002.
- [26] BOGDANOFF, J. L. A new cumulative damage model, part 1. *Journal of Applied Mechanics 45* (1978), 246–250.
- [27] BOGDANOFF, J. L. A new cumulative damage model, part 3. *Journal of Applied Mechanics 45* (1978), 733–739.
- [28] BOGDANOFF, J. L., AND KOZIN, F. *Probabilistic models of cumulative damage*. John Wiley & Sons, 1985.

- [29] BOGDANOFF, J. L., AND KRIEGER, W. A new cumulative damage model, part 2. *Journal of Applied Mechanics* 45 (1978), 251–257.
- [30] BORSELLINO, C., CALABRESE, L., BELLA, G. D., AND VALENZA, A. Comparisons of processing and strength properties of two adhesive systems for composite joints. *International Journal of Adhesion and Adhesives* 27 (2007), 446–457.
- [31] BREMOND, P., AND POTET, P. Lock-in thermography: a tool to analyze and locate thermomechanical mechanisms in materials and structures. *Proceedings of SPIE, the International Society for Optical Engineering* 4360 (2001), 560–566.
- [32] CAMPILHO, R. D. S. G., DE MOURA, M. F. S. F., AND DOMINGUES, J. J. M. S. Modelling single and double-lap repairs on composite materials. *Composites Science and Technology* 65, 13 (2005), 1948 – 1958.
- [33] CAVALIERE, P., ROSSI, G. L., DI SANTE, R., AND MORETTI, M. Thermoelasticity for the evaluation of fatigue behavior of 7005/al2o3/10p metal matrix composite sheets joined by fsw. *International Journal of Fatigue* 30, 1 (2008), 198–206. doi: DOI: 10.1016/j.ijfatigue.2007.01.021.
- [34] CAVALIERE, P., SANTIS, A. D., PANELLA, F., AND SQUILLACE, A. Thermoelasticity and ccd analysis of crack propagation in aa6082 friction stir welded joints. *International Journal of Fatigue* 31, 2 (2009), 385–392. doi: DOI: 10.1016/j.ijfatigue.2008.07.016.
- [35] CHAND, N., AND ROHATGI, P. Adhesion of previous termsisalnext term fibre polyester system. *Polym. Commun.* 27 (1986), 157–160.
- [36] CUNNINGHAM, P., DULIEUBARTON, J. M., DUTTON, A., AND SHENOI, R. Thermoelastic characterisation of damage around a circular hole in a grp component. *Key Engineering Materials* 204-205 (2001), 453–463.
- [37] DA SILVA, L. F. M., AND ADAMS, R. D. Techniques to reduce the peel stresses in adhesive joints with composites. *International Journal of Adhesion and Adhesives* 27, 3 (2007), 227 – 235.
- [38] DALLY, J., AND SANFORD, R. Strain-gage method for measuring the opening-mode stress-intensity factor, k_i . *Experimental Mechanics* 27, 4 (1987), 381–388.
- [39] DIAZ, F. A., PATTERSON, E. A., TOMLINSON, R. A., AND YATES, J. R. Measuring stress intensity factors during fatigue crack growth using thermoelasticity. *Fatigue & Fracture of Engineering Materials and Structures* 27 (2004), 571–583.
- [40] DIAZ, F. A., YATES, J. R., AND PATTERSON, E. A. Some improvements in the analysis of fatigue cracks using thermoelasticity. *International Journal of Fatigue* 26 (2004), 365–376.

- [41] DICKSON, J. N., HSU, T., AND MCKINNEY, J. Development of an understanding of the fatigue phenomena of bonded and bolted joints in advanced filamentary composite materials. Tech. rep., Lockheed-Georgia Co., 1972.
- [42] DULIEU-BARTON, J., EMERY, T., QUINN, S., AND CUNNINGHAM, P. A temperature correction methodology for quantitative thermoelastic stress analysis and damage assessment. *Measurement Science and Technology* 16 (2006), 1627–1637.
- [43] DULIEU-SMITH, J. M., QUINN, S., SHENOI, R. A., READ, P. J. C. L., AND MOY, S. S. J. Thermoelastic stress analysis of a grp tee joint. *Applied Composite Materials* 4, 5 (1997), 283–303.
- [44] DUNN, S. On the effects of through-thickness thermal conduction on stress measurement by thermoelastic techniques. *Experimental Mechanics* 33 (1993), 32–36.
- [45] DVORAK, G., AND RAO, M. Axisymmetric plasticity theory of fibrous composites. *Int. J. Eng. Sci.* 14 (1976), 361–373.
- [46] DWEIB, M. A., HU, B., O'DONNELL, A., SHENTON, H. W., AND WOOL, R. P. All natural composite sandwich beams for structural applications. *Composite Structures* 63, 2 (2004), 147–157. doi: DOI: 10.1016/S0263-8223(03)00143-0.
- [47] EDEEROZEY, A. M. M., AKIL, H. M., AZHAR, A. B., AND ARIFFIN, M. I. Z. Chemical modification of kenaf fibers. *Materials Letters* 61, 10 (2007), 2023–2025. doi: DOI: 10.1016/j.matlet.2006.08.006.
- [48] EL-HAJJAR, R., AND HAJ-ALI, R. A quantitative thermoelastic stress analysis method for pultruded composites. *Composites Science and Technology* 63, 7 (2003), 967 – 978.
- [49] EL-HAJJAR, R., AND HAJ-ALI, R. In-plane shear testing of thick-section pultruded frp composites using a modified arcan fixture. *Composites Part B: Engineering* 35, 5 (2004), 421 – 428.
- [50] EMERY, T., DULIEU-BARTON, J., EARL, J., AND CUNNINGHAM, P. A generalised approach to the calibration of orthotropic materials for thermoelastic stress analysis. *Compos Sci Techno* 68 (2008), 743–752.
- [51] FESSEL, G., BROUGHTON, J. G., FELLOWS, N. A., DURODOLA, J. F., AND HUTCHINSON, A. R. Evaluation of different lap shear joint geometries for automotive applications. *International Journal of Adhesion and Adhesives* 27 (2007), 574–583.
- [52] GOLAND, M., AND REISSNER, E. The stresses in cemented joints. *Journal of Applied Mechanics* 11, A17-A27 (1944).

- [53] GRIFFIN, O., KAMAT, M., AND HERAKOVICH, C. Threedimensional finite element analysis of laminated composites. *J. Composite Materials* 5 (1981), 543–560.
- [54] HAHN, T. Nonlinear behaviour of laminated composites. *J. Compos. Mater* 7 (1973), 257271.
- [55] HAHN, T., AND TSAI, S. Nonlinear elastic behavior of unidirectional composite laminae. *J. Compos. Mater* 7 (1973), 102–118.
- [56] HAJ-ALI, R. Cohesive micromechanics: A new approach for progressive damage modeling in laminated composites. *International Journal of Damage Mechanics* 18, 8 (2008), 691–719.
- [57] HAJ-ALI, R. Nested nonlinear multi-scale frameworks for the analysis of thick-section composite materials and structures, in: Multiscale modeling and simulation of composite materials and structures, 2008.
- [58] HAJ-ALI, R., AND ABOUDI, J. Nonlinear micromechanical formulation of the high fidelity generalized method of cells. *International Journal of Solids and Structures* 46, 13 (2009), 2577 – 2592.
- [59] HAJ-ALI, R., AND KILIC, H. Nonlinear behavior of pultruded frp composites. *Composites Part B: Engineering* 33, 3 (2002), 173 – 191.
- [60] HAJ-ALI, R., AND KILIC, H. Nonlinear constitutive models for pultruded frp composites. *Mechanics of Materials* 35, 8 (2003), 791 – 801.
- [61] HAJ-ALI, R., KILIC, H., AND MULIANA, A. Nested nonlinear micromechanical and structural models for the analysis of thick-section composite materials and structures. *Composites Science and Technology* 67, 10 (2007), 1993 – 2004.
- [62] HAJ-ALI, R., WEI, B.-S., JOHNSON, S., AND EL-HAJJAR, R. Thermoelastic and infrared-thermography methods for surface strains in cracked orthotropic composite materials. *Engineering Fracture Mechanics* 75, 1 (2008), 58 – 75.
- [63] HAJ-ALI, R. M., AND EL-HAJJAR, R. F. A thermoelastic method for strain measurement in coated orthotropic materials. *Experimental Mechanics* (2004).
- [64] HANSBO, A., AND HANSBO, P. A finite element method for the simulation of strong and weak discontinuities in solid mechanics. *computer Method in Applied Mechanis and Engineering* 193 (2004), 3524–3540.
- [65] HART-SMITH, L. Adhesive bonded single-lap joints. Tech. rep., NASA, 1973.
- [66] HART-SMITH, L. Analysis and design of advanced composite bonded joints. Tech. rep., National Aeronautics and Space Administration, 1974.

- [67] HASHIN, Z., BAGCHI, D., AND ROSEN, B. Nonlinear behavior of fiber composite laminates. *NASACR-2313* (1974).
- [68] HEMELRIJCK, D. V., SCHILLEMANS, L., ROEY, F. D., DAERDEN, I., BOULPAEP, F., WILDE, P. D., AND CARDON, A. Thermoelastic stress analysis of fibre reinforced composite systems. *3rd International Conference on Computer Aided Design in Composite Material Technology - CADCOMP 92* (1992), 626–633.
- [69] HERAKOVICH, C. T., AND MIRZADEH, F. Properties of pultruded graphite/epoxy. *J Reinforced Plastics Compos* 10 (1991), 2–28.
- [70] HONG, C., HWANG, I., KIM, N., PARK, D., HWANG, B., AND NAH. Mechanical properties of silanized jute-polypropylene composites. *Journal of Industrial and Engineering Chemistry* 14 (2008), 71–76.
- [71] HWANG, S. K. C. S. W. Application of a hybrid finite element method to determine stress intensity factors in unidirectional composites. *International Journal of Fracture* 31 (1986), 37–51.
- [72] IRWIN, G. Analysis of stress and strain near the end of a crack traversing a plate. *Journal of Applied Mechanics* 24 (1957), 361–364.
- [73] JOHNSON, S. *Infrafred thermography and thermoelastic stress analysis of composite materials and structural systems*. PhD thesis, 2006.
- [74] JOHNSON, S., KIM, H., WEI, B. S., AND HAJ-ALI, R. Infrared thermography for damage and fatigue of thick-section frp composites.
- [75] JONES, R., HELLER, M., LOMBARDO, D., DUNN, S., PAUL, J., AND SAUNDERS, D. Thermoelastic assessment of damage growth in composites. *Composite Structures* 12, 4 (1989), 291–314. doi: DOI: 10.1016/0263-8223(89)90077-9.
- [76] JONES, R., AND MORGAN, H. Analysis of nonlinear stress-strain behavior of fiber reinforced materials. *AIAA* 15 (1977), 1669–1676.
- [77] JONES, R., AND NELSON JR., D. A new material model for the nonlinear biaxial behavior of atj-s graphite. *J. Compos. Mater.* 9 (1974), 10–27.
- [78] JU, S., AND ROWLANDS, R. Thermoelastic determination of k_i and k_{ii} in an orthotropic graphite-epoxy composite. *Journal of Composite Materials* 37 (2003), 2011–2025.
- [79] KAGEYAMA, K., UEKI, K., AND KIKUCHI, M. Fatigue damage analysis of notched carbon/epoxy laminates by thermoelastic emission and three dimensional finite element methods. *Proc. 7th Conf. Comp. Mat. ICCM 7* (1989).
- [80] KHAN, A., AND HUANG, S. *Continuum Theory of Plasticity*. Wiley, New York, 1995.

- [81] KILIC, H., AND HAJ-ALI, R. Elastic-degrading analysis of pultruded composite structures. *Composite Structures* 60, 1 (2003), 43 – 55.
- [82] KILIC, H., AND HAJ-ALI, R. Progressive damage and nonlinear analysis of pultruded composite structures. *Composites Part B: Engineering* 34, 3 (2003), 235 – 250.
- [83] KOZIN, F., AND BOGDANOFF, J. L. A critical analysis of some probabilistic models of fatigue crack growth. *Engineering Fracture Mechanics* 14 (1980), 59–89.
- [84] KRISHNAMURTHY, W. S. T. Probabilistic and possibilistic analyses of the strength of a bonded joint. Tech. rep., American Institute of Aeronautics and Astronautics, 2001.
- [85] KRUEGER, R. The virtual crack closure technique: history, approach and applications. Tech. rep., 2002.
- [86] KUPPUSWAMY, T., NADA, A., AND REDDY, J. Materially nonlinear analysis of laminated composite plates. *Compos. Struct.* 2 (1984), 315–328.
- [87] KYRIAKOPOULOS, M. K., WILDE, W. P. D., HEMELRIJCK, D. V., AND SCHILLEMANS, L. A finite element approach for thermal-structural response in fibre reinforced composite systems. *3rd International Conference on Computer Aided Design in Composite Material Technology - CADCOMP 92* (1992), 599–614.
- [88] LEKHNITSKII, S. *Theory of Elasticity of an Anisotropic Body*. Holden-Day, San Francisco, 1963.
- [89] LIU, Y., AND MAHADEVAN, S. Stochastic fatigue damage modeling under variable amplitude loading. *International Journal of Fatigue* 29 (2007), 1149–1161.
- [90] LOEVE, M. *Probability theory*. Springer, New York, 1977.
- [91] LOHR, D. T., ENKE, N. F., AND SANDOR, B. I. Analysis of fatigue damage evolution by differential infrared thermography. *Proceedings of the 1987 SEM Fall Conference* (1987).
- [92] MACKENZIE, A. K. Effects of surface coatings on infrared measurements of thermoelastic responses. *SPIE* 1084 (1989), 59–71.
- [93] MACKIN, T. J., AND ROBERTS, M. C. Evaluation of damage evolution in ceramic-matrix composites using thermoelastic stress analysis. *J. Am. Ceram. Soc.* 83 (2000), 337–343.
- [94] MAHADEVAN, Y. L. S. Probabilistic fatigue life prediction of multidirectional composite laminates. *Composite Structures* 69 (2005), 11–19.

- [95] MANDELL, J., AND SAMBORSKY, D. Contractor report sand97-3002. Tech. rep., 1997.
- [96] MATHISON, S., PINDER, M., AND HERAKOVICH, C. Nonlinear response of resin matrix laminates using endochronic theory. *J. Eng. Mat. Tech.* 113 (1991), 449–455.
- [97] MATHUR, V. K. Composite materials from local resources. *Construction and Building Materials* 20 (2006), 470–477.
- [98] MUSKHELISHVILI, N. *Some Basic Problems of the Mathematical Theory of Elasticity*. P. Noordhoff, Ltd, Groningen-Holland, 1954.
- [99] NAHAS, M. Analysis of non-linear stress-strain response of laminated fibre-reinforced composites. *Fibre Sci. Tech.* 20 (1984), 297–313.
- [100] PAGANO, N. J., AND . Exact moduli of anisotropic laminates. *Mechanics of composite materials* (1974), 23–44.
- [101] PALEY, M., AND ABOUDI, J. Micromechanical analysis of composites by the generalized cells model. *Mechanics of Materials* 14, 2 (1992), 127 – 139.
- [102] PETIT, P. H. A simplified method of determining the in-plane shear stress-strain response of unidirectional composites. astm stp 460. philadelphia, pa; 1969. *ASTM STP* (1969).
- [103] PINDER, M., AND HERAKOVICH, C. An endochronic model for the response of unidirectional composites under off-axis tensile load. In *IUTAM Symposium on Mechanics of Composite Materials* (New York, 1983), Mechanics of Composite Materials: Recent Advances, Pergamon Press, pp. 367–381.
- [104] POTTER, R. Stress analysis in laminated fibre composites by thermoelastic emission. In *SPIE* (1987), vol. 731, pp. 110–120.
- [105] POTTER, R., AND GREAVES, L. The application of thermoelastic stress analysis technique to fibre composites. *SPIE* 817 (1988), 134–146.
- [106] RICHARD, R., AND ABBOTT, B. Versatile elastic-plastic stress-strain formula. *ASCE J. Eng. Mech. Div., Technical Note* 101 (1975), 511–515.
- [107] ROE, P. J., AND ANSELL, M. P. *J Mater Sci* 20 (1985), 40154020.
- [108] ROH, Y. S., AND XI, Y. A general formulation for transition probabilistic of markov model and the application of fracture of composite materials. *Probabilistic Engineering Mechanics* 15 (2000), 241–250.
- [109] ROWATT, J. D. *A probabilistic model for fatigue damage accumulation in composite laminates*. M.s., 1993.

- [110] ROWATT, J. D., AND SPANOS, P. D. Markov chain models for life prediction of composite laminates. *Structural Safety* 20 (1998), 117–135.
- [111] RYBICKI, E., AND KANNINEN, M. F. A finite element calculation of stress intensity factors by a modified crack closure integral. *Engineering Fracture Mechanics* 9 (1977), 931–938.
- [112] SANDHU, R. Non-linear behaviour of unidirectional and angle-ply laminates. *J. Aircraft* 13 (1976), 104–111.
- [113] SHAN, A. N., AND LAKKARD, S. C. Effect of interface modification on the mechanical properties of polystyrene-sisal fiber composites. *Fibre Sci Technol* 15 (1981), 4146.
- [114] SHUKLA, A., AGARWAL, B., AND BHUSHAN, H. Determination of stress intensity factor in orthotropic composite materials using strain gages. *Engineering Fracture Mechanics* 32 (1989), 469–477.
- [115] SIH, G., PARIS, P., AND IRWIN, G. On cracks in rectilinearly anisotropic bodies. *International Journal of Fracture Mechanics* 1 (1965), 189–203.
- [116] SIMO, J., AND T.J.R., H. *Computational Inelasticity*. Springer, New York, 1998.
- [117] SONG, J., AREIAS, P., AND BELYTSCHKO, T. A method for dynamic crack and shear band propagation with phantom nodes. *International Journal for Numerical Methods in Engineering* 67 (2006), 868–893.
- [118] SRIDHAR, M. K., AND BASAVARAJAPPA, G. *Indian J Text Res* 79 (1982), 8792.
- [119] SUN, C., AND CHEN, J. A simple flow rule for characterizing nonlinear behavior of fiber composites. *J. Compos. Mater.* 23 (1989.), 1009–1020.
- [120] SUN, R. W. X. *Bio-Based Polymers and Composites*. Elsevier Science and Technology Books, 2005.
- [121] SUO, Z., BAO, G., FAN, B., AND WANG, T. C. Orthotropy rescaling and implications for fracture in composites. *International Journal of Solids and Structures* 28, 2 (1991), 235–248. doi: DOI: 10.1016/0020-7683(91)90208-W.
- [122] TAMUZS, V., DZELZITIS, K., AND REIFSNIDER, K. Fatigue of woven composite laminates in off-axis loading i. the mastercurves. *Applied Composite Materials* 11 (2004), 259–279.
- [123] TAMUZS, V., DZELZITIS, K., AND REIFSNIDER, K. Fatigue of woven composite laminates in off-axis loading ii. prediction of the cycle durability. *Applied Composite Materials* 11 (2004), 281–293.

- [124] TANIMOTO, T. Correlation of statistical fatigue properties in a wide stress range for frp laminates with failure mechanisms. *International Journal of Fatigue* 28 (2006), 1493–1500.
- [125] THOMSON, W. On the thermoelastic, thermomagnetic and pyro-electric properties of matter. *Phil. Mag.* 5 (1878), 4–27.
- [126] TOMBLIN, J., AND BARBERO, E. J. Compression strength of pultruded fiber reinforced composites. vol. 1, p. 747. Proceedings of the 10th conference on engineering mechanics.
- [127] TOMLINSON, R. A., AND MARSAVINA, L. Thermoelastic investigations for fatigue life assessment. *Experimental Mechanics* 44, 5 (2004), 487–494.
- [128] VAN DE VELDE, K., AND KIEKENS, P. Thermoplastic pultrusion of natural fibre reinforced composites. *Composite Structures* 54, 2-3, 355–360. doi: DOI: 10.1016/S0263-8223(01)00110-6.
- [129] VARMA, I. K., ANANTHA KRISHNAN, S. R., AND KRISHNAMOORTHY, S. Composites of glass/modified jute fabric and unsaturated polyester resin. *Composites* 20, 4 (1989), 383–388. doi: DOI: 10.1016/0010-4361(89)90664-2.
- [130] WANG, Y., AND ZUREICK, A.-H. Characterization of the longitudinal tensile behavior of pultruded i-shape structural members using coupon specimens. *Composite Structures* 29, 4 (1994), 463 – 472.
- [131] WEI, B. S. *Thermoelastic Stress Analysis Techniques for Mixed Mode Fracture and Stochastic Fatigue of Composite Materials*. Phd, 2008.
- [132] WEI, B.-S., JOHNSON, S., AND HAJ-ALI, R. A stochastic fatigue damage method for composite materials based on markov chains and infrared thermography. *International Journal of Fatigue* 32, 2 (2009), 350–360.
- [133] WELCH, C., AND ZICKEL, M. *Thermal coating characterization using thermoelasticity*, vol. 12 of *Review of Progress in Quantitative Nondestructive Evaluation*. Plenum Press, New York, NY, 1993.
- [134] WESTERGAARD, H. Bearing pressures and cracks. *Journal of Applied Mechanics* 6 (1939), 49–53.
- [135] WONG, A., JONES, R., AND SPARROW, J. Thermoelastic constant or thermoelastic parameter? *J Phys Chem Solids* 48, 8 (1987), 749–53.
- [136] WU, W., AND NI, C. Probabilistic models of fatigue crack propagation and their experimental verification. *Probabilistic Engineering Mechanics* 19 (2004), 247–257.
- [137] XI, Y., AND BAZANT, Z. P. Random growth of crack with r-curve: Markov process model. *Engineering Fracture Mechanics* 57, 6 (1997), 593–608.

- [138] ZADORECKI, P., AND FLODIN, P. Surface modification of cellulose fibers. ii. the effect of cellulose fiber treatment on the performance of cellulose-polyester composites. *J. Appl. Polym. Sci.* (1985), 3971–3983.
- [139] ZENG, Q., AND SUN, C. T. Fatigue performance of a bonded wavy compstie lap joint. *Fatigue and Fracture of Engineering Materials and Structures 27* (2004), 413–422.
- [140] ZHANG, D., ENKE, N., AND SANDOR, B. Thermographic stress analysis of composite materials. *Experimental Mechanics 30*, 1 (1990), 68–73.
- [141] ZHANG, D., AND SANDOR, B. Thermographic analysis of stress concentrations in a composite. *Experimental Mechanics 29*, 2 (1989), 121–5.
- [142] ZHANG, D., AND SANDOR, B. A thermoelasticity theory for damage in anisotropic materials. *Fatigue and Fracture of Engineering Materials and Structures 13*, 5 (1990), 497–509.